

REPORT DOCUMENTATION PAGE					<i>Form Approved OMB No. 0704-0188</i>	
The public reporting burden for this collection of information is estimated to average 1 hour per response, including the time for reviewing instructions, searching existing data sources, gathering and maintaining the data needed, and completing and reviewing the collection of information. Send comments regarding this burden estimate or any other aspect of this collection of information, including suggestions for reducing the burden, to the Department of Defense, Executive Service Directorate (0704-0188). Respondents should be aware that notwithstanding any other provision of law, no person shall be subject to any penalty for failing to comply with a collection of information if it does not display a currently valid OMB control number.						
PLEASE DO NOT RETURN YOUR FORM TO THE ABOVE ORGANIZATION.						
1. REPORT DATE (DD-MM-YYYY) 01/27/2012		2. REPORT TYPE Final Technical Report			3. DATES COVERED (From - To) June 15, 2008 to December 31, 2011	
4. TITLE AND SUBTITLE Health Monitoring of Composite Structures Using Guided Waves				5a. CONTRACT NUMBER FA9550-08-1-0311		
				5b. GRANT NUMBER		
				5c. PROGRAM ELEMENT NUMBER		
				5d. PROJECT NUMBER		
6. AUTHOR(S) Dr. Joseph L. Rose				5e. TASK NUMBER		
				5f. WORK UNIT NUMBER		
7. PERFORMING ORGANIZATION NAME(S) AND ADDRESS(ES) The Pennsylvania State University 212 Earth-Engineering Sciences Building University Park, PA 16802				8. PERFORMING ORGANIZATION REPORT NUMBER		
9. SPONSORING/MONITORING AGENCY NAME(S) AND ADDRESS(ES) Air Force Office of Scientific Research Aerospace, Chemical, and Material Sciences 875 N. Randolph Street Suite 325, Room 3112 Arlington VA, 22203-1768				10. SPONSOR/MONITOR'S ACRONYM(S)		
				11. SPONSOR/MONITOR'S REPORT NUMBER(S) AFRL-OSR-VA-TR-2012-0264		
12. DISTRIBUTION/AVAILABILITY STATEMENT Approved for public release; distribution is unlimited						
13. SUPPLEMENTARY NOTES						
14. ABSTRACT Two guided wave SHM approaches were developed in this project. The first approach is based on a guided wave tomographic technique, in which the region surrounded by a sparse sensor array is monitored. The second one is a phased array approach, in which sensors are attached to a structure in a compact format to form an array. The region subjected to inspection and monitoring is the region outside the array. Both techniques have shown an excellent capability of determining damage size, location, and severity. The importance of guided wave mode and frequency control has been demonstrated for both the tomography and the phased array approach. Guided wave annular arrays have been successfully developed as a means of mode and frequency control. Phased annular array transducers with excellent flexibility on guided wave mode tuning have also been investigated. Guided wave tomography with improved robustness to environmental conditions was demonstrated via the application of specially designed annular arrays. Damage detection using phased array beamforming was also achieved. Unique beamformer transducers were developed and applied to both isotropic and anisotropic multilayer composite structures.						
15. SUBJECT TERMS Composite, Health Monitoring, Ultrasonic Guided Wave, Phased Array, Tomography						
16. SECURITY CLASSIFICATION OF:			17. LIMITATION OF ABSTRACT UU	18. NUMBER OF PAGES 100	19a. NAME OF RESPONSIBLE PERSON Joseph L. Rose	
a. REPORT U	b. ABSTRACT U	c. THIS PAGE U			19b. TELEPHONE NUMBER (Include area code) 8148638026	

Reset

Final Report

On

Project No. FA9550-08-1-0311

Health Monitoring of Composite Structures Using Guided Waves

Submitted to

AFOSR

Program Manager: Dr. David Stargel

By

Penn State University

Joseph L. Rose

On

January 20, 2012

Table of contents

Table of contents	2
Summary:	3
Composite plates	4
Wave mechanics studies	4
Guided wave excitation by SHM sensors	12
Source influence for straight-crested plane waves	12
Excitation of circular-crested guided waves by point sources	14
Guided wave excitation of PWAS in isotropic plates	16
Guided wave excitation in composite plates	24
Skew angle based composite inspection method	33
Guided wave tomography using annular array transducers	39
Annular array transducer design and fabrication	39
Proof-of-concept delamination detection experiment using annular arrays	48
An example application of annular array tomography	50
Phased Annular Array Transducer Design	53
Selective Radiation	55
Numerical Simulations.....	57
Piezocomposite based Phased annular array transducers.....	60
Experimental observations of a 1-3 piezocomposite phased annular transducer.....	63
Phased array beam steering in anisotropic composite plates	66
Introduction of guided wave beam steering in composite plates	66
Angular dependences of guided waves in composite plates	67
Guided wave Phased array Directivity profiles	69
Experiments and results	73
Defect detection in a composite plate using a phased array	77
Phased Beamformer Transducer Design	78
Finite element modeling of guided wave beam forming	79
Experiments on an isotropic plate.....	81
Guided wave mode control with Phased Annular Array transducers.....	87
Beamforming with a Phased Annular Beamformer Transducer	89
Phased Array System with Nonlinear Phase Delays	93
Theory.....	93
<i>Phased array on a rectangular grid</i>	94
<i>Proposed phased array configuration</i>	95
Finite element simulation.....	95
<i>Multichannel phase delay system</i>	96
Concluding remarks.....	97
Personnel supported	98
Publications	98
References	99

Summary:

Structural health monitoring (SHM) of fiber reinforced composite structures has become a very critical topic for aviation safety due to the fact that the use of composite materials in the aircraft industry has steadily increased in recent decades. Composite materials offer many mechanical advantages over metallic materials when being used in the aircraft industry. However, since the composite materials are generally anisotropic, and the defects generated in composite structures are usually not visible from material surfaces, the use of composite materials prompts challenges to the SHM community. The objective of this project is to answer the challenges by developing a reliable and cost effective ultrasonic guided wave based SHM techniques that take into account the material anisotropy of composite structures.

In the early performance period of the project, analytical and numerical tools for guided wave propagation in anisotropic composite plates were established. The tools were then used to aid the further developments of guided wave mechanics based SHM techniques.

Two guided wave SHM approaches were developed in this project. The first approach is based on a guided wave tomographic technique, in which the region surrounded by a sparse sensor array is monitored. The second one is a phased array approach, in which sensors are attached to a structure in a compact format to form an array. The region subjected to inspection and monitoring is the region outside the array. Both techniques have shown an excellent capability of determining damage size, location, and severity.

The importance of guided wave mode and frequency control has been demonstrated for both the tomography and the phased array approach. Guided wave annular arrays have been successfully developed as a means of mode and frequency control. Phased annular array transducers with excellent flexibility on guided wave mode tuning have also been investigated.

Guided wave tomography with improved robustness to environmental conditions was demonstrated via the application of specially designed annular arrays. Damage detection using phased array beamforming was also achieved. Unique beamformer transducers were developed and applied to both isotropic and anisotropic multilayer composite structures. Research on phased arrays with nonlinear phase delays has also been carried out, together with development of a phased array circuit that is particularly suitable for guided wave phased array applications.

Composite plates

Quasi-isotropic Carbon/epoxy composite plates were selected as example structures in this project to represent aircraft fuselage and wing skins and to demonstrate the guided wave SHM technique. The number of layers of the composite plates was 8 or 16. The layup sequence for the 8 layer composite plate was $[0/45/90/-45]_s$, whereas for the 16 layer one, the layup sequence was $[(0/45/90/-45)_s]_2$. The composite plates were fabricated in Penn State using Cytec CYCOM IM7/977-3 Carbon/epoxy prepregs. Hand layup and vacuum bagged autoclave curing was employed in the plate fabrication. The averaged ply thickness of the plates was measured at 0.2 mm. The measured density of the plates was 1.608 g/cc. The elastic properties of the IM7/977-3 single lamina found in reference [Schoeppner 2001] are listed in Table 1.

Table 1: Elastic properties of the IM7/977-3 lamina

E_1	172 GPa
$E_2=E_3$	9.8 GPa
G_{23}	3.2 GPa
$G_{12}=G_{13}$	6.1 GPa
ν_{23}	0.55
$\nu_{12}=\nu_{13}$	0.37

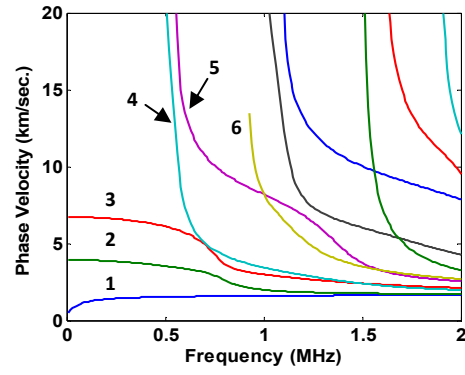
Wave mechanics studies

Guided wave mechanics for traction free plates serves as a fundamental basis for all of the problems that utilize plate waves. Dispersion curves, wave structures, and other free wave characteristics are essential in guided wave applications. The investigation of guided wave excitation as well as wave scattering is also set forth from the free wave solutions.

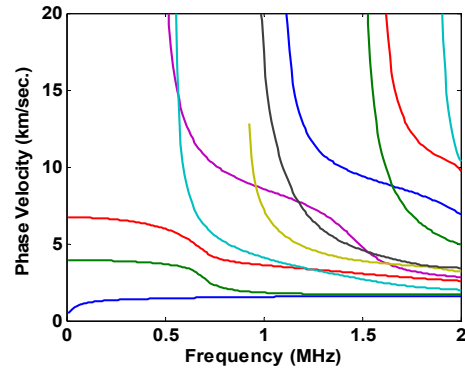
In this project, we employed a SAFE (Semi-Analytical Finite Element) computational method in our guided wave mechanics studies for traction free composite plates. The SAFE method adopts a harmonic exponential term $e^{i(kx-\omega t)}$ to describe the wave behavior in the wave propagation direction, where x represents the wave propagation direction, k represents the wave number, ω represents the radial frequency, and t is the time term. For anisotropic wave guides, it is possible to have different propagation directions for phase velocity and energy velocity. To avoid confusion, the wave propagation direction of phase velocity is named wave vector direction hereafter. The finite element discretization of the SAFE method takes place at the cross section of the wave guide that is perpendicular to the wave vector direction.

For the problem of plane wave propagation in a plate, a one-dimensional discretization across the plate thickness is sufficient. The displacements, strains, and stresses within a finite element can then be expressed as functions of the nodal displacements whose variations in the wave vector direction x satisfies the harmonic exponential assumption. A general eigenvalue problem can be formed after submitting the harmonic wave expressions into the governing equation for elastic wave motions and applying the finite element assembly. Well developed eigenvalue solvers can then be employed to seek the eigenvalues that corresponds to the dispersion relations and the eigenvectors that provide information on the wave structures [Hayashi 2003]. Compared to the conventional global matrix methods or transfer matrix methods [Thomson 1950], [Knopoff 1964] for solving the dispersion curves and wave structures, the SAFE method avoids the root searching procedure and thus is more numerically stable. Moreover, it is more convenient to implement material viscoelasticity in to a SAFE calculation since the complex domain root searching becomes even more difficult when dealing with viscoelastic wave guides [Bartoli 2006], [Gao 2007].

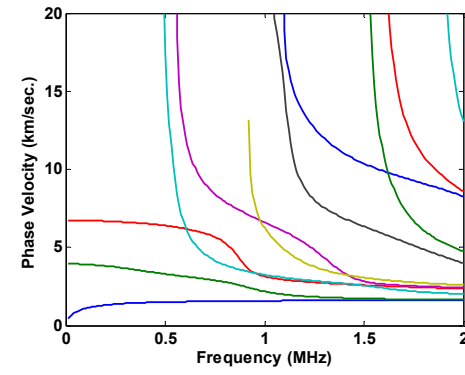
The phase velocity dispersion curves calculated using the SAFE method for the 0° , 30° , and -30° wave vector directions in the 8 layer quasi-isotropic composite plate are given in Figure 1 (a), (b), and (c), respectively. As can be seen, due to the material anisotropy, the dispersion curves are different for all three wave vector directions. Besides, the decoupling between Lamb waves and SH waves in single isotropic plates no longer exists for the composite plate. The wave mode numbering system proposed in [Gao 2007] is used in this work to name guided wave modes in composites. The three fundamental modes with no cut-off frequencies are named modes 1 to 3 based on the values of phase velocities at low frequency. Higher order modes starting from mode 4 are numbered based on their cut-off frequencies for the 0° wave vector direction. The first 6 modes are labeled with their names in Figure 1. The corresponding group velocity dispersion curves are shown in Figure 2. It should be noticed that when using the SAFE method, it is critical to check the convergence of the results. Generally, more nodes are needed in SAFE calculations to accurately represent the wave modes whose wave structures are of larger variations across the plate thickness. The guided wave calculations presented in this report were always conducted with enough elements to ensure convergence. The convergence was achieved when the dispersion curves did not change when increasing the number of elements.



(a)

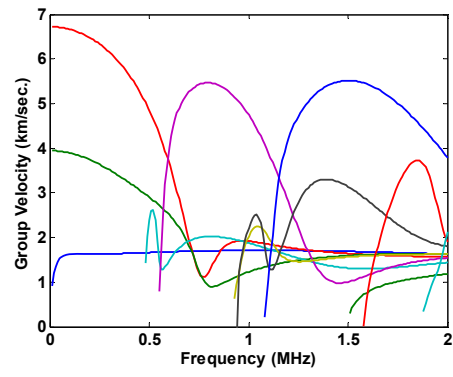


(b)

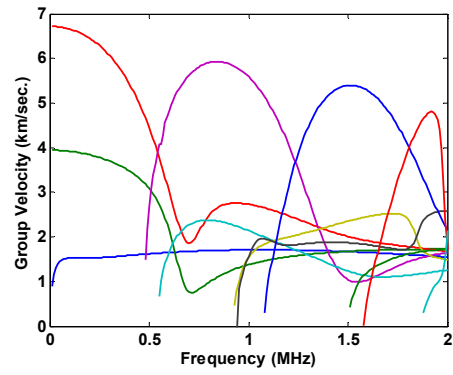


(c)

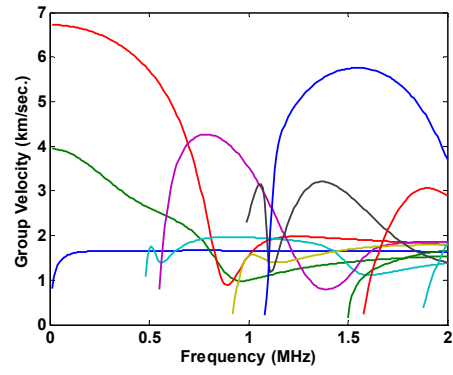
Figure 1: Phase velocity dispersion curves of the 8 layer quasi-isotropic plate for the wave vector directions of (a) 0° , (b) 30° , and (c) -30° .



(a)



(b)



(c)

Figure 2: Group velocity dispersion curves of the 8 layer quasi-isotropic plate for the wave vector directions of (a) 0° , (b) 30° , and (c) -30° .

Example wave structures for guided wave modes propagating in the 0° direction are presented in Figure 3.

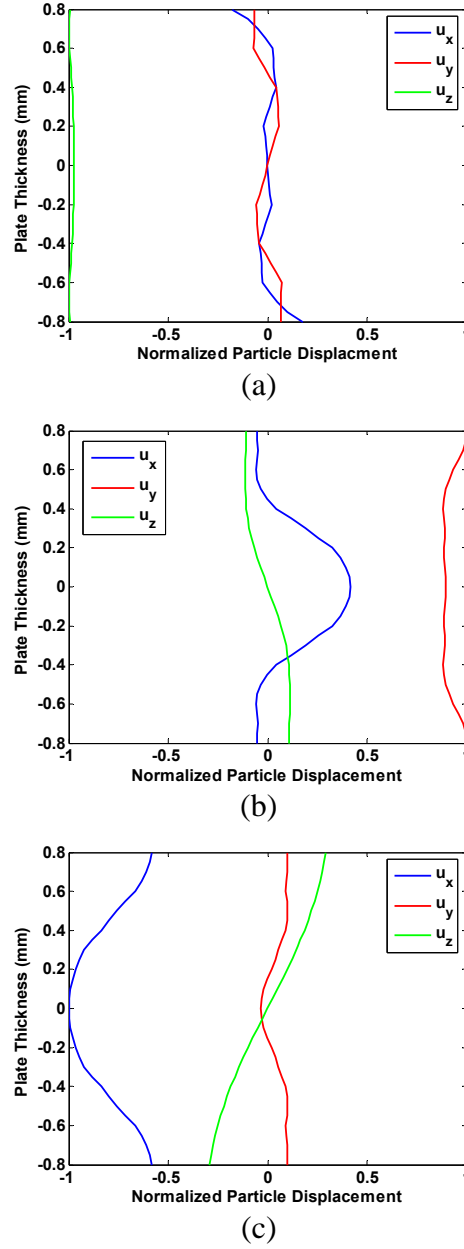
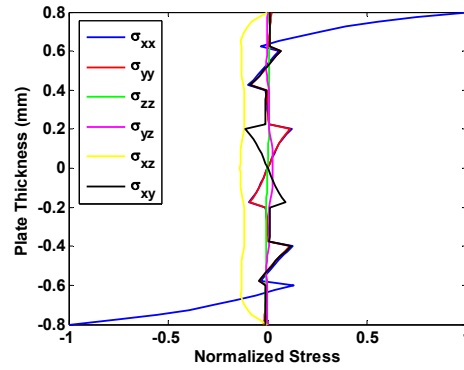


Figure 3: Example wave structures of the three fundamental modes at 500 kHz. (a) mode 1, (b) mode 2, (c) mode 3.

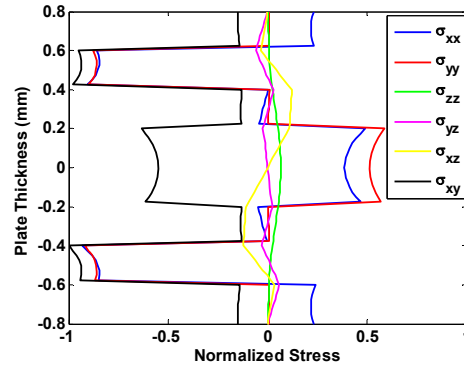
As demonstrated in Figure 3, wave structures vary dramatically from one mode to the other even though the frequencies are the same. Since guided wave modes with different wave structures are sensitive to different types of defects, the great variations of wave structures among different guided wave modes and frequencies offer an excellent flexibility in guided

wave NDE and SHM applications. The wave structures shown in Figure 3 have nonzero displacements in all three displacement directions, whereas in isotropic plates, Lamb waves only have displacements in x and z directions and SH waves have y direction displacements only. Nevertheless, analogies between the guided wave modes in the composite plate and the wave modes in isotropic plates can still be observed. For instance, the wave structure of mode 1 in the composite plate has dominant out-of-plane displacement (u_z) which makes mode 1 similar to the Lamb wave mode A0 in isotropic plates. Similarly, mode 2 and mode 3 have analogies with the SH0 mode and the S0 mode, respectively. Due to the analogies based on wave structures, the fundamental wave modes in the composite plate possess somewhat similar characteristics as the A0, S0, and SH0 modes in isotropic plates when considering wave excitabilities.

The stress distributions across the plate thickness for the three fundamental modes of the composite plate at 500 kHz are shown in Figure 4. As shown, the calculated stress components σ_{xz} , σ_{yz} , and σ_{zz} vanish at the plate surfaces, which satisfies the traction free boundary conditions. They also satisfy the continuity interface conditions between different layers of the composite plate. The correctness of the SAFE calculations is thus verified.



(a)



(b)

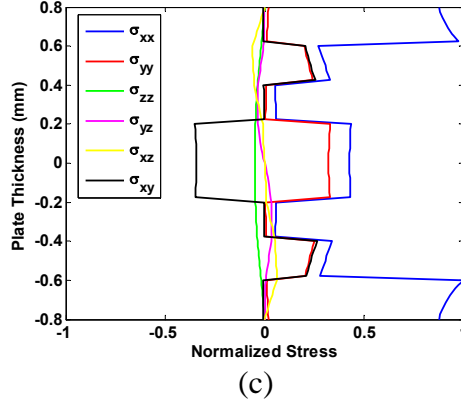


Figure 4: Stress distributions of the three fundamental modes at 500 kHz. (a) mode 1, (b) mode 2, (c) mode 3.

Starting from an electromagnetic-acoustic analogy, B.A. Auld derived an acoustic Poynting vector that represents the power flow density vector of acoustic waves in solids [Auld 1971a]. The acoustic Poynting vector is not only useful for investigating guided wave energy but also plays an important role in guided wave field normalization, guided wave excitability studies, as well as skew angle determination for anisotropic wave guides. The complex Poynting vector can be calculated from the particle velocity and stress fields based on the following equation:

$$\mathbf{P} = -\frac{\tilde{\mathbf{v}} \cdot \boldsymbol{\sigma}_M}{2}, \quad (1)$$

where $\tilde{\mathbf{v}}$ represents the conjugate of particle velocity vector and $\boldsymbol{\sigma}_M$ represents the stress matrix of format:

$$\boldsymbol{\sigma}_M = \begin{bmatrix} \sigma_{xx} & \sigma_{xy} & \sigma_{xz} \\ \sigma_{yx} & \sigma_{yy} & \sigma_{yz} \\ \sigma_{zx} & \sigma_{zy} & \sigma_{zz} \end{bmatrix} \quad (2)$$

For plate wave guides, the three components of the Poynting vector provide us with the power flow densities of a guided wave mode in three orthogonal directions. An integral of \mathbf{P}_x (the component in the wave vector direction) across the plate thickness yields the power flow carried by the guided wave mode in the wave vector direction.

If material anisotropy is not present, all three components of the second row in the stress matrix vanish for plane wave assumption. In this case, the Poynting vector only has two nonzero components P_x and P_z for the wave vector direction and the plate thickness direction, respectively. For the cases of anisotropic plates, however, the P_y component becomes nonzero

for some wave modes. The nonzero P_y component introduces wave skew effects to the guided wave modes. The skew angles can be calculated based on the equation given below:

$$\varphi_{skew} = \tan^{-1} \left(\frac{\int_d P_y dz}{\int_d P_x dz} \right) \quad (3)$$

The skew angle dispersion curves calculated based on Eq. (3) are shown in Figure 5. The integrations in Eq. (3) were evaluated numerically. The wave vector direction was 0° .

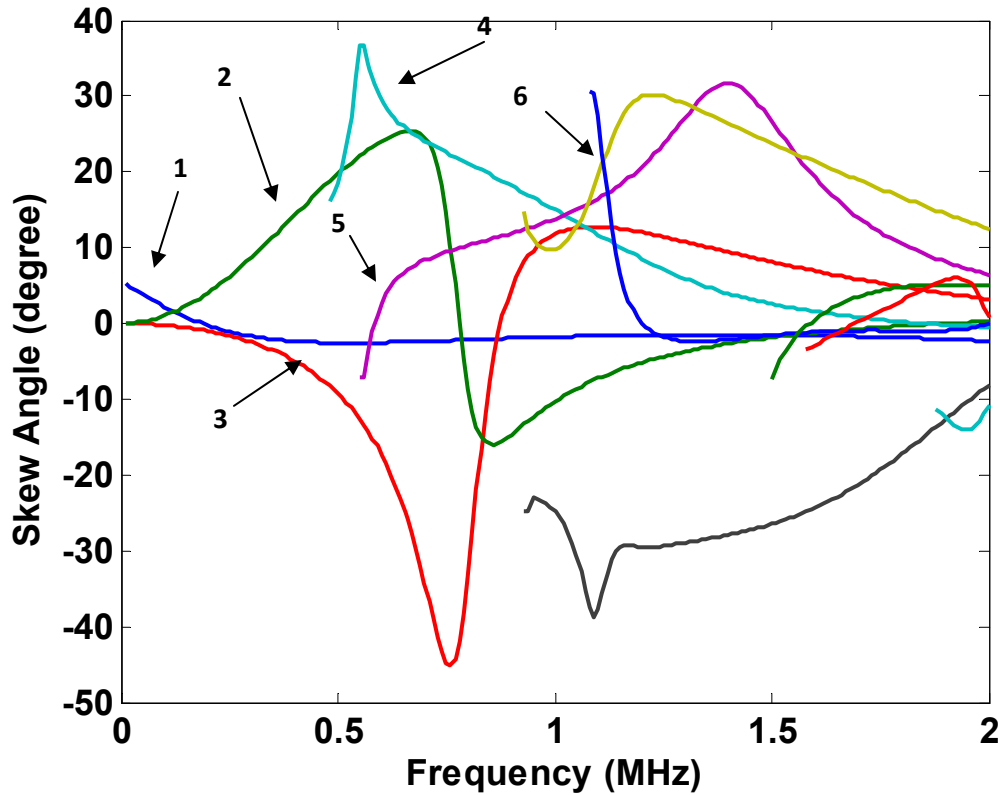


Figure 5: Skew angle dispersion curves of the composite plate for the 0° wave vector direction. Modes 1-6 are labeled.

Although the composite plate was of a quasi-isotropic stacking sequence, the skew angles introduced by the material anisotropy actually varied in a large range roughly from -45 degrees to 38 degrees. For guided wave modes with nonzero skew angles, the wave energies propagate in the directions that are away from the wave vector direction. Hence, a careful investigation on wave skew effects is necessary in guided wave applications for anisotropic wave guides.

Guided wave excitation by SHM sensors

The dispersion curves obtained in the free guided wave solutions showed that there are an infinite number of guided wave modes for a plate. In order to excite the guided wave modes, a loading source needs to be applied to the plate. The forced guided wave solutions then become critical for the understanding of the source influence on the excitation of different guided wave modes. The high sensitivity and accuracy of guided wave inspections can be achieved only if the knowledge of what guided wave modes will be excited by the loading source is established. As an inverse problem, guided wave transducers as well as controlled guided wave inspection techniques can be developed by implementing the guided wave excitation studies into the developments of the transducers and the inspection techniques.

Source influence for straight-crested plane waves

The free guided wave solutions presented previously were obtained by assuming that the width of the plate is infinite in the y direction such that the plane strain assumption is used. The guided waves propagate in the x direction. The source influence study can be started from the problem of guided wave excitation by a surface loading source. The problem geometry is depicted in Figure 6. The loading source is elongated in the width direction (y direction) toward infinity such that straight-crested plane waves are excited in the plate.

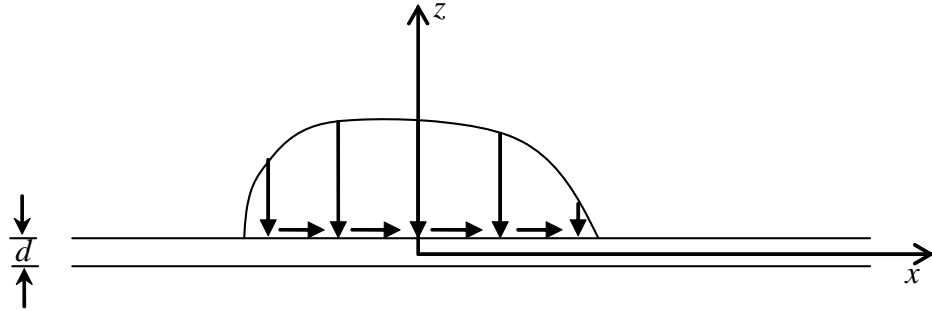


Figure 6: A surface loading source on a plate (after [Ditri 1994a]).

Based on the normal mode expansion technique ([Auld 1971a], [Ditri 1994a], [Auld 1971b], [Kino 1987]), the guided wave field excited by the source can be expanded into a combination of different guided wave modes:

$$\mathbf{v}(x, z) = \sum_{\mu} A_{\mu}(x) \bar{\mathbf{v}}_{\mu}(z), \quad (4)$$

$$\mathbf{T}(x, z) = \sum_{\mu} A_{\mu}(x) \bar{\mathbf{T}}_{\mu}(z), \quad (5)$$

where \mathbf{v} represents the particle velocity field, \mathbf{T} represents the stress field, $\bar{\mathbf{v}}_\mu$ and $\bar{\mathbf{T}}_\mu$ respectively represent the particle velocity and stress distributions across the thickness of the plate that can be derived from the wave structures of the μ th mode, and $A_\mu(x)$ represents the amplitude factor for the μ th mode. Notice that the time harmonic dependence of the wave field is dropped for brevity. By applying the orthogonality relation among different wave modes and also the boundary conditions, one can show that the amplitude factor in Eqs. (4) and (5) can be evaluated using the following equation [Ditri 1994a]:

$$A_\mu(x) = \frac{e^{i\tilde{k}_\mu x}}{4P_{\mu\mu}} \int_{-\infty}^{\infty} e^{-i\tilde{k}_\mu \eta} \tilde{\mathbf{v}}_\mu(d/2) \cdot \mathbf{t}(\eta) d\eta, \quad (6)$$

where \mathbf{t} denotes the traction applied on the top surface of the plate, the tilde represents complex conjugation, and $P_{\mu\mu}$ can be calculated as:

$$P_{\mu\mu} = \text{Re} \left(-\frac{1}{2} \int_{-d/2}^{d/2} \tilde{\mathbf{v}}_\mu \cdot \mathbf{T}_\mu \cdot \hat{\mathbf{e}}_x dz \right), \quad (7)$$

which corresponds to the x component of the Poynting's vector.

Based on Eq. (7), the displacement field of the μ th mode can be expressed as:

$$\mathbf{u}_\mu = \left[\frac{\tilde{\mathbf{v}}_\mu(d/2)}{4P_{\mu\mu}} \cdot \int_{-\infty}^{\infty} \mathbf{t}(\eta) e^{-i\tilde{k}_\mu \eta} d\eta \right] \bar{\mathbf{u}}_\mu(z) e^{i(\tilde{k}_\mu x - \omega t)}. \quad (8)$$

The harmonic time dependence of the displacement field is put back in Eq (8). The displacement field on the surface where the load is applied can then be expressed as a dot product of a matrix and a vector:

$$\mathbf{u}_\mu(d/2) = \left[\mathbf{E}_\mu \cdot \int_{-\infty}^{\infty} \mathbf{t}(\eta) e^{-i\tilde{k}_\mu \eta} d\eta \right]^T e^{i(\tilde{k}_\mu x - \omega t)}, \quad (9)$$

In which the matrix \mathbf{E}_μ is the multiplication of two vectors:

$$\mathbf{E}_\mu = \frac{[\bar{\mathbf{u}}_\mu(d/2)]^T}{4P_{\mu\mu}} \times \tilde{\mathbf{v}}_\mu(d/2). \quad (10)$$

The matrix \mathbf{E}_μ is defined as the excitability matrix of the μ th mode in this report.

If, for example, an in-plane line source is applied on the top surface of the plate at $x=0$, the loading traction is expressed as

$$\mathbf{t}(x) = t_x \delta(x) \hat{\mathbf{e}}_x. \quad (11)$$

The integral term included in Eq. (9) becomes:

$$\int_{-\infty}^{\infty} \mathbf{t}(\eta) e^{-i\tilde{k}_\mu \eta} d\eta = t_x \hat{\mathbf{e}}_x. \quad (12)$$

Based on Eqs. (9), (10), and (12), it is straightforward to calculate the surface in-plane displacement of an excited guided wave mode:

$$u_{x\mu}(d/2) = -it_x E_{xx\mu} e^{i(\tilde{k}_\mu x - \omega t)}, \quad (13)$$

where $E_{xx\mu}$ is one element of the excitability matrix:

$$E_{xx\mu} = \frac{\omega}{4P_{\mu\mu}} [\bar{u}_{x\mu}(d/2)]^2. \quad (14)$$

Physical insights on the guided wave excitation can be obtained from Eq. (14) in which the excitability is proportional to the square of power flow normalized surface displacement component in the direction of the applied traction. In other words, wave modes whose wave structures “match” the applied traction more intend to have higher excitability.

Excitation of circular-crested guided waves by point sources

In many guided wave SHM applications, the transducers have dimensions that are smaller than the wavelength of the guided wave mode. In these cases, the assumption in the strip type loading adopted in the previous source influence study for the straight-crested plane waves becomes invalid. Circular-crested waves are the type of waves excited by the transducers.

The schematic drawing of the circular-crested waves excited by a point source is given in Figure 7. A cylindrical coordinate system is used. The origin of the cylindrical coordinate system locates at the center of the plate. The point source is applied at the center of the top surface of the plate at which the coordinates are $(r=0, z=d/2)$.

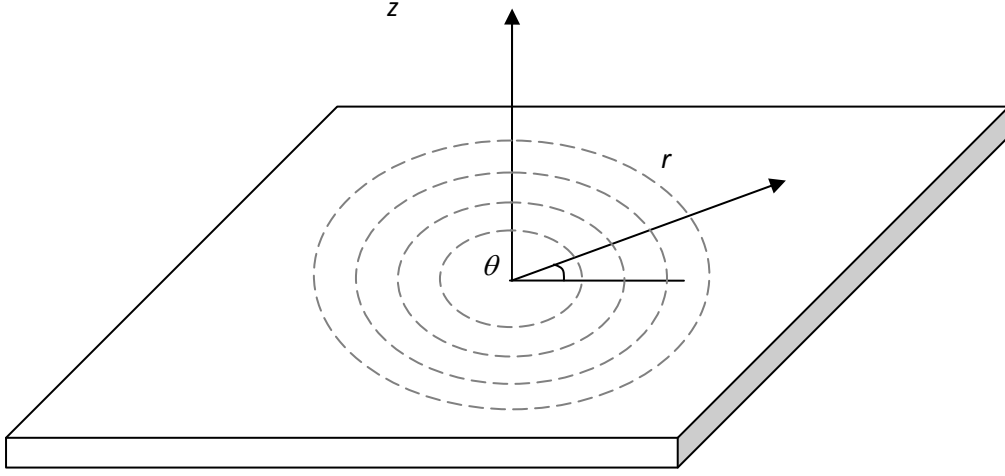


Figure 7: Schematic drawing of the circular-crested waves excited by a point source.

On the basis of the derivation for wave motion generated by a time-harmonic point load [Achenbach 1999], [Ditri 1994b], Wilcox was able to link the point excitations of circular-crested waves to the line excitations of straight-crested waves [Wilcox 2004], [Wilcox 2005]. From Eqs. (13) and (14), the guided wave surface displacement fields of the ν th mode excited by line sources can be derived as:

$$\mathbf{u}_\nu(d/2) = [\mathbf{E}_\nu \cdot (t_x \hat{\mathbf{e}}_x, t_y \hat{\mathbf{e}}_y, t_z \hat{\mathbf{e}}_z)^T]^T e^{i(k_\nu x - \omega t)}, \quad (15)$$

where the conjugate of the wavenumber \tilde{k}_ν is replaced by k_ν for propagating wave modes. Based on Wilcox's work, the guided wave surface displacement fields excited by out-of-plane point sources applied to the point ($r=0, z=d/2$) or in-plane point sources applied to the same point in the $\theta = 0$ direction can be expressed as:

$$\mathbf{u}_\nu(d/2) = [\mathbf{E}_\nu^{(3D)} \cdot (t_r \hat{\mathbf{e}}_r, t_\theta \hat{\mathbf{e}}_\theta, t_z \hat{\mathbf{e}}_z)^T]^T H_0^{(1)}(k_\nu r) e^{-i\omega t}, \quad (16)$$

where $\mathbf{E}_\nu^{(3D)}$ is a 3D excitability matrix for point sources whose components are linked to the components of the \mathbf{E}_ν matrix given in Eq. (15) through the following equations:

$$E_{rr\nu}^{(3D)} = \frac{ik_\nu}{2} E_{xx\nu} \cos(\theta), \quad (17)$$

$$E_{r\theta\nu}^{(3D)} = 0, \quad (18)$$

$$E_{rz\nu}^{(3D)} = \frac{ik_\nu}{2} E_{xz\nu}, \quad (19)$$

$$E_{\theta r\nu}^{(3D)} = \frac{ik_\nu}{2} E_{yy\nu} \sin(\theta), \quad (20)$$

$$E_{\theta\theta\nu}^{(3D)} = 0, \quad (21)$$

$$E_{\theta z\nu}^{(3D)} = 0, \quad (22)$$

$$E_{zr\nu}^{(3D)} = \frac{ik_\nu}{2} E_{zx\nu} \cos(\theta), \quad (23)$$

$$E_{z\theta\nu}^{(3D)} = 0, \quad (24)$$

$$E_{zz\nu}^{(3D)} = \frac{ik_\nu}{2} E_{zz\nu}. \quad (25)$$

It is shown that the spatial variation of the circular-crested Lamb waves is described by a first kind Hankel function of zero order rather than the exponential function for the straight-crested waves. The Hankel function captures the decay of the Lamb waves as the waves travel outwards from the source. It is also important to know that the circular-crested Lamb waves in plates satisfy the same dispersion relations as the straight-crested Lamb waves do [Achenbach 1999], [Wilcox 2005]. The connections between the matrices $\mathbf{E}_\nu^{(3D)}$ and \mathbf{E}_ν , nevertheless, are valid except for the very near field of the source. In our guided wave SHM applications, the interests are generally placed outside the very near fields of the transducers. Therefore, Eqs. (17)-(25) are applicable in SHM applications. Since any source loading applied to the surface of the plate can be decomposed into a combination of the out-of-plane and in-plane point sources based on Huygen's principle, Eqs. (17)-(25) can be used to predict the guided wave fields excited by any surface loading.

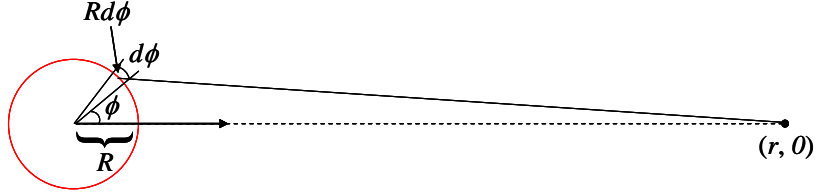
Guided wave excitation of PWAS in isotropic plates

Piezoelectric Wafer Active Sensors (PWAS) have been extensively used in ultrasonic guided wave SHM applications due to their small size, light weight, and low cost. It was revealed that the interaction between an attached PWAS and the host structure behaves as interfacial shear stresses locating only at the edge of the PWAS if the bonding layer is thin and rigid [Giurgiutiu 2005]. Therefore, we can consider the loading of an attached PWAS as an axisymmetric in-plane loading located at the circle of the disk edge. The guided wave field excited by this axisymmetric in-plane loading can be predicted by integrating the in-plane point source solution along the circle of the disk edge.

As can be obtained from Figure 8, the in-plane surface particle displacement in the r direction of wave mode ν at the position $(r, 0)$ excited by a small portion $Rd\phi$ of the disk can be written as:

$$du_{r\nu} = \frac{ik_\nu}{2} E_{xx\nu} \cos(\phi) H_0^{(1)}[k_\nu(r - R\cos(\phi))] \rho_{Tr} Rd\phi, \quad (26)$$

where R is the radius of the disk and ρ_{Tr} represents the line density of the in-plane traction.



Leave-in-Place Piezoelectric Disk Transducer

Figure 8: Geometry of far field wave excitation by a leave-in-place piezoelectric disk transducer.

The in-plane displacement excited by the whole disk is an integral of $du_{r\nu}$ along the disk edge:

$$u_{r\nu} = \frac{ik_\nu}{2} E_{xx\nu} \rho_{Tr} R \int_0^{2\pi} \cos(\phi) H_0^{(1)}[k_\nu(r - R\cos(\phi))] d\phi. \quad (27)$$

After applying the asymptotic form of Hankel function for large parameters, we obtain an asymptotic solution of $u_{r\nu}$:

$$\begin{aligned} u_{r\nu} &\approx \sqrt{\frac{i}{2\pi}} \rho_{Tr} R \frac{\exp(ik_\nu r)}{\sqrt{r}} \left\{ \sqrt{k_\nu} E_{xx\nu} \int_0^{2\pi} \cos(\phi) \exp(-ik_\nu R \cos(\phi)) d\phi \right\} \\ &= -i \sqrt{\frac{2\pi k_\nu}{r}} \rho_{Tr} R \{E_{xx\nu} J_1(k_\nu R)\} \exp(ik_\nu r) \end{aligned} \quad (28)$$

The corresponding out-of-plane displacement $u_{z\nu}$ is of form:

$$u_{z\nu} \approx -i \sqrt{\frac{2\pi k_\nu}{r}} \rho_{Tr} R \{E_{zx\nu} J_1(k_\nu R)\} \exp(ik_\nu r). \quad (29)$$

Special attention needs to be paid to the fact that the θ direction in-plane displacement excited by the small portion $Rd\phi$ of the disk is nonzero since $E_{\theta r\nu}^{(3D)}$ given in Eq. (20) does not vanish. The displacement $du_{\theta\nu}$ generated by $Rd\phi$ is as follows:

$$du_{\theta\nu} = -\frac{ik_\nu}{2} E_{yy\nu} \sin(\phi) H_0^{(1)}[k_\nu(r - R\cos(\phi))] \rho_{Tr} R d\phi. \quad (30)$$

The point source defined by $Rd\phi$ hence excites not only Lamb type circular-crested waves but also SH type waves. However, it is not hard to show that the integral of $du_{\theta\nu}$ along the circle given by the disk edge equals to zero, i.e.,

$$\int_0^{2\pi} -\frac{ik_\nu}{2} E_{yy\nu} \sin(\phi) H_0^{(1)}[k_\nu(r - R\cos(\phi))] \rho_{Tr} R d\phi = 0. \quad (31)$$

As a result, the disk transducer only excites circular-crested Lamb waves. The Lamb wave displacement fields given by Eqs. (28) and (29) are comparable to the ones derived using the Hankel transform in [Raghavan 2004].

Finite element (FE) analysis has been extensively used for guided wave problems. As a numerical method, FE analysis is capable of dealing with complex wave guide geometries and wave scattering problems whose closed form solutions are not available or hard to obtain. FE analysis can also be applied as a numerical experiment method to validate guided wave theories as well as to provide visualization of guided wave propagation and scattering. In this project, we have employed a commercially available FE software package Abaqus Explicit to model the guided wave excitation of the PWAS and have compared the FEA results with the theoretical solutions derived previously.

Based on the theoretical derivations, the guided wave displacements excited by a leave-in-place PWAS can be evaluated using Eqs. (28) and (29). These two equations are suitable for calculating the displacements for a single frequency. In practical applications and also numerical experiments performed by FE models, the applied loads are generally described by short pulses or tone-burst signals. Hence, the time domain loading signals need to be transformed into frequency domain using a Fourier transform before applying Eqs. (28) and (29). For the ease of comparing to experimental results or FE analysis results, the contributions of the different frequency components of the applied signals are subject to a transformation back to the time domain. The transformation can be carried out using the following equations:

$$u_z(r, t) = \sum_{\omega} u_z(r, \omega, t) F(\omega), \quad (32)$$

$$u_r(r, t) = \sum_{\omega} u_r(r, \omega, t) F(\omega), \quad (33)$$

where $F(\omega)$ is the amplitude factor of the frequency component ω which is available in the Fourier transform result.

In the FE analysis, since the guided wave fields excited by the out-of-plane point source were axisymmetric, the 2-dimensional axisymmetric model in Abaqus can be used. The sketch of the

FE model defined in ABAQUS is shown in Figure 9. The plate was a 1 mm thick aluminum plate. The radius of the PWAS was 4 mm. The load provided by a PWAS was described as shear traction acting at the edge of the transducer. A unit in-plane force was applied to represent the transducer load. The traction density ρ_{Tr} in Eqs. (28) and (29) was $1/2\pi R$ for this case. The amplitude of the applied force was defined by a 5 cycle 300kHz Hanning windowed tone-burst signal. Two particle displacement measurement points were defined at the distance of 0.1m from the axisymmetric axis on the upper and lower surfaces of the plate, respectively. The time history records of the particle displacements at the displacement measurement points were obtained in the FE analysis.

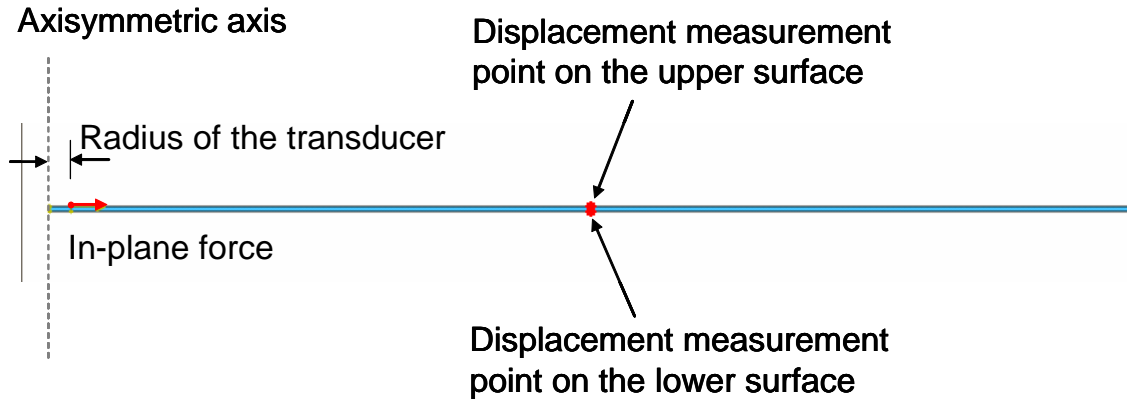


Figure 9: Axisymmetric FE model for a PWAS attached to the surface of a 1mm thick aluminum plate. The radius of the transducer is 4mm.

The time histories of the particle displacements at the measurement points contain the information for both the A0 mode and the S0 mode. Thanks to the symmetries in wave structures, the A0 mode and the S0 mode can be separated using the following equations:

$$u_{xA0}(t) = u_{xUp}(t)/2 - u_{xLow}(t)/2, \quad (34)$$

$$u_{zA0}(t) = u_{zUp}(t)/2 + u_{zLow}(t)/2, \quad (35)$$

$$u_{xS0}(t) = u_{xUp}(t)/2 + u_{xLow}(t)/2, \quad (36)$$

$$u_{zS0}(t) = u_{zUp}(t)/2 - u_{zLow}(t)/2, \quad (37)$$

where u_{xUp} and u_{xLow} represent the in-plane displacement signals recorded from the upper and lower surfaces of the plate, respectively. u_{zUp} and u_{zLow} are the corresponding out-of-plane displacement signals.

The in-plane displacements excited by the PWAS were obtained by the FE analyses for both A0 and S0 modes and then were compared to the ones calculated from the closed form solutions given in Eqs. (28) and (29). The results are presented in Figures 10 and 11 for the A0 and the S0 modes, respectively.

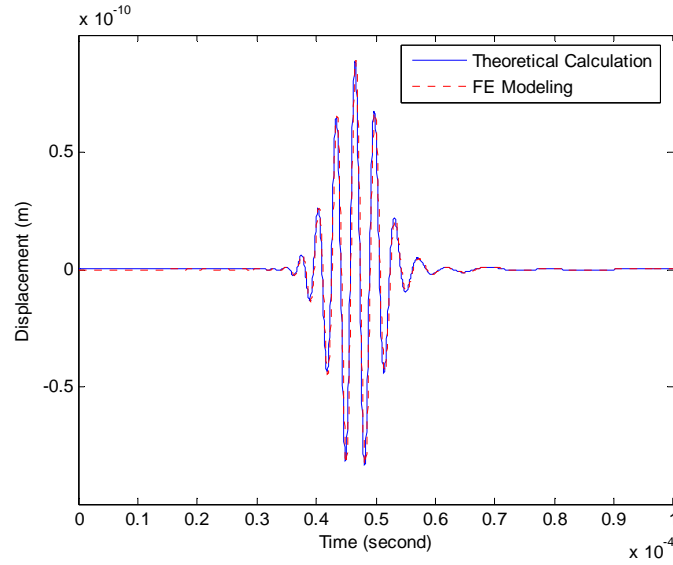


Figure 10: Comparison between theoretical calculation and FE modeling on the in-plane displacement of the A0 mode for the 4mm radius PWAS.

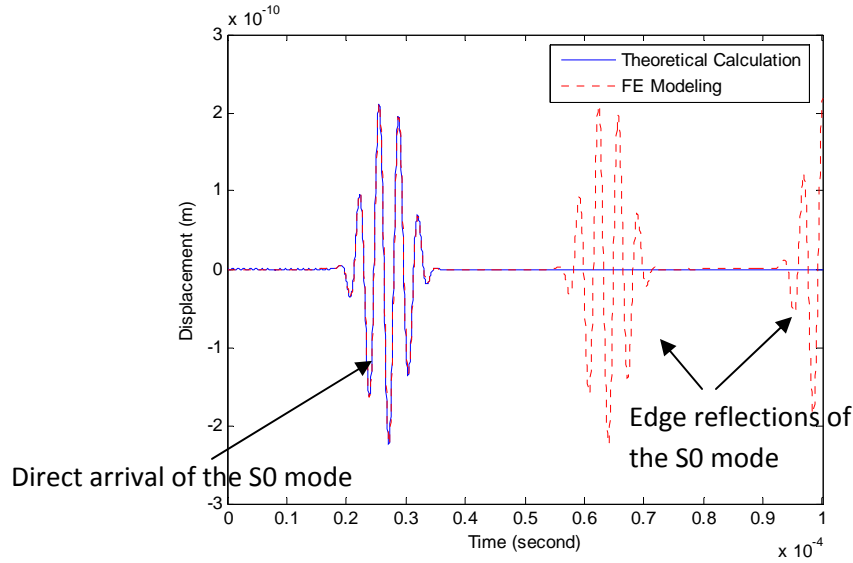


Figure 11: Comparison between theoretical calculation and FE modeling on the in-plane displacement of the S0 mode for the 4mm radius PWAS.

As demonstrated in Figure 10, the in-plane displacements of the A0 mode calculated from the theoretical calculation and from the FE modeling match quite well. The result for the S0 mode calculated from the FE modeling, as shown in Figure 11, has not only direct arrival signals of the S0 mode at the measurement points, but also contains the edge reflections of the S0 mode. An excellent match between the theoretical calculation and the FE modeling can be observed for the direct arrival signal. Hence, the theoretical derivations for the point source guided wave excitation are validated by the FE modeling. Comparing to the FE analyses, the closed form solutions not only offer computational efficiency but also avoid the presence of numerical calculation errors and reflection signals that could introduce difficulties for signal analyses in FE modeling.

When using the PWAS as SHM sensors, especially when using it as a phased array element, it is critical to know the guided wave excitations of the transducers at different frequencies. The magnitudes of the in-plane displacements given in Eq. (28) are plotted in Figure 12 for different frequencies. As can be seen, the excitations of the A0 mode and the S0 mode vary differently with respect to the frequency change. As a result, it is possible to control the ratio of the A0 mode to the S0 mode by selecting different operating frequencies. The frequency domain representations of the in-plane displacements obtained from the FE analysis are also plotted in Figure 12. To avoid numerical errors, the frequency domain representations are only calculated for the frequencies within the 6dB bandwidth of the input excitation signal: the 5 cycle Hanning windowed tone-burst signal. Apparently, the derived closed form solutions can be applied to correctly evaluate the frequency domain representations for a large frequency range in a computational effective way.

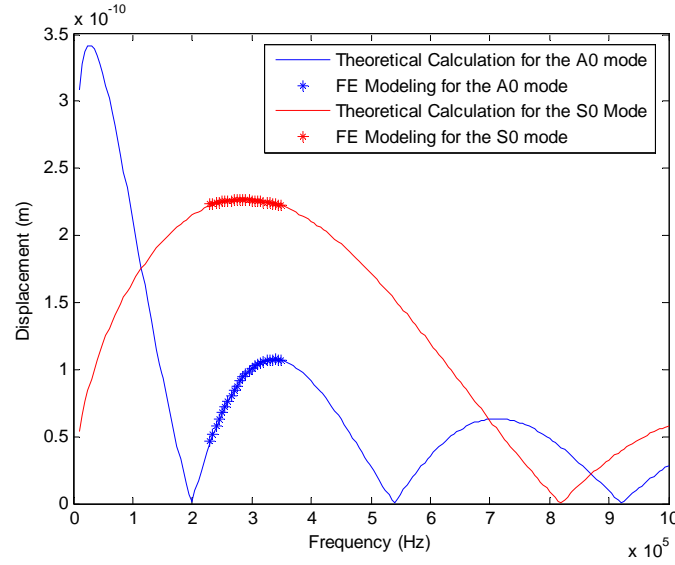


Figure 12: Frequency domain comparison between theoretical calculation and FE modeling on the in-plane displacements for the 4mm radius leave-in-place piezoelectric disk transducer.

In guided wave phased array applications, it is important to ensure a single wave mode excitation such that the influence of unwanted wave modes can be eliminated. When using the PWAS as an array element, to optimize the radius and operating frequency of the PWAS under consideration of controlling the influence of unwanted wave modes, it is critical to understand the variation of the wave excitations with respect to the change of both the radius and the operating frequency. Evaluating Eq. (28) at different frequencies for different PWAS transducer radiuses, one can plot the in-plane displacement spectrums in a frequency-radius domain. The normalized in-plane displacement spectrums for a 1mm thick aluminum plate are shown in Figure 13 for the A0 and the S0 wave modes. The normalized in-plane displacement spectrum is named guided wave mode selection spectrum here based on the fact that the mode selection capability of the transducer is directly revealed in the spectrum.

Notice that the color scales used for Figure 13 (a) and (b) are the same such that the mode selection capabilities for the two modes can be easily compared. For instance, it is easy to observe that the mode selection capability of a 6mm radius transducer for the S0 mode is higher than the one for the A0 mode at 0.2MHz. However, at the same frequency, if a 2mm radius transducer is used, the mode selection capability is higher for the A0 mode.

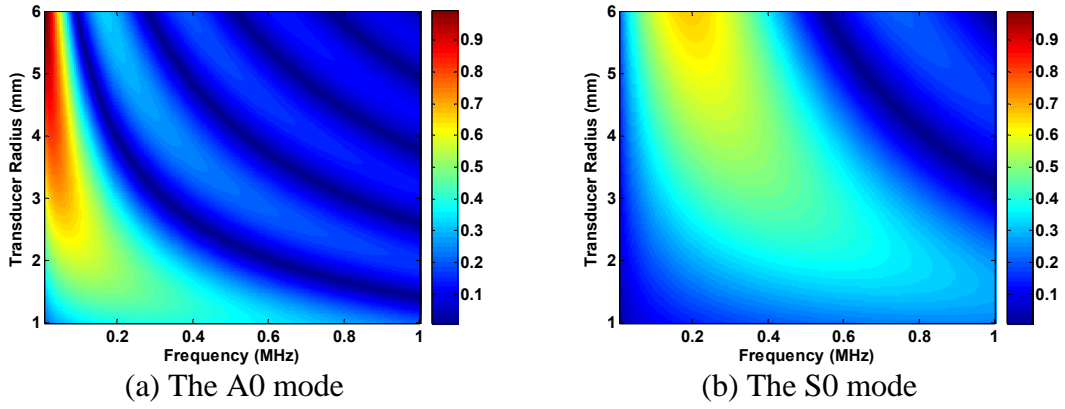


Figure 13: Guided wave mode selection spectra of PWAS for a 1mm thick aluminum plate.

The S0-to-A0-ratio of mode selection capability can be obtained by dividing the mode selection spectrum of the S0 mode by the one of the A0 mode. The spectrum of the S0-to-A0-ratio on mode selection capability for a 1mm thick aluminum plate is presented in Figure 14 in dB scale. From such a spectrum, the regions where the excitation capability of the S0 mode is much higher than the A0 mode can be easily identified. The regions where the excitation capability of the A0 mode is higher than the S0 mode are indicated in the spectrum by negative dB values as well. As a result, the transducer radius and the operating frequency can be chosen according to the spectrum shown in Figure 14 to have one mode excited dominantly over the other and thus control the influence of the unwanted wave mode.

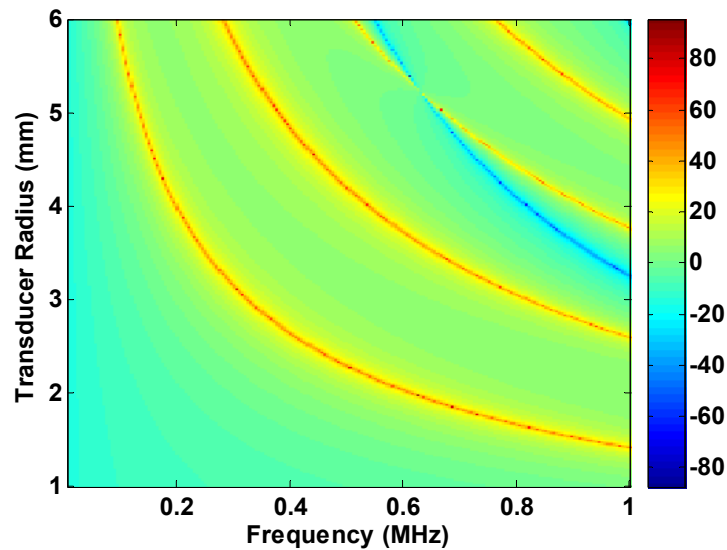


Figure 14: Spectrum of the S0-to-A0-ratio of mode selection capability for a 1mm thick aluminum plate.

Guided wave excitation in composite plates

The problem of guided wave point source excitation becomes much more complex for composite plates. Material anisotropy of composite plates may have Lamb waves and SH waves coupled together such that nonzero particle displacements in all three directions are present in the wave structures of the straight-crested waves. Thus, all of the components of the 2-dimensional excitability matrix defined in Eq. (10) are nonzero. The excitability matrix also depends on the wave propagation direction. The wave skew effects in composite plates bring another extra difficulty as compared to the problem of guided wave point source excitation in isotropic plates. In this report, the asymptotic method proposed in [Velichko 2007] is modified and applied for predicting the guided wave excitations in composite plates.

For 2D straight-crested guided waves, the particle displacement field excited by a surface traction loading as a summation of Eq. (8) with respect to all possible wave modes can be rewritten using a 2D Green's function:

$$\mathbf{u}(x, z, \mathbf{t}) = \left[\int \mathbf{g}(x - \eta, z) \bullet \mathbf{t}(\eta) d\eta \right]^T, \quad (38)$$

where the Green's function is of the form:

$$\mathbf{g}(x, z) = \sum_{\nu} [\bar{\mathbf{u}}_{\nu}(z)]^T \frac{\tilde{\mathbf{v}}_{\nu}(d/2)}{4P_{\nu\nu}} e^{ik_{\nu}x}. \quad (39)$$

Similarly, the particle displacement field excited by an arbitrary surface loading can be described by a 3D Green's function $\mathbf{g}^{(3)}(x', y', z)$ for the rectangular coordinate system shown in Figure 15:

$$\mathbf{u}^{(3)}(x', y', z, \mathbf{t}^{(3)}) = \left[\iint \mathbf{g}^{(3)}(x' - \eta, y' - \varsigma, z) \bullet \mathbf{t}^{(3)}(\eta, \varsigma) d\eta d\varsigma \right]^T. \quad (40)$$

The corresponding wavenumber domain 3D Green's function can be obtained by applying a 2D spatial Fourier transform to the function $\mathbf{g}^{(3)}(x', y', z)$:

$$\mathbf{G}^{(3)}(k'_x, k'_y, z) = \iint \mathbf{g}^{(3)}(x', y', z) e^{-i(k'_x x + k'_y y)} dx' dy'. \quad (41)$$

Since k'_x and k'_y are wavenumbers for straight-crested waves, it is easier to find the connections between the 3D guided wave excitation by the arbitrary surface loading with the 2D straight-crested guided wave excitation in wavenumber domain. The 2D Green's function in wavenumber domain can also be obtained by a 1D spatial Fourier transform:

$$\mathbf{G}(k, z) = \int \mathbf{g}(x, z) e^{-ikx} dx. \quad (42)$$

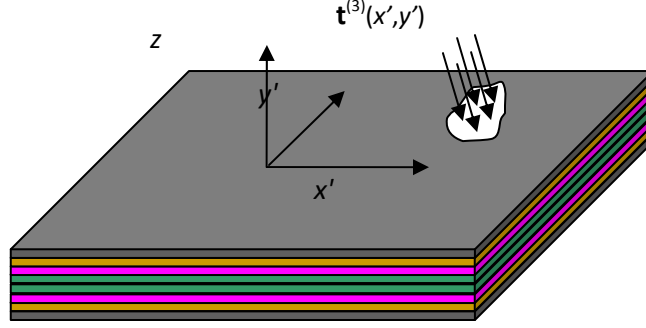


Figure 15: Arbitrary surface loading applied to the surface of a composite plate.

Assume that the angle from the axis x' shown in Figure 15 to the axis x that defines the wave propagation direction of the 2D straight-crested is γ , the coordinate transformation from the 3D wave excitation coordinate system to the one of the 2D wave excitation case can be achieved with the following equation:

$$[x, y, z]^T = \mathbf{A}(\gamma)[x', y', z]^T, \quad \mathbf{A}(\gamma) = \begin{bmatrix} \cos \gamma & \sin \gamma & 0 \\ -\sin \gamma & \cos \gamma & 0 \\ 0 & 0 & 1 \end{bmatrix}. \quad (43)$$

After coordinate transformation, the 3D wavenumber domain Green's function $\mathbf{G}^{(3)}(k'_x, k'_y, z)$ becomes:

$$\mathbf{G}^{(3)}(k_x, k_y, z) = \mathbf{A} \mathbf{G}^{(3)}(k_x \cos \gamma - k_y \sin \gamma, k_x \sin \gamma + k_y \cos \gamma, z) \mathbf{A}^{-1}. \quad (44)$$

It is apparent that if $k_y = 0$, $\mathbf{G}^{(3)}(k_x, k_y, z)$ given in Eq. (44) represents the same straight-crested plane wave as the 2D wavenumber domain Green's function $\mathbf{G}(k, z)$ does. Therefore, the relation between the 3D and the 2D wavenumber domain Green's functions can be written as:

$$\mathbf{A} \mathbf{G}^{(3)}(k_x \cos \gamma, k_x \sin \gamma, z) \mathbf{A}^{-1} = \mathbf{G}(k, z). \quad (45)$$

Such a relation makes it possible to calculate 3D guided wave fields excited by arbitrary surface loadings based on 2D plane wave solutions.

To obtain the 3D Green's function $\mathbf{g}^{(3)}(x', y', z)$ from $\mathbf{G}^{(3)}(k'_x, k'_y, z)$, one can use the inverse 2D spatial Fourier transform:

$$\mathbf{g}^{(3)}(x', y', z) = \frac{1}{4\pi^2} \iint \mathbf{G}^{(3)}(k'_x, k'_y, z) e^{i(k'_x x' + k'_y y')} dk'_x dk'_y. \quad (46)$$

For the convenience of calculating circular-crested guided wave fields, Eq. (46) is transformed to a cylindrical coordinate system as follow:

$$\mathbf{g}^{(3)}(r, \varphi, z) = \frac{1}{4\pi^2} \int_0^{2\pi} \int_0^\infty \mathbf{G}^{(3)}(k \cos \gamma, k \sin \gamma, z) e^{ikr \cos(\gamma - \varphi)} k dk d\gamma. \quad (47)$$

The cylindrical coordinate system (r, φ, z) used in Eq. (47) has the same origin and z axis as the Cartesian coordinate system (x', y', z) does. The x' axis of the Cartesian coordinate system corresponds to $\varphi = 0$ in the cylindrical coordinate system. The integration with respect to k in Eq. (47) can be evaluated using the residue theorem. On the basis of the residue theorem, the integration with respect to k equals the summation of the residues of all poles of the complex integrand $\mathbf{G}^{(3)}(k \cos \gamma, k \sin \gamma, z) k e^{ikr \cos(\gamma - \varphi)}$ in the upper half k plane. Since the complex poles correspond to the evanescent guided wave modes, the residues of them can be omitted for far field solutions. Therefore, the far-field approximation of the integration with respect to k can be written as the summation of the real poles that correspond to propagating guided wave modes:

$$\begin{aligned} & \int_0^\infty \mathbf{G}^{(3)}(k \cos \gamma, k \sin \gamma, z) k e^{ikr \cos(\gamma - \varphi)} dk \\ & \approx 2\pi i \sum_\nu \text{res} \left\{ \mathbf{G}^{(3)}(k \cos \gamma, k \sin \gamma, z) k e^{ikr \cos(\gamma - \varphi)} \right\} \Big|_{k=k_\nu(\gamma)} \\ & = 2\pi i \sum_\nu k_\nu e^{ik_\nu(\gamma) r \cos(\gamma - \varphi)} \text{res} \left\{ \mathbf{G}^{(3)}(k \cos \gamma, k \sin \gamma, z) \right\} \Big|_{k=k_\nu(\gamma)} \end{aligned} \quad (48)$$

The far-field approximation of Eq. (47) then becomes:

$$\mathbf{g}^{(3)}(r, \varphi, z) = \frac{1}{2\pi} \sum_\nu \int_0^{2\pi} \mathbf{G}_\nu^{(3)}(\gamma, z) k_\nu(\gamma) e^{ik_\nu(\gamma) r \cos(\gamma - \varphi)} d\gamma, \quad (49)$$

with

$$\mathbf{G}_\nu^{(3)}(\gamma, z) = i \text{res} \left\{ \mathbf{G}^{(3)}(k \cos \gamma, k \sin \gamma, z) \right\} \Big|_{k=k_\nu(\gamma)}. \quad (50)$$

The method of stationary phase [Hayek 2001], an asymptotic method for integral evaluation, is employed to calculate the integration with respect to angle γ in Eq. (49). The stationary phase points of the integrand, $\gamma_\nu(\varphi)$, are calculated from:

$$\frac{\partial[k_\nu(\gamma)\cos(\gamma-\varphi)]}{\partial\gamma}=0. \quad (51)$$

asymptotic representation of Eq. (49) can then be expressed as:

$$\begin{aligned} \mathbf{g}^{(3)}(r, \varphi, z) &= \frac{1}{2\pi} \sum_\nu e^{ir\Phi_\nu(\gamma_\nu, \varphi)} \mathbf{G}_\nu^{(3)}(\gamma_\nu, z) k_\nu(\gamma_\nu) \sqrt{\frac{2\pi}{r \frac{\partial^2 \Phi_\nu(\gamma_\nu, \varphi)}{\partial \gamma^2}}} e^{i\pi/4}, \\ &= \sqrt{\frac{i}{2\pi r}} \sum_\nu e^{ir\Phi_\nu(\gamma_\nu, \varphi)} \mathbf{G}_\nu^{(3)}(\gamma_\nu, z) k_\nu(\gamma_\nu) \left[\frac{\partial^2 \Phi_\nu(\gamma_\nu, \varphi)}{\partial \gamma^2} \right]^{-1/2} \end{aligned} \quad (52)$$

where

$$\Phi_\nu(\gamma, \varphi) = k_\nu(\gamma) \cos(\gamma - \varphi). \quad (53)$$

The 2D Green's function $\mathbf{g}(x, z)$ can be expressed as the inverse spatial Fourier transform of $\mathbf{G}(k, z)$ as well:

$$\mathbf{g}(x, z) = \frac{1}{2\pi} \int_{-\infty}^{\infty} \mathbf{G}(k, z) e^{ikx} dk. \quad (54)$$

residue theorem is also applicable to Eq. (54). The application of the theorem yields:

$$\mathbf{g}(x, z) = i \sum_\nu e^{ik_\nu x} \text{res} \left\{ \mathbf{G}(k, z) \right\}_{k=k_\nu}. \quad (55)$$

Comparing Eq. (55) to Eq. (39), one can get:

$$i \text{res} \left\{ \mathbf{G}(k, z) \right\}_{k=k_\nu} = [\bar{\mathbf{u}}_\nu(z)]^T \frac{\tilde{\tilde{\mathbf{v}}}_\nu(d/2)}{4P_{\nu\nu}}. \quad (56)$$

The substitution of Eq. (45) and Eq. (56) into Eq. (50) provides us with:

$$\mathbf{G}_\nu^{(3)}(\gamma, z) = \mathbf{A}^{-1} [\bar{\mathbf{u}}_\nu(z)]^T \frac{\tilde{\tilde{\mathbf{v}}}_\nu(d/2)}{4P_{\nu\nu}} \mathbf{A}. \quad (57)$$

Eq. (51), Eq. (52), and Eq. (57) can now be used together to calculate the 3D Green's function $\mathbf{g}^{(3)}(r, \varphi, z)$. Once the 3D Green's function $\mathbf{g}^{(3)}(r, \varphi, z)$ is known, the guided wave field excited

by a surface loading source can be obtained from the convolution of the Green's function with the surface traction of the applied source.

Physical insights on the relation between angle γ_ν and φ defined by Eq. (51) can be gained by substituting $k = \frac{\omega}{c}$ into the equation followed by some algebraic manipulations. The manipulated equation becomes:

$$\varphi = \gamma_\nu + \text{atan}\left(\frac{c'(\gamma_\nu)}{c(\gamma_\nu)}\right), \quad (58)$$

where c' represents the derivative of phase velocity c with respect to angle γ . It is now clear that the angle φ is the group velocity direction for the ν th guided wave mode launched in the γ_ν direction. In other words, the skew effect of the ν th guided wave mode makes angle φ as the energy propagation direction when the wave launching direction is γ_ν . For a certain angle φ within the wave field, Eq. (52) summarizes the contributions of all of the wave modes whose group/energy velocity directions lie in the direction of angle φ . It has been shown in the previous chapter that the skew angles can be evaluated based on the direction of the Poynting vector. In this report, instead of applying numerical differentiation based on Eq. (51), the values of γ_ν are determined based on Eq. (58) after replacing $\text{atan}\left(\frac{c'(\gamma_\nu)}{c(\gamma_\nu)}\right)$ with the skew angle calculated from Eq. (3).

To summarize, the guided wave field excited by a surface traction loading can be calculated as a convolution of the 3D Green's function $\mathbf{g}^{(3)}(r, \varphi, z)$ with the applied traction. To calculate the value of $\mathbf{g}^{(3)}(r, \varphi, z)$ for a certain angle φ , it is first necessary to find the wave modes and launching directions which have the group/energy propagation directions coincided with the direction of angle φ . Eq. (58) and Eq. (3) serve as the basis to do that. As the second step, Eq. (57) is applied to obtain the 3D function $\mathbf{G}_\nu^{(3)}(\gamma, z)$ for each found wave mode and launching angle using the corresponding 2D plane wave solutions. Eq. (52) is available for the final step of calculating $\mathbf{g}^{(3)}(r, \varphi, z)$.

Based on the asymptotic Green's function given in Eq. (52), guided wave excitations in general multilayer composite plates can be modeled for arbitrary surface source loadings. Convolutions of the Green's function and the loading distribution functions provide us with the excited guided wave displacement fields. If a point source is applied, the convolution yields the Green's function itself multiplied by the magnitude of the point source loading.

Using an out-of-plane point source as an example, the out-of-plane displacement field of the excited guided waves can be written as:

$$u_z(r, \varphi, z) = Ag_z^{(3)}(r, \varphi, z), \quad (59)$$

where A is the magnitude of the applied source loading. Eq. (59) is employed for studying the case of applying the point source to the surface of an 8 layer quasi-isotropic composite plate. The material properties and the lay-up sequence of the plate can be found in Chapter 2. The magnitude of the applied source is 1 Newton. The time-history of the amplitude of the source is described by a 5 cycle Hanning windowed tone-burst signal with a center frequency of 160kHz. Notice that Eq. (59) is for single frequency only, such that Eq. (32) is needed for studying the tone-burst loading. The surface out-of-plane displacement fields of different wave modes are calculated for the time of $32\mu\text{s}$ after the start of the tone-burst loading. The result for the mode 1 is shown in Figure 16. It is demonstrated that the guided wave displacement field is not only of amplitude differences in different directions but also of different propagation speeds.

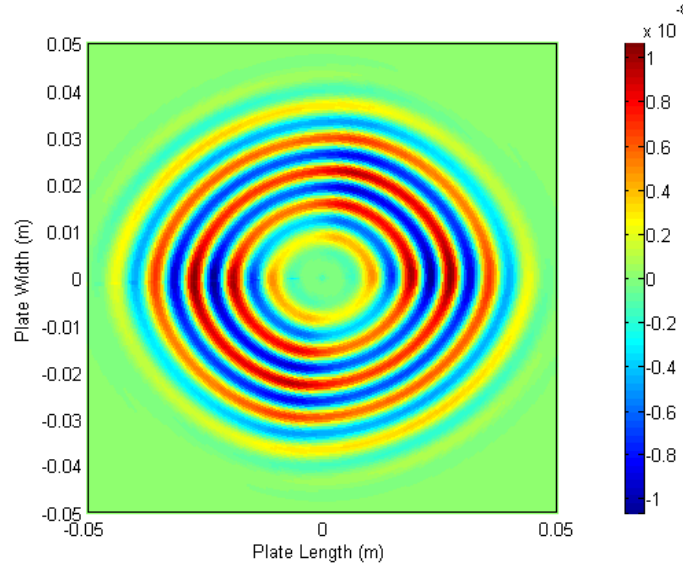


Figure 16: Out-of-plane guided wave displacement field of the mode 1 predicted by the Green's function for the case of a 1 Newton out-of-plane point source applied to the center of the plate surface. The source is driven by a 5 cycle Hanning windowed tone-burst signal with a center frequency of 160kHz. The field shown is for $32\mu\text{s}$ after the start of the tone-burst signal.

A FE model is built using the ABAQUS Explicit software package. Although the out-of-plane point source itself is an axisymmetric loading, due to the material anisotropy, the guided wave excitation is not axisymmetric. As a result, a 3D model instead of the axisymmetric models as used for the isotropic plates is employed. A square plate with 0.1m width is built. The plate is partitioned to 8 layers across the plate thickness. The fiber orientations of the plate are represented by assigning different material orientations to different partitions. The element size used to mesh all of the partitions is 0.5mm and hence results 320,000 elements. Figure 17 presents a corner of the meshed composite plate. The 0 degree fiber direction is at the x-axis

direction. The same out-of-plane point loading as used for the Green's function calculation is applied to the center of the plate surface. The out-of-plane displacement obtained in the FE analysis is shown in Figure 18 for the time of $32\mu\text{s}$ after the start of the tone-burst signal.

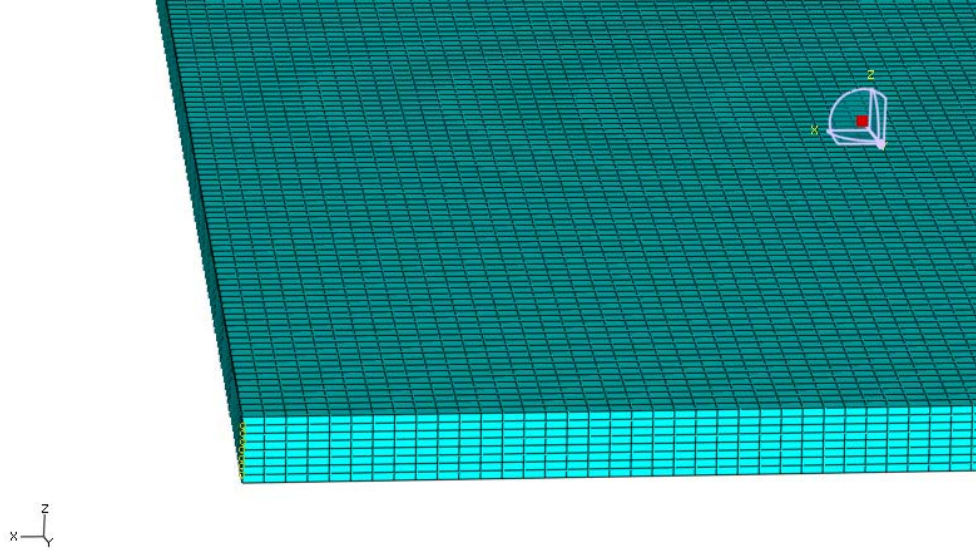


Figure 17: Meshed 8 layer quasi-isotropic composite plate in ABAQUS.

The FE modeling result shown in Figure 18 contains the contributions of all possible guided wave modes. However, it can be directly compared to the displacement field of the mode 1 given in Figure 16 based on the fact that the excitabilities of the other two propagating modes (the modes 2 and 3) are much smaller than the mode 1 excitability. The excitability differences are illustrated in Figure 19 by plotting the out-of-plane excitabilities of all three propagating modes for the center frequency against the wave launching directions. It is demonstrated that the out-of-plane displacements of the modes 2 and 3 are neglectable as compared to mode 1.

By comparing Figure 18 to Figure 16, one can see that there is a good agreement between the FE modeling result and the closed form calculation, especially on the displacement amplitude distributions with respect to the wave propagation directions. Relative high displacement amplitudes are observed for the directions around 0, 180, 72, and 252 degrees in both the FE modeling result and the closed form calculation. The maximum and minimum displacement values in the FE modeling result are 10.87nm and -11nm, respectively. Whereas in the closed form calculation result, the maximum and minimum displacement values are 10.78nm and -10.83nm, respectively. Quantitative comparison between the closed form calculation and the FE model is conducted for the out-of-plane displacement distributions from the center of the plate to the plate edge along the 90° direction. The result is presented in Figure 20. As can be seen, there is a very good agreement between the closed form calculation and the FE model. The minor discrepancies on the appearances of the out-of-plane displacement fields shown in Figure 16 and Figure 18 are introduced by the small differences in the color scales that are used for the

FE modeling result and the image calculated using the closed form solution. Therefore, the validity of the closed form solution derived based on the Green's function is verified by the FE modeling result.

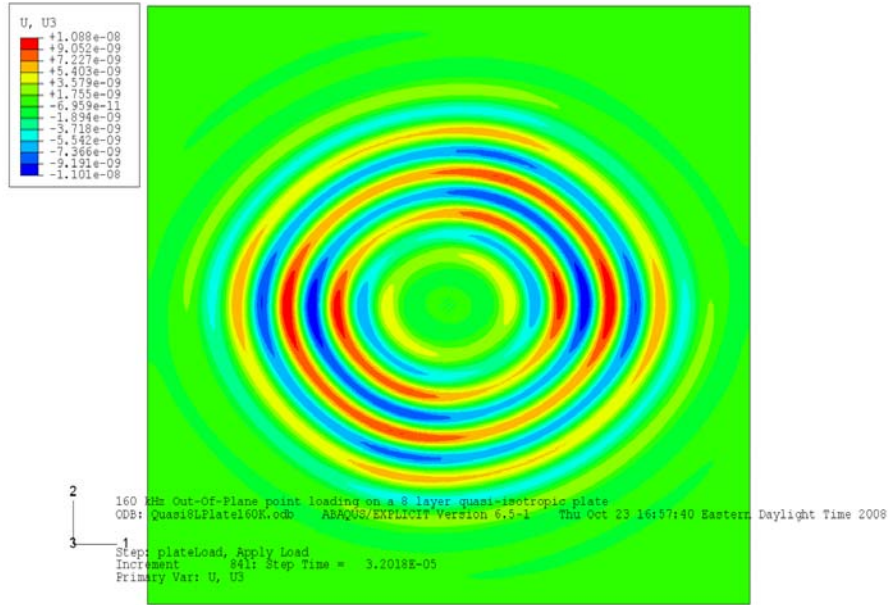
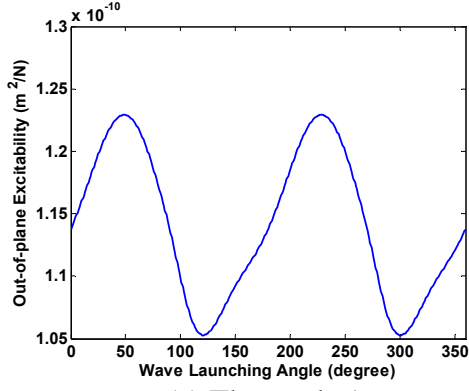
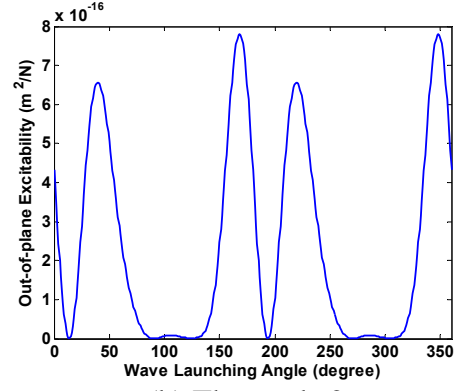


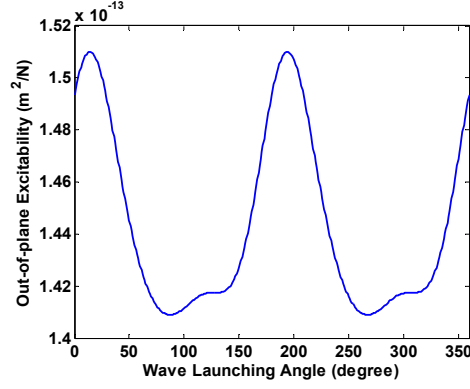
Figure 18: Out-of-plane displacement obtained by FE modeling for the case of applying an out-of-plane point source to the surface of an 8 layer composite plate. The source is driven by a 1 Newton 5 cycle Hanning windowed tone-burst signal with a center frequency of 160kHz. The field shown is for 32 μ s after the start of the tone-burst signal.



(a) The mode 1



(b) The mode 2



(c) The mode 3

Figure 19: Out-of-plane excitabilities of different modes at frequency 160kHz for different wave launching directions. Note that the excitabilities of the modes 2 and 3 are much smaller than the excitability of mode 1.

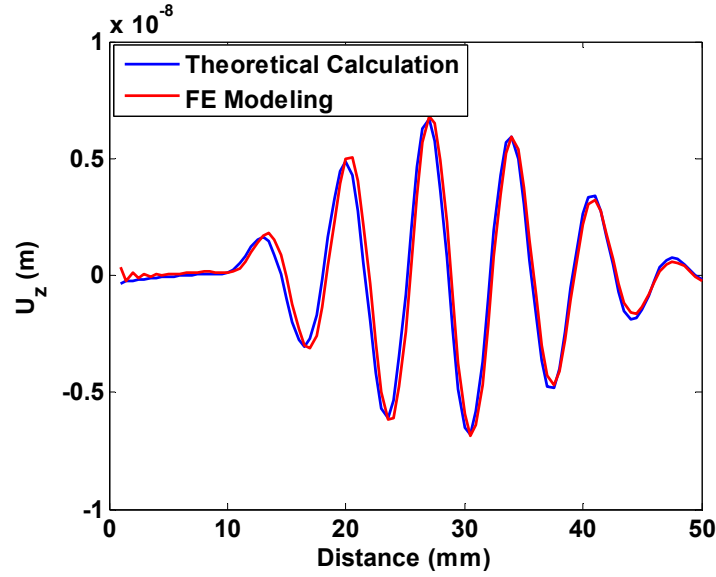


Figure 20: Comparison between the theoretical closed form calculation and the FE modeling result on the out-of-plane displacement distributions from the center of the plate to the plate edge along the 90° direction.

With the Green's function, guided wave excitations by SHM sensors can be predicted if the loadings applied by the sensors are known. It is possible to implement the guided wave excitation studies into the sensor design such that guided wave mode selections for specific inspection requirements can be realized.

Skew angle based composite inspection method

It has been shown that the anisotropy of the composite materials introduces wave skew effects upon which the energy propagation direction does not necessarily coincide with the wave launching direction. Apparently, the wave skew effects need to be taken into consideration when utilizing guided waves for composite inspections. In general, the guided wave skew effects are considered undesirable in guided wave inspections. To avoid them, wave propagation in the material symmetric directions or guided wave modes and frequencies that are almost immune to the material anisotropy (referred as quasi-isotropic mode points in [Yan 2007]) must be selected. In this the method proposed here, by contrast, we propose to take advantage of the guided wave skew effects instead of avoiding them in composite plate inspections. By choosing guided wave modes and frequencies to obtain different skew angles, the guided wave energies are sent into different directions in a composite plate to look for defects while the wave launching direction remains unchanged.

Comb type transducers are an effective means of guided wave mode selection [Quarry 1997], [Li 2001a]. The wavelength of the guided waves to be excited can be controlled by the element spacing of the comb transducers. The distributions of the comb elements can also be designed

to achieve guided wave cancellation [Cawley 2000]. Moreover, it has been demonstrated that by applying time delays to the comb elements, it is possible to conduct guided wave mode tunings in a controlled fashion [Li 2001b]. In this project, time delay comb transducers are employed in the guided wave mode selection method. Since different skew angles can be obtained by applying different time delays and excitation signals to the time delay transducers, the scan of the composite plate can be carried out fully electronically.

Due to material anisotropy, the phase velocity dispersion curves of a composite plate vary with the wave launching direction. Using the 8 layer quasi-isotropic composite plate as an example, the phase velocity dispersion curves of the plate for the wave launching directions 0° and 30° are shown in Figure 21 (a) and (b), respectively. The angle of the wave launching direction is defined by the angle between the direction of the 0 degree fibers and the wave launching direction. As demonstrated, the phase velocity dispersion curves are different from one wave launching direction to the other. It is also shown that different wave modes and frequencies bear different phase velocity variations. As a result, there is a unique slowness curve for each point of the phase velocity dispersion curves. Skew angles, the angles from the wave launching directions to the wave energy propagation directions, can be studied using slowness curves based on the fact that the energy propagation directions are always perpendicular to the slowness curves [Rose 1999]. The slowness curve of mode 3 at frequency 750 kHz is presented in Figure 22. The energy propagation directions for the 0° and 180° wave launching directions are determined and marked with black arrows in the figure as well. The energy propagation directions for the two wave launching directions, as can be seen, are of opposite values. As a result, if there is a defect in the path of the energy propagation when sending the guided wave to the 0° direction, the reflected guided wave with its wave launching direction in the 180° direction, will propagate back to the wave sending position. It is not hard to find out from the slowness curve that such a scenario is always true for any other wave launching directions. Therefore, it is possible to inspect the composite plate in different directions by exciting guided waves with different skew angles, without changing the wave launching direction.

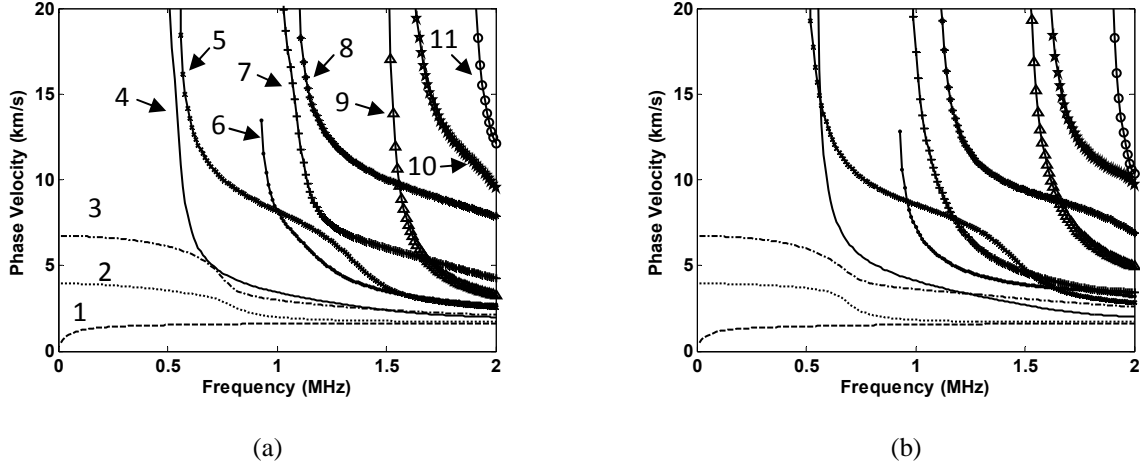


Figure 21: Phase velocity dispersion curves of an 8 layer quasi-isotropic composite plate. The wave launching directions are (a) 0° and (b) 30° .

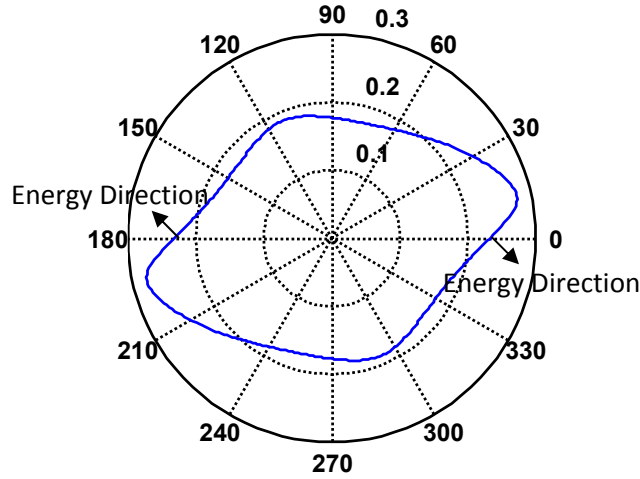


Figure 22: Slowness curve of mode 3 at 750 kHz. The energy propagation directions for the 0° and 180° wave launching directions are marked with black arrows.

To facilitate the idea of using time delay comb transducers for guided wave mode selection, the source influence investigation on the comb type loading is necessary. A schematic drawing of a time delay comb transducer placed on a plate is shown in Figure 23. The width of each element is a and the element spacing is d . The time delay profile applied to the comb transducer is an arithmetic time delay sequence ranging from 0 to $(N - 1)\tau$ in an increment step of τ . The time delays are respectively applied to the N elements from left to right in the $+x$ direction, as illustrated in Figure 23.

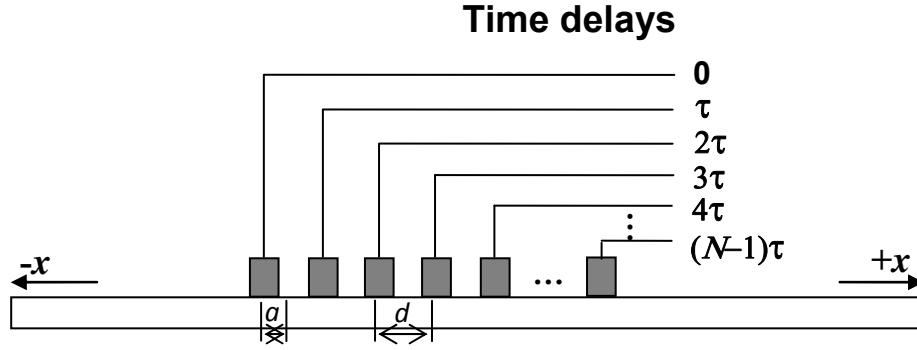


Figure 23: Illustration of a time delay comb transducer placed on a plate.

The normal mode expansion technique based source influence studies suggests that the guided wave excitation can be considered as a combination of the guided wave excitability, which is the intrinsic characteristic of the guided wave mode, and the excitation spectrum determined by the properties of the applied source. For the time delay comb transducer shown in Figure 23, the excitation spectrum for the waves that propagate in the $+x$ direction can be calculated as [Hay 2004]:

$$E(k, \omega) = \left| \frac{\sin(ka/2)}{k/2} \frac{\sin((kd - \omega\tau)N/2)}{\sin((kd - \omega\tau)/2)} \frac{\sin[(\omega - \omega_0)m/2\omega_0]}{(\omega - \omega_0)/2} \right|, \quad (60)$$

where k is the wavenumber, ω is the circular frequency, N denotes the number of elements of the comb transducer, ω_0 denotes the center frequency of the tone-burst signal that is applied to the comb transducer as the excitation signal, and m represents the number of cycles of the tone-burst signal. The excitation spectrum for the waves that propagate in the $-x$ direction can be obtained by simply replacing the time delay τ in equation (1) with $-\tau$:

$$E'(k, \omega) = \left| \frac{\sin(ka/2)}{k/2} \frac{\sin((kd + \omega\tau)N/2)}{\sin((kd + \omega\tau)/2)} \frac{\sin[(\omega - \omega_0)m/2\omega_0]}{(\omega - \omega_0)/2} \right|. \quad (61)$$

Obviously, the excitation spectrums for the waves traveling to the opposite directions are different unless $\tau = 0$. If no time delays are applied, i.e., $\tau = 0$, the excitation spectrums are the same for both wave propagation directions and thus yield a bi-directional wave excitation. This bi-directional wave excitation of the conventional comb transducers is often considered undesired in guided wave inspections. With time delays, however, the excitation spectrums described by Eqs. (60) and (61) are different such that one directional wave excitation is possible.

The excitation spectrums for a 5 element time delay comb transducer are calculated using Eqs. (60) and (61) and given in Figure 24(a) and (b), respectively. The element width of the transducer is 4.22 mm and the element spacing d is 8.44 mm. The value τ used in the

calculations is $0.14\mu\text{s}$ and the tone-burst signal is an 8 cycle 600 kHz tone-burst. As can be seen, a very good excitation of mode 3 is achieved for the $-x$ wave propagation direction. Whereas for the $+x$ direction, the wave excitation is much weaker.

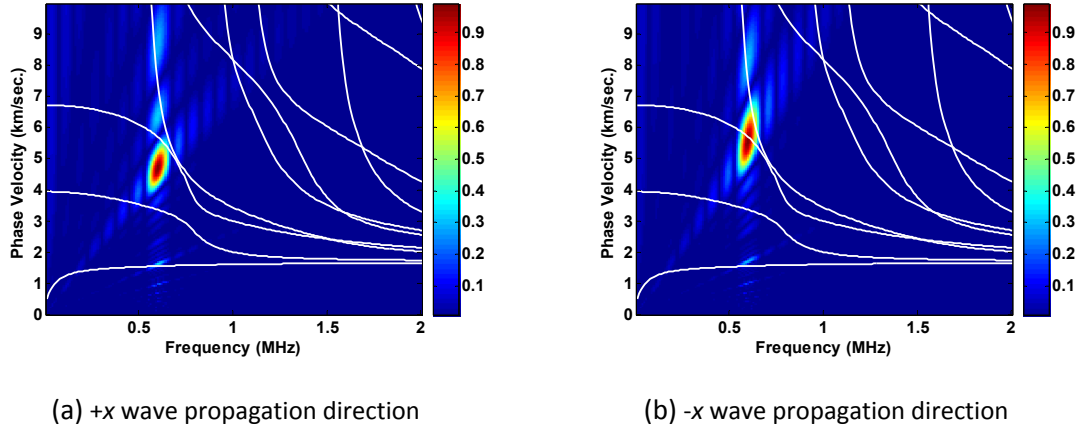


Figure 24: Excitation spectrums for a 5 element time delay comb transducer showing that the guided wave excitation for the $-x$ wave propagation direction is stronger than for the $+x$ wave propagation direction.

The guided wave excitation and propagation in the 8 layer composite plate has been studied using finite element analysis. The commercial finite element software package: Abaqus Explicit is employed to carry out the analysis. Figure 25 presents the finite element modeling (FEM) results for a time delay comb transducer loading on the 8 layer composite plate. The geometry, time delay profile, and the excitation tone-burst signal of the comb transducer used in the FEM analysis are the same as the ones used to generate the excitation spectrums shown in Figure 24.

As can be seen from Figure 25(a), the wave excitation of the guided wave that travels towards left is much stronger than the wave excitation of the right propagating guided wave. This matches the prediction that is made based on the excitation spectrums. Figure 25(b) shows the guided wave field after the waves being reflected back from the plate edges. It is interesting to see that the reflected wave energy follows the incident path and goes back to the transducer position.

The skew angle calculation for the 8 layer composite plate shows that the skew angle of mode 3 at frequency 600 kHz for the 180° wave launching direction is -17.28° . The skew angle that can be observed from the wave propagating towards left does agree with the calculated value.

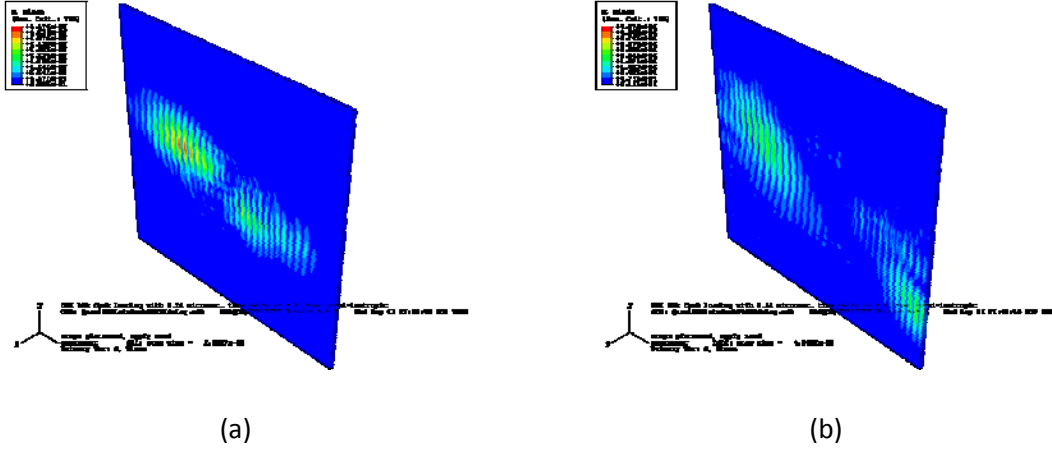
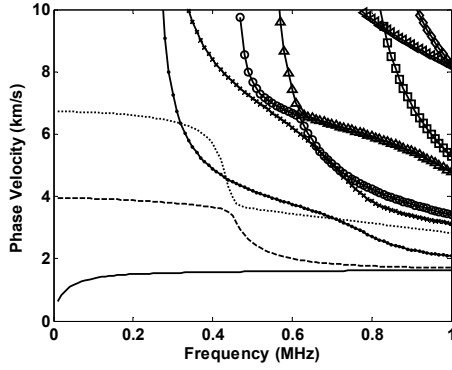


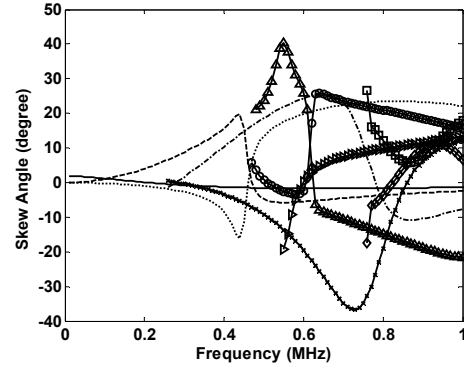
Figure 25: Guided wave fields excited by the time delay comb transducer in the 8 layer composite plate, (a) before hitting the plate edges, (b) after being reflected by the plate edges. Notice that the wave excitation is stronger for the left propagation wave. Besides, the wave energy goes back to the transducer position after being reflected by the plate edges.

The feasibility of sending guided wave energy to different directions for inspection purposes by selecting wave modes and frequencies with different skew angles has also been investigated experimentally. In the experiment, two 5 element comb transducers produced by KrautKramer (now GE Inspection) were used in the experiment under the pitch-catch mode. The element width and spacing of the transducers are 4.22 mm and 8.44 mm, respectively. In the pitch-catch mode, the signals received by the elements of the receiver were delayed and summed in a post-processing fashion. The time delays used for the received signals are the same as the ones applied to the elements of the transmitter. The transmitter is fixed in the experiment to ensure a 0° wave launching direction, while the receiver is moved step by step in the direction that is perpendicular to the wave launching direction. The guided wave signals are recorded for every positions of the receiver. Since the angles offset from the wave launching direction can be calculated for the receiver positions, the skew angle of the guided wave can be determined as the offset angle at which the maximum wave amplitude is received.

A 16 layer quasi-isotropic plate with lay-up sequence $[(0/45/90/-45)_s]_2$ is used in the experiment. The phase velocity dispersion curves of the plate are presented in Figure 26(a). The skew angles are calculated for every point in the phase velocity dispersion curves and then plotted as skew angle dispersion curves in Figure 26(b). The wave launching direction is 0° . Based on Eq. (60), the time delay profile and excitation signal for selecting a certain mode and frequency can be obtained. The excitation signals used in the experiment are 8 cycle tone-burst signals. The time delay profiles described by the τ values and the center frequencies of the tone-burst signals used in the experiment are given in Table 2. The corresponding skew angles predicted from the skew angle dispersion curves and the measured skew angles are given in the table, too.



(a) Phase velocity dispersion curves



(b) Skew angle dispersion curves

Figure 26: Phase velocity dispersion curves and skew angle dispersion curves of the 16 layer composite plate for the 0° wave launching direction.

Table 2 Skew angle measurement results

Frequency (kHz)	Time delay τ (μ s)	Calculated skew angle (degree)	Measured skew angle (degree)
650	2.88	-8.54	-8.34
600	0.6	0.134	2.30
700	0.84	7.47	6.84
750	0.84	8.76	8.34

Comparing the theoretically predicted skew angles with the measured results, one can see that they match quite well. The small discrepancies can be attributed to the inconsistency of the transducer coupling conditions. Since the measured skew angles indicate the optimum positions of the receiver for receiving the guided wave signals, the experiment also proves that the guided wave energy can be sent into different directions by choosing guided wave modes and frequencies with different skew angles. It is hence possible to scan the composite plate in different directions without rotating the transducer. This is in particular of practical value for SHM applications.

Guided wave tomography using annular array transducers

Annular array transducer design and fabrication

The sensors readily available for SHM applications (for example, PWAS sensors) do not provide good control on guided wave mode-frequency selections. Consequently, phased array beam forming may suffer from the influence of unwanted wave modes. Earlier work attempted to

reduce this interference by appropriately selecting the transducer dimensions which can predominantly generate a single mode. The source influence of the transducer results in one mode getting strongly excited while significantly weakening the other modes. However this concept can be used only at low frequencies where there are relatively few modes, otherwise, the transducer selection process becomes very cumbersome. This problem can be overcome by designing transducers that can have mode and frequency control.

Annular array transducers are a class of comb transducers that can generate a desired mode at a desired frequency. They have an array of elements each conveniently spaced at the wavelength that needs to be excited. Fig. 27 shows the excitation line (wavelength) of an annular array sensor design for an aluminum plate. Annular arrays being symmetric have a similar behavior as a PWAS sensor with an additional advantage in the form of desired mode excitation.

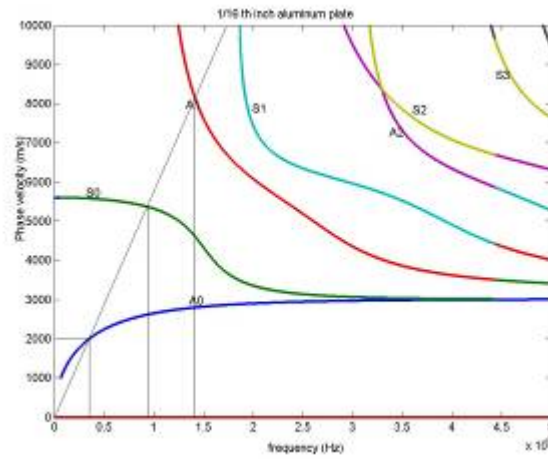


Fig. 27: Dispersion curves of a 1/16th inch aluminum plate exciting A₀ mode at 350 kHz

Finite element model analysis is extensively used to arrive at optimum geometry for the annular arrays to excite a desired wave mode. Models were built in ABAQUS explicit software package. To demonstrate the needs of annular array transducers for better guided wave mode control, two FEM models were constructed to compare the guided wave excitations in a composite plate using a disk transducer and an annular array transducer.

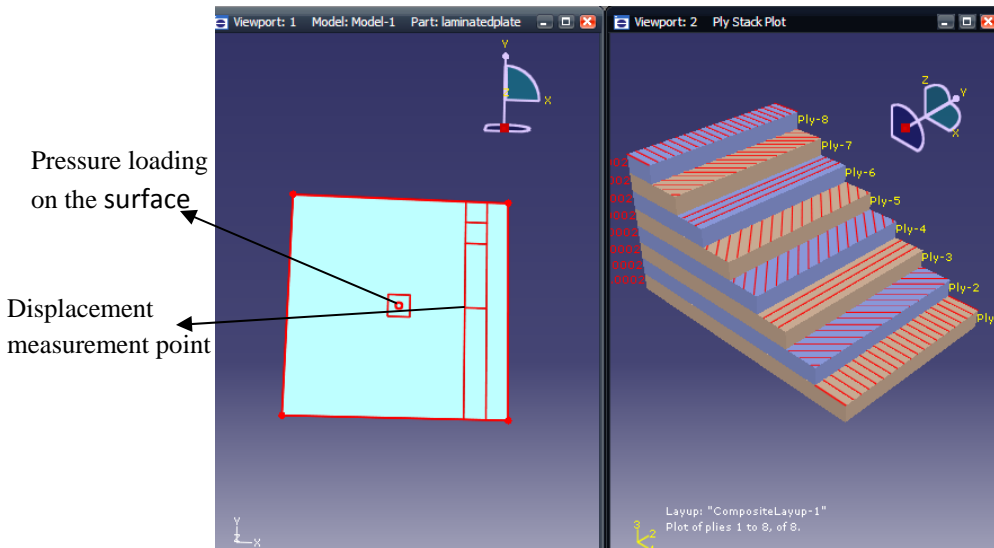


Fig.28: Finite element model of a 200 mm x 200 mm x 1.6 mm 8 layered composite, the ply stack and their orientation can be seen

For the disk transducer model, pressure loading was applied on the composite plate to simulate a piezoelectric disk transducer. Fig.28 shows the 8 layered quasi isotropic plate being modeled. The ply stack and their orientation can be seen in the figure. The resultant U1 displacement at the measurement point on the structure is shown in Fig. 29. It can be noticed that there were multiple modes excited at this frequency when using the disk transducer. In other words, for the given frequency, the mode control of the disk transducer was poor.

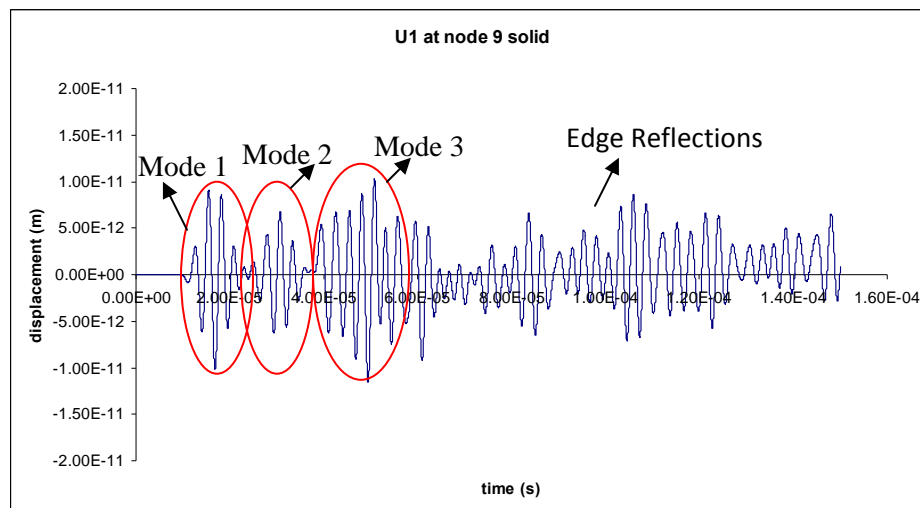


Fig.29: U1 displacement at a point in the structure generated by a disk transducer loading. Multiple wave modes were observed. The mode control of the disk transducer was poor.

An annular array transducer was modeled in a similar fashion. Fig. 30 shows the geometry of the model that was built to estimate the displacement field of an annular array design. A 3D aluminum plate is modeled with an annular array, the annular array is designed to excite A0

mode at 350 kHz with a wavelength of $\lambda=5.7$ mm. The displacement is recorded at a distance 80 mm from the array center. It can be noted in the U3 displacement shown in Fig. 31 that there was only one mode propagating in the structure. The symmetry of the annular array leads to a forward and a backward mode being generated, however they were the same mode. As will be discussed later, this bi-directional wave excitation can be suppressed when applying time delays to the annular array elements.

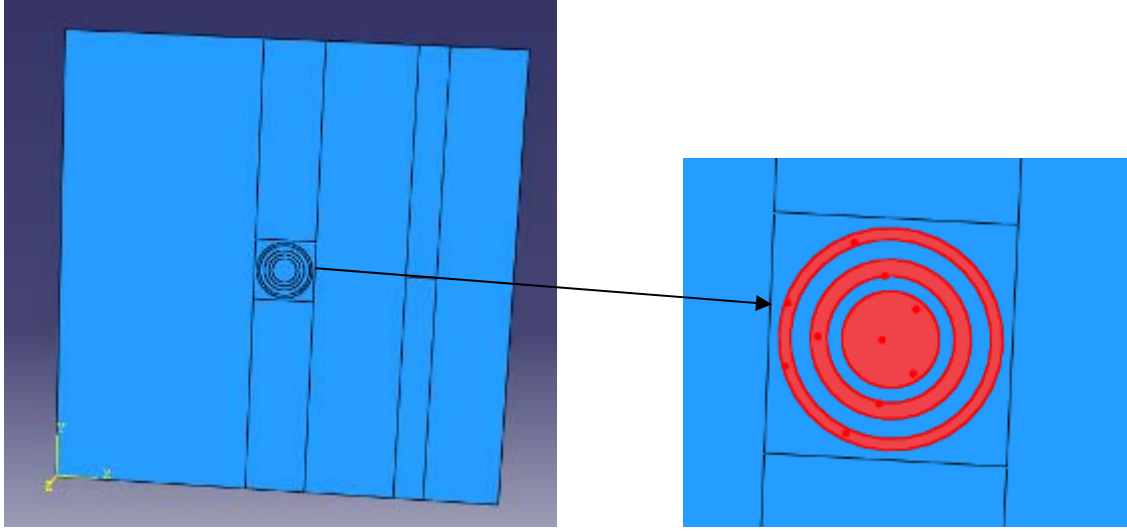


Fig 30: Annular array simulation on plate like structure in ABAQUS

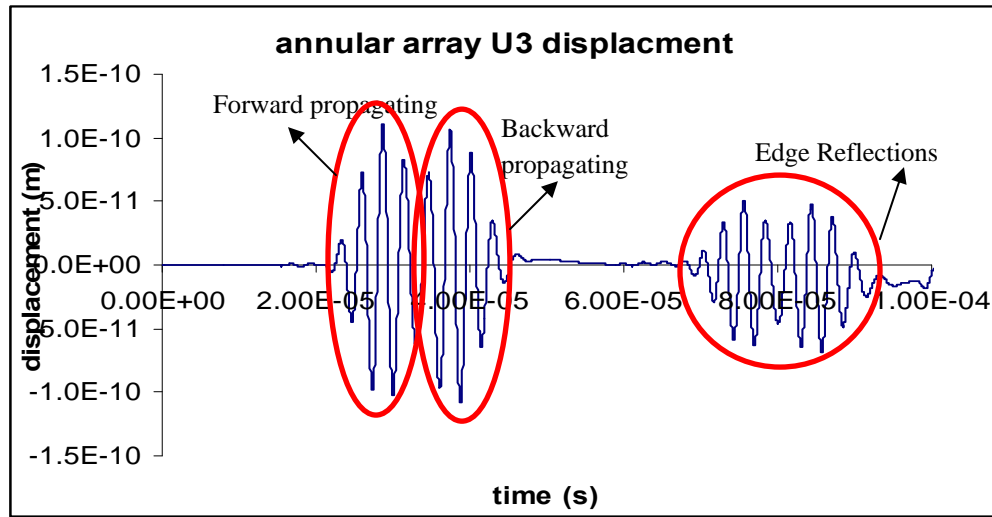


Fig 31: FEM simulation of A0 mode generation at 350 KHz in 1/16th inch aluminum plate with annular arrays

Annular arrays with the desired electrode spacing can be manufactured by patterning the electrodes on top of a piezoelectric substitute as shown in Fig. 32. Generally, the electrode is patterned on top of a printed circuit board (PCB) and glued to the piezoelectric substitute.

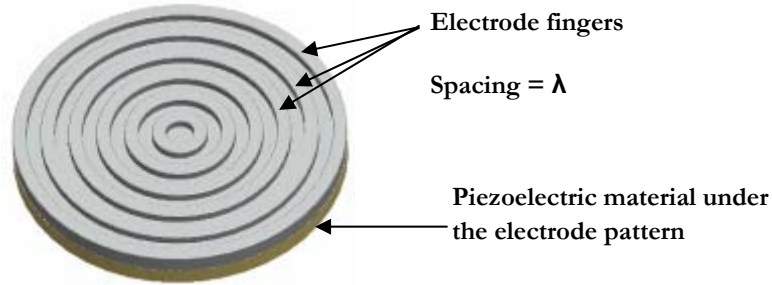


Fig. 32: Configuration of a typical annular array transducer

The commonly used material for the piezoelectric substitute is PVDF. As a polymer, PVDF can conform to any surface and can be readily glued down on any structure. The low electromechanical coupling coefficient of PVDF ($k_t \sim 0.2$) makes it a weak actuator. And its signal to noise ratio is very poor on structures like composites. Hence designing a piezoelectric material that can perform significantly well on composite structures is critical. Table.3 shows the material properties of different piezoelectric materials. It can be noticed that the planar coupling of PVDF is negligible while that of PZT is high. Modified lead titanate, owing to its high electromechanical anisotropy, has neglectable planar coupling. This property of modified lead titanate can be conveniently used in applications where only normal coupling is desired, such as in the case of annular arrays where lateral coupling between the array elements is not desired.

Table.3: Piezoelectric properties of materials tested

	PVDF	PZT 402	Modified Lead Titanate (MPT)
Planar coupling (k_p)	~ 0	0.33	~ 0
thickness coupling (k_{33})	0.19	0.513	0.52
Dielectric Constant (ϵ_r/ϵ_0)	8.4	1250	200

Annular array sensors design is based on the premise that there is no lateral coupling between the array elements. 1-3 piezocomposites are made by dicing a monolithic ceramic like PZT or MPT and filling it with epoxy; the dicing reduces the lateral coupling and increases the thickness coupling. The polymer filled ceramic now has reduced impedance, higher bandwidth. Fig.16 shows the picture of a piezo-composite made by dicing and filling with polymer. A 1mm thick MPT ceramic is taken and diced into 1 mm x 1 mm x 0.9 mm sections which is then filled with a soft epoxy like the epotek 301. The remaining ceramic at the bottom is grinded out. Once grinded, the 1-3 piezo-composite is ready to be coated with electrodes and used as a

transducer. Sputter deposition is normally used to coat the electrode of interest. We coated this composite with 500A chrome and 1500A of gold.

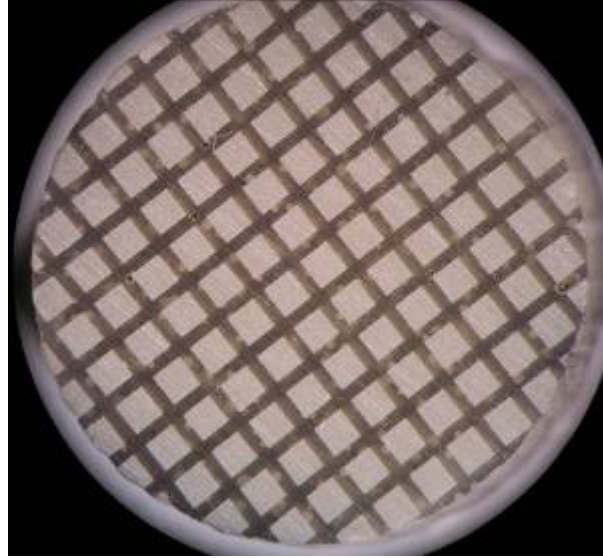


Fig. 33: A 1-3 piezo-composite made from dicing a ceramic and filling with polymer

The detailed manufacturing process of these 1-3 piezo-composites is described in Fig. 33.

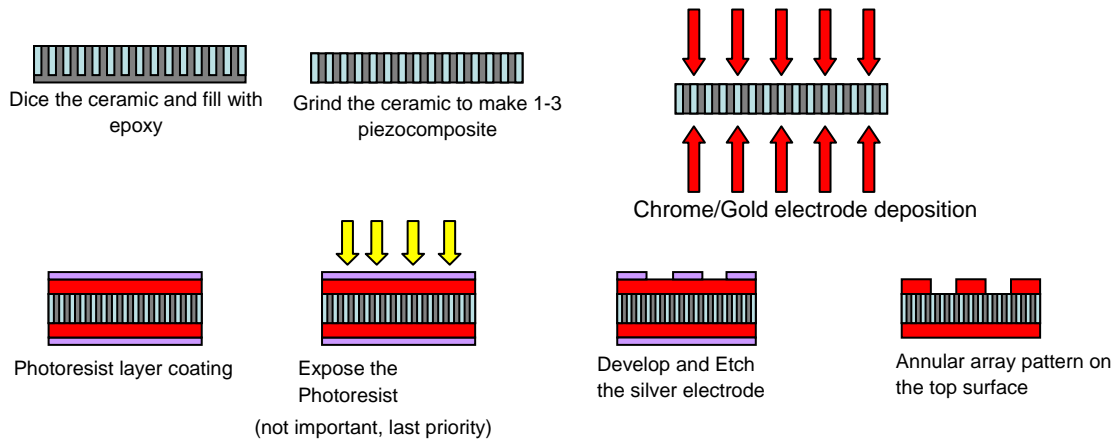


Fig 34: The detailed manufacturing process of the 1-3 piezo-composites

The dimensions of the ceramic pillars in the 1-3 composites are chosen such that the lateral resonant frequency between the pillars is sufficiently away from the frequency range of interest for which the transducer is being designed. The mode coupling theory can be used to compute the different resonant frequencies for a given material and dimensions.

$$f^4 - [f_a^2(1 + \gamma) + f_b^2]f^2 + f_a^2 f_b^2(1 + \gamma - 2\alpha^2) = 0$$

$$f_a = (1/2L)\sqrt{C_{11}/\rho}$$

$$f_b = (1/2H)\sqrt{C_{33}/\rho}$$

$$\alpha = C_{13}/\sqrt{C_{11}C_{33}}$$

$$\gamma = C_{12}/C_{11}$$

Where f_a is the uncoupled lateral resonance, f_b is the uncoupled thickness resonance

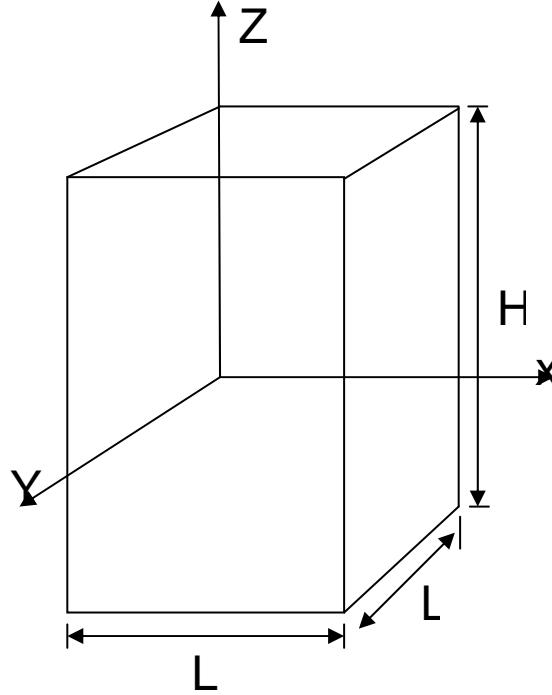


Fig. 35: Pillar shaped element inside 1-3 piezo-composite

Modified lead titanate (MPT) and PZT 402 can be used to fabricate 1-3 piezocomposite. PZT 402 has a high thickness and planar coupling coefficients, hence the resulting piezo-composites should have low aspect ratios ($L/H \sim 0.2$). MPT has a very high degree of electromechanical anisotropy due to which its planar coupling is negligible ($k_p \sim 0$) and a high thickness coupling factor ($k_t = 0.52$). This unique property of MPT allows for high aspect ratio composites ($L/H > 1$) which can be exploited for SHM applications. High aspect ratios result in reduced cost of manufacturing and lead time which is very much desirable in SHM applications owing to the large number of transducers used.

Finite element modeling can be used to model the piezocomposite vibration. Steady state frequency response was used to visualize the vibration patterns of a representative volume element. Fig. 36 shows the representative volume element of an MPT composite and its vibrations at the thickness resonance.

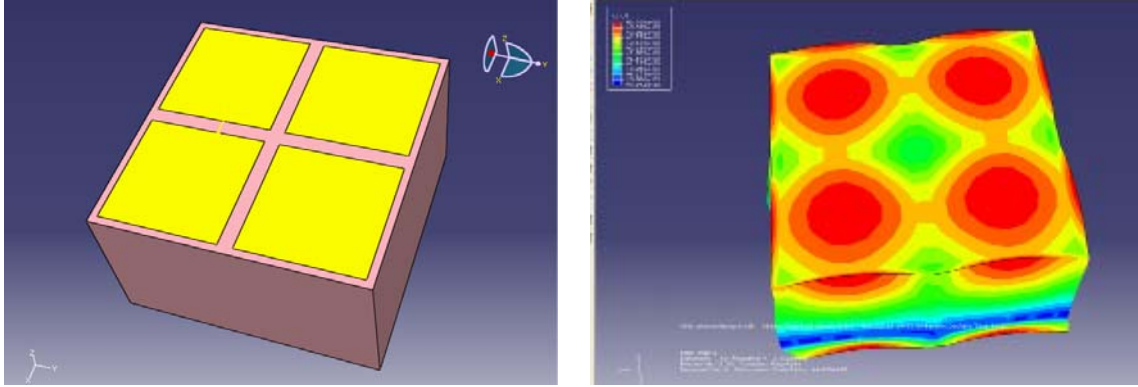


Fig.36: Representative volume element of a 1mm thick 1-3 MPT composite and vibration pattern at thickness resonance

The simulated impedance plots of the 1-3 MPT composite can be seen in Fig. 37.

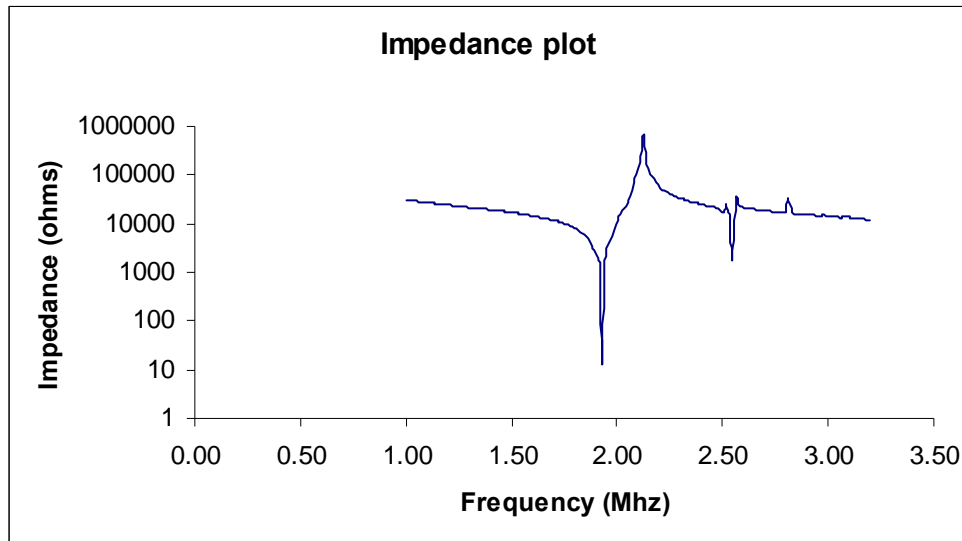


Fig. 37: Impedance plots of a 1mm thick 1-3 MPT composite with aspect ratio 0.7

Flexible 1-3 MPT composites have been designed with high aspect ratios ($L/H = 5$) and a thickness around 500 μm . The epoxy in this composite ($\sim 40\%$) gives it a certain degree of flexibility allowing it to conform to any surface. The detail manufacturing process is shown in Fig. 38. The annular array electrode is designed for a wavelength of $\lambda = 3.1\text{ mm}$, photolithography techniques are used to etch a copper coated mylar film into the desired electrode pattern.

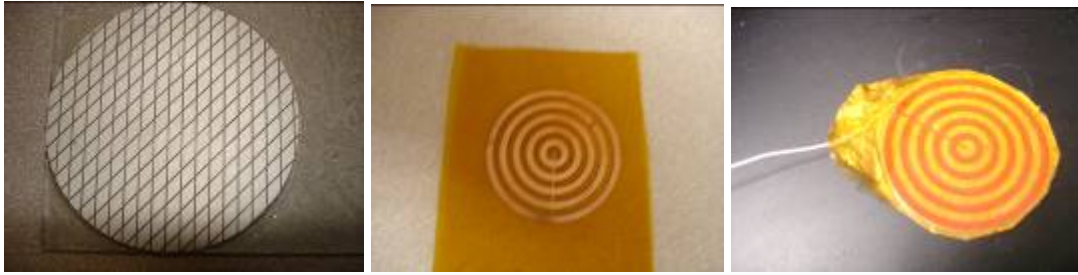
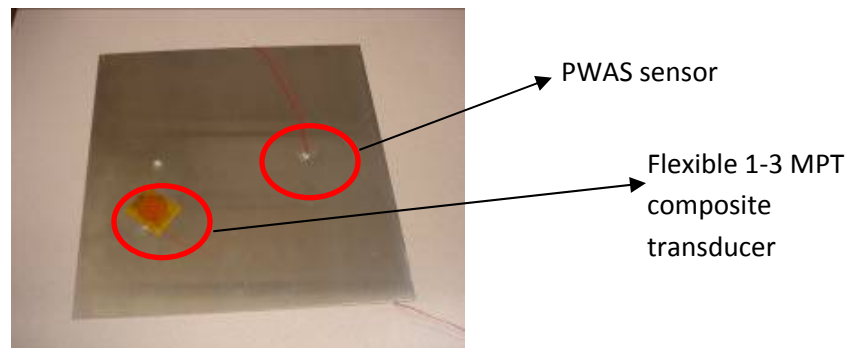
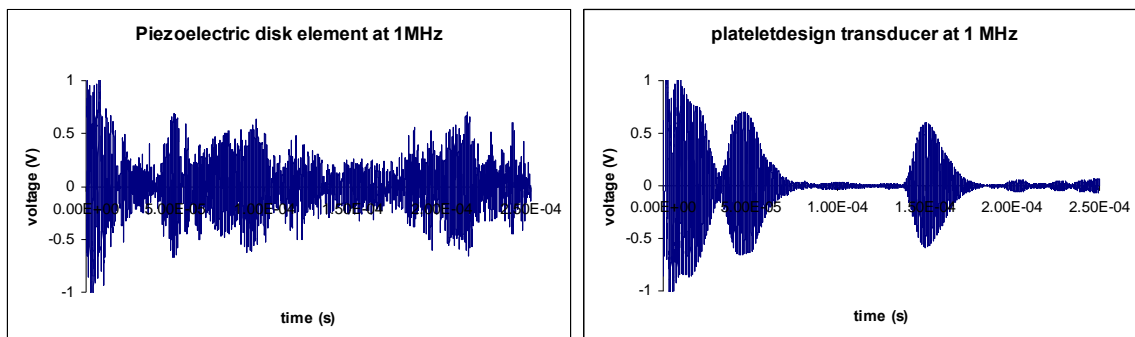


Fig. 38: The ceramic is diced, filled with epoxy and grinded to the desired thickness. The electrodes are bonded to the top and bottom surface of the piezo-composite

An experimental comparison of the pulse-echo signals from a PWAS sensor and the designed annular array transducer at 1 MHz on a 1/16th inch thick aluminum plate is shown in Fig. 39. It can be seen that the signal to noise ratio improvement is significant when using annular array transducers.



(a) Aluminum plate with a PWAS sensor and a annular array attached to the surface



(b) PWAS result

(c) Annular array result ,only A0 mode is excited

Fig. 39: Comparison of signals from PWAS and annular array designed on a 1/16th inch aluminum plate, showing that the annular array transducer produces much higher signal to noise ratio.

Proof-of-concept delamination detection experiment using annular arrays

Delamination detection in composite plates is a very challenging problem. Designing the right transducer can help selecting the right guided wave mode-frequency combination for an optimal sensitivity to delamination defects. A proof-of-concept experiment was performed on adhesively bonded aluminum plates. The delamination was simulated by placing Teflon inserts between the aluminum and the adhesive. An isotropic aluminum-epoxy-aluminum bond is made. The mode selection criterion for the transducer design followed the work discussed in the previous report. The mode with very high concentration of interfacial shear stress was ideal for delamination detection. Hence one such point in the dispersion space at 2 MHz of mode 9 was identified. Its wave structure is shown in Fig. 40. The transducer is a 1-3 piezocomposite made from MPT, it is 15 mm in diameter with Chrome/Gold electrodes. An aspect ratio (L/H) of 1 is used in the 1-3 composite design. The annular array is fabricated using the photolithography techniques described above, the array element dimensions can be seen table.4. The annular array is designed for the wavelength of mode 9 at 2 MHz, $\lambda = 3.1$ mm, hence the separation between successive rings is 3.1 mm.

Table.4: Annular array dimensions

Element Number	Inner Radius (r_i) (mm)	Outer Radius (r_o) (mm)
1	0	1.3
2	2.85	4.40
3	5.95	7.5

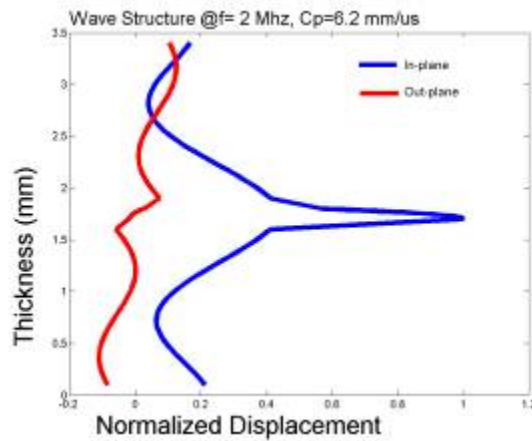


Fig. 40: Wave structure of the mode with high interfacial shear stress used for delamination detection

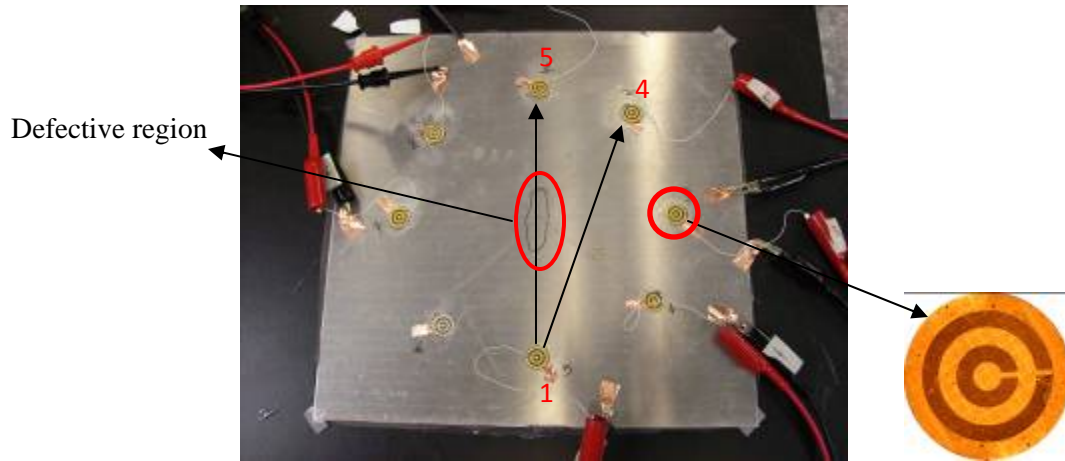


Fig. 41: 1-3 MPT composites designed with appropriate annular array electrodes for delamination detection

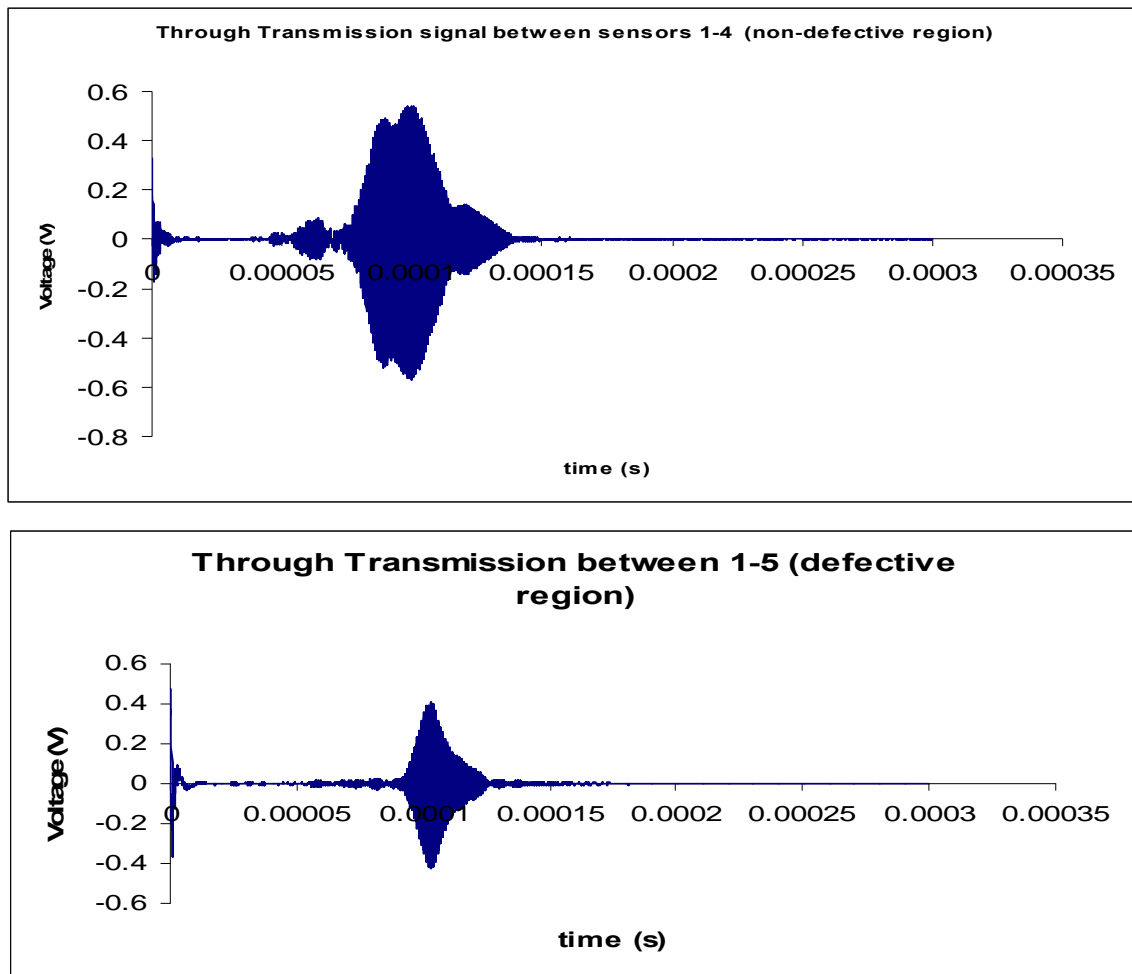


Fig. 42: Delamination detection in bonded plates with the designed annular arrays with and without the defect

The signals obtained using the annular array transducers for a defect free wave path and a path that went through the defect region are shown in Fig. 42. Through the defect free region two modes namely mode 9 and mode 11 get excited due to their proximity in phase and group velocities. Hence two wave packets can be seen in the signal. From Fig. 42, it can also be noticed that there was a considerable change in the guided wave characteristics through the defective region. Mode conversion took place when the wave packet passed through the defective region. Mode 9 which was very sensitive to interfacial defects scattered and converted into mode 11. Such an experiment demonstrated the feasibility of selecting appropriate guided wave mode-frequencies to achieve a good sensitivity to delamination type defects. In the future, we will extend our work to fiber reinforced composite structures.

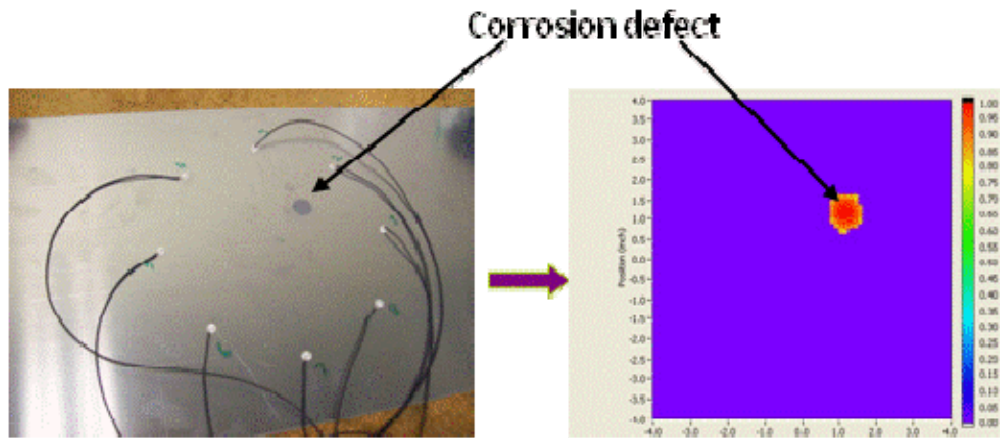
An example application of annular array tomography

Guided wave tomography for structural health monitoring is fast emerging as a reliable tool for the detection and monitoring of hotspots in a structure, for any defects arising from corrosion, delamination, crack growth etc. To date guided wave tomography has been successfully tested on aircraft wings, pipes, pipe elbows, and weld joints. Structures practically deployed are subjected to harsh environments like exposure to rain, changes in temperature and humidity. A reliable tomography system should take into account these environmental factors to avoid false alarms. The lack of mode control with piezoceramic disk sensors makes it very sensitive to traces of water leading to false alarms. In this study we explored the design of annular array sensors to provide mode control for improved structural tomography, in particular, addressing the false alarm potential of water loading.

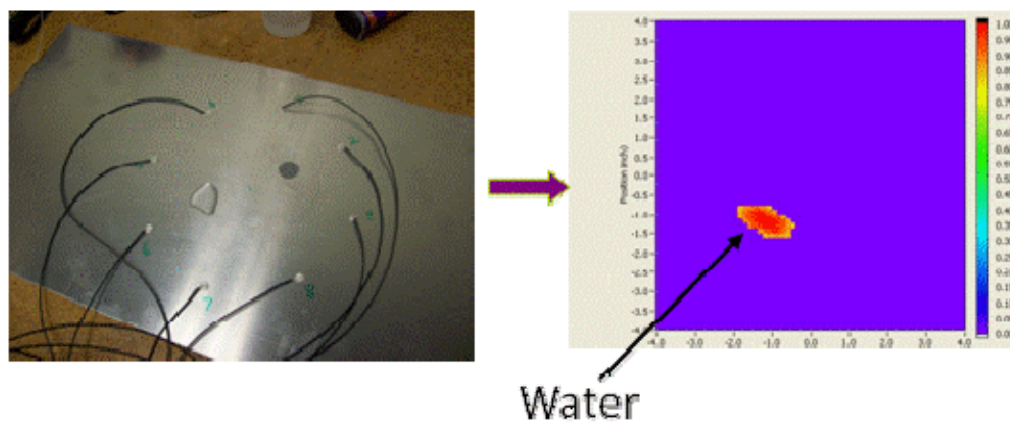
Theoretically there can exist infinite wave modes in a given wave guide for an applied excitation, but few modes tend to dominate the wave propagation in the structure depending on factors like frequency, loading, etc. Piezoelectric disk sensors are typically used for structural health monitoring. Their low cost of manufacturing and the ease with which they can be deployed permanently on a structure makes them ideally suitable for SHM applications. However, piezoelectric disk sensors have limited mode selection capability. With multiple modes being excited, the presence of different modes with different wave structures makes it more difficult to differentiate a real defect from a false alarm. In practically deployed structures, the environmental interaction of the sensors can profoundly influence the measurements. External environmental conditions like water loading or soil loading have an effect on the Lamb wave propagation which can be construed as a defect leading to a false alarm. As an example, the piezoelectric disk sensors with a resonant frequency of 350 kHz are mounted on a thin aluminum plate (1/16 inch thick) which is typically found in aerospace structures. At 350 kHz the sensors can excite A₀ and S₀ modes in the plate. Figure 43 shows the disk sensor readily detecting a corrosion defect on the structure. Adding some water droplets onto the structure to simulate water loading on practical structures leads to a tomogram as shown in Figure 43 as well. The false alarm from the tomogram exposes the vulnerabilities of the current approach to guided wave SHM. The presence of A₀ mode with a predominate out of plane displacement on

the plate surface makes it very sensitive to water loading and results in the false alarm. Hence it is desirable to design sensors that can control the wave modes propagating in the structure.

To overcome the problem of false alarms under water loading conditions, annular array sensors were designed to dominantly excite a point at the dispersion curves with zero out-of-plane displacement in the plate surface. For the 1/16 inch thick aluminum plate, the S1 mode has zero out-of-plane displacements at 2.4 MHz. The wavelength of the S1 mode at 2.4 MHz was used to design the annular array sensors. The designed sensors were tested on the 1/16 inch thick aluminum plate. Eight sensors were bonded permanently on the aluminum plate into a 9 inch diameter circular array. The sensors were used to continuously monitor for defects that arise over time. A baseline data set was collected in this reference configuration. A corrosion damage of 1 inch diameter was simulated using salt water. The corrosion process was accelerated using a battery. Figure 45a shows the corroded area with a thickness loss of 6%. The data were collected with the sensors in a through-transmission mode with one sensor acting as the transmitter while the rest of the sensors served as receivers. The process was repeated between all the sensors. The corroded area was in the line of sight of the sensor pair 2 and 6. Figure 44 shows the received signal between sensors 2 and 6 with and without the presence of water showing the minimal effects of water loading on S1 mode. The tomogram obtained by the annular array sensors at 2.4 MHz demonstrated a remarkable improvement in the ability to distinguish a real corrosion defect from any other water traces on the structure. Figure 45b shows the tomogram of the structure and figure 45c shows the tomogram after false color filtering with only the corrosion defect and no traces of water seen. The example experiment presented here therefore shows the importance of using annular array mode and frequency control for guided wave applications.



(a) A tomography image obtained using PZT sensors showing an indication of the corrosion defect



(b) A tomography image obtained using PZT sensors showing a false alarm caused by water loading

Figure 43. Guided wave tomography images obtained using PZT disk sensors.

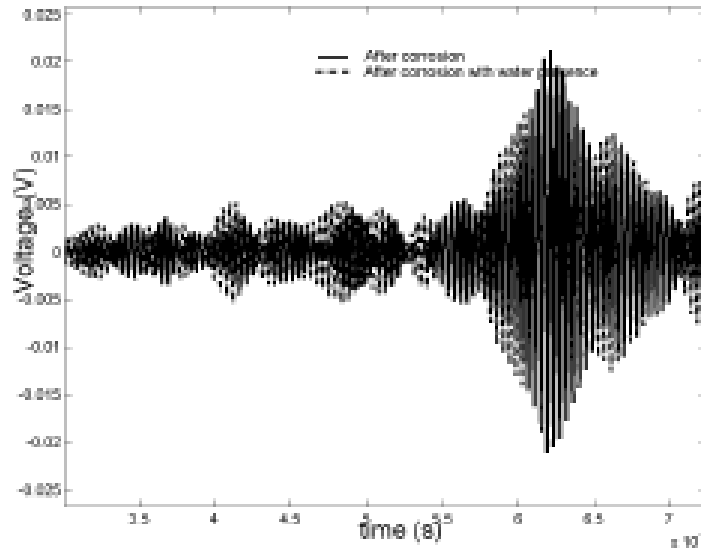


Figure 44. The received signal between sensors 2 and 6 after corrosion with and without the presence of water.

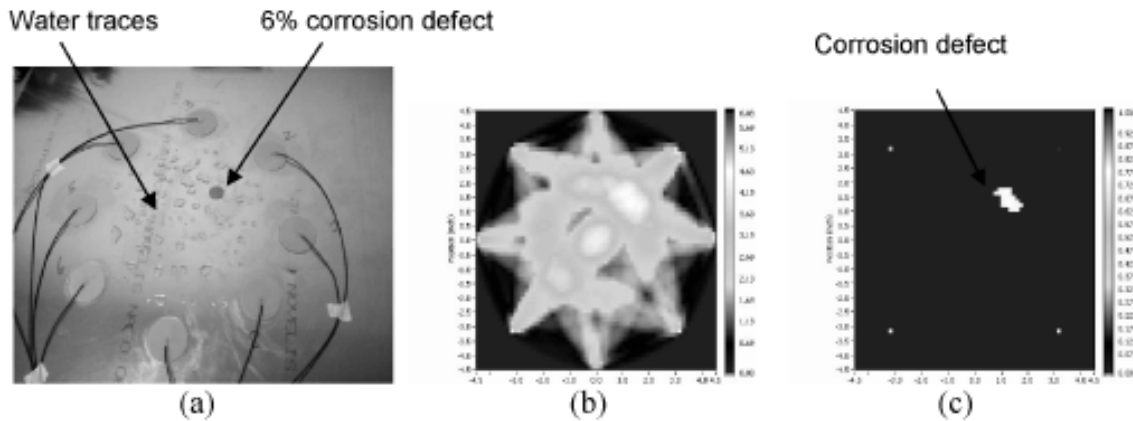


Figure 45. (a) 8 annular array sensors monitoring an aluminum plate with a corrosion defect and traces of water, (b) the resulting tomogram (c) the tomogram obtained showing only the corrosion defect after false color filtering (the water influence was minimal).

Phased Annular Array Transducer Design

Time delay comb transducers are an effective means for guided wave mode selections. The wavelength of the guided waves can be controlled by adjusting the time delay between successive elements. Annular arrays used for mode control are usually large in size due to the multiple rings and large wavelengths. This large transducer size is undesirable in applications like phased array where ideally one would like a point size transducer. Hence, designing an annular array which can control the propagating mode in the structure, at the same time having a small footprint is desired. Phased annular arrays are the candidate to fulfill those requirements.

Phased annular array transducers differ from comb transducers in the fact that the elements are circularly symmetric and can generate omni-directional guided waves. Figure 46 shows three annular array elements mounted on a structure, each element can be excited with unique amplitude and phase. By varying the amplitude and phase it is possible to control the guided wave mode generated in the structure. Due to the infinite possibilities of amplitude and phase combinations the optimum parameters need to be found. Using energy of the excited modes as a parameter it is enough if we can find parameters that can suppress the unwanted modes while maximizing the mode of interest (Glushkov, Glushkova et al. 2006; Glushkov and et al. 2010). Earlier work by (Glushkov and et al. 2010) set up the mathematical problem for loading assumed to be radially symmetric in-plane loading and found out coefficients and time delays for controlled mode generation. However, designing such as an actuator is practically very difficult. In this section, we set up the mathematical problem for uniform pressure type loading on the surface and derive the appropriate parameters for uni-modal generation.

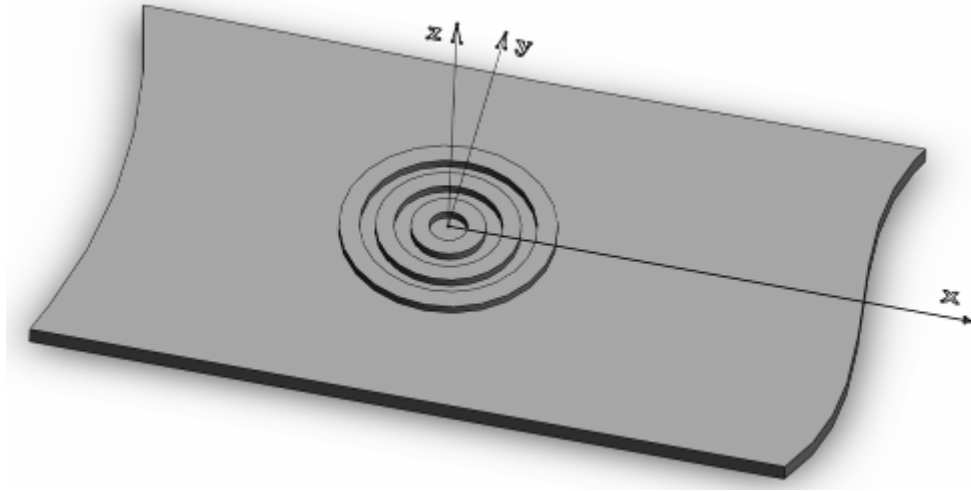


Figure 46: Three annular array elements mounted on a structure

The general expression for far field displacement in the structure due to an arbitrary loading was discussed in the above sections. The displacement due to the annular array actuator with M array elements can be written as

$$u(r, \varphi, q) = \frac{1}{\sqrt{r}} \sum_m \sum_v E_v(\varphi, z) V_m Q_m(k_v, \gamma_v) e^{i\Phi_v(k_v, \gamma_v)} \quad (62)$$

Here γ_v is the wave vector launch angle with contributions in the φ direction and m is the array element number, V_m is the excitation of the element 'm'.

For the m^{th} element annular loading, the loading function can be approximated as a constant normal stress (τ_0) with components only along the z-direction.

$$q_m = (0, 0, q_{zm})^T \quad (63)$$

The spatial Fourier transform of the annular loading is

$$Q_m(k) = (0, 0, Q_{zm})^T \quad (64)$$

$$\begin{aligned} Q_{zm}(k) &= 2\pi\tau_0 \int_0^\infty \hat{q}_{zm}(r) J_0(kr) r dr \\ &= 2\pi\tau_0 \left[\frac{r_{2m} J_1(k_\nu r_{2m})}{k_\nu} - \frac{r_{1m} J_1(k_\nu r_{1m})}{k_\nu} \right] \end{aligned} \quad (65)$$

Selective Radiation

The maximization of a set of a particular mode at a frequency can be set up as a maximization problem in which the desired mode energy has to be maximized among all the modes in the structure. If there N modes at the frequency of interest, let the modes to be maximized be represented by the set H while minimizing the rest of the modes. Using the total energy associated with a mode propagating in the structure we can set up an optimization problem. The driving parameters needed to optimally generate the modes of interest can be expressed as a solution to this maximization problem. Let EN denote the energy associated with a guided wave mode in the structure, the parameters $(\hat{V}(t))$ maximizing $\Delta(\hat{V}(t))$ in Equation (66) should be found.

$$\Delta(\hat{V}(t)) = \frac{\sum_{k \in H} EN_k(\hat{V}(t))}{\sum_{k \in N/H} EN_k(\hat{V}(t))} \quad (66)$$

The total power entering the structure due to the actuator can be written as

$$EN(\omega)_0^h = \frac{1}{T} \int_0^T \frac{dE}{dt} dt = -\frac{\omega}{2} \text{Im} \int_S (\hat{u}, \hat{\tau}_n) dS \quad (67)$$

$$EN_0^h = \pi\omega \text{Im} \int_0^\infty (\hat{u}(r, 0), \sum_{m=1}^M \hat{V}_m \hat{q}_m(r)) r dr \quad (68)$$

The integral can be rewritten in terms of its Fourier transform using Parseval's identity as in Equation (69) which can be written as Equation (70)

$$EN_0^h = \pi\omega \text{Im} \int_0^\infty (G(k, 0) \sum_{m=1}^M V_m Q(k), \sum_{m=1}^M V_m Q(k)) k dk \quad (69)$$

$$EN_v^h = \sum_{i=1}^M \sum_{j=1}^M a_{ij}^v V_i V_j^* = (A\hat{V}, \hat{V}) \quad (70)$$

$$a_{ij}^v = \frac{\omega}{4} \text{Re } s(G(k,0)) \Big|_{k=k_v} Q_j(k_v) Q_i(k_v) k_v \quad (71)$$

The total energy radiation associated with the mode during the whole time period is

$$E_v = \frac{2}{\pi} \int_0^\infty E^h(\omega) d\omega = \frac{2}{\pi} \sum_{i=1}^M \sum_{j=1}^M \int_0^\infty a_{ij}^v(\omega) V_i(\omega) V_j^*(\omega) d\omega \quad (72)$$

For guided wave mode generation usually tone-burst type excitation is used in which majority of the energy is concentrated at a single frequency, hence the energy associated with a mode can be approximated as

$$E_v(\omega_c) = \frac{2}{\pi} \sum_{i=1}^M \sum_{j=1}^M a_{ij}^k(\omega_c) V_i(\omega_c) V_j^*(\omega_c) \quad (73)$$

The driving parameters

$$\hat{V}_m(\omega) = \int_{t_m}^\infty A_m f(t-t_m) e^{i\omega t} dt = A_m e^{i\omega t_m} \hat{f}_n(\omega) = e_m(\omega) \hat{f}_n(\omega) \quad (74)$$

For a tone burst excitation majority of the energy is concentrated at the center frequency and hence the energy parameter can be approximated as

$$E_k(\omega) = \frac{2}{\pi} \int_0^\infty (Ae, e) \left| \hat{f}_n(\omega) \right|^2 d\omega \quad (75)$$

Hence the equation can be rewritten as

$$\Delta(e) = \frac{(Ae, e)}{(Be, e)} \text{ where } A = \sum_{k \in H} A^k(\omega_c), B = \sum_{k \in N/H} A^k(\omega_c) \quad (76)$$

The maximum of $\Delta(e)$ occurs when

$$\frac{\partial \Delta}{\partial e} = 0, \text{ where } e = (e_1, e_2, \dots, e_M) \quad (77)$$

Hence the maximum occurs for the driving parameters satisfying

$$(A - \Delta B)e = 0 \quad (78)$$

If $\det(B) \neq 0$ then the eigen vector corresponding to the maximum eigen value gives the optimum driving parameters. If $\det(B) = 0$ then the eigen vector corresponding to the eigen values, $\lambda_0 = 0$ provide full damping of the undesired radiation. In this case the maximizing parameters for (Ae_s, e_s) is to be searched as a linear combination of the eigen vectors damping the undesired radiation which can be expressed as in Equation (79)

$$e_s = \sum_{k=1}^{k_0} c_k e_k, \text{ with } \|e_s\| = 1 \quad (79)$$

The new maximization problem reduces to the search for the coefficients vector $c = (c_1, c_2, \dots, c_n)$. This modified problem can be written as in the similar form as Equation (80).

$$A^0 = (a_{ij}^0), a_{ij}^0 = (Ae_j, e_i) \text{ for } i, j = 1, 2, \dots, k_0 \quad (80)$$

$$B^0 = (b_{ij}^0), b_{ij}^0 = (e_j, e_i)$$

The matrix B^0 being a grammian of the linearly independent eigen vectors, the maximization problem reduces to

$$(A^0 - \Delta)e_s = 0 \quad (81)$$

The eigen vector corresponding to the maximum eigen value e_s is taken and the corresponding coefficient vector is calculated to obtain the optimum driving parameters. The amplitude and time delay necessary for each element can be calculated as

$$A_m = |e_m| \quad (82)$$

$$t_m = \arg(e_m / \omega_c), \text{ if } 0 \leq \arg(e_m) \leq \pi$$

$$t_m = \pi + \arg(e_m / \omega_c), \text{ if } -\pi \leq \arg(e_m) \leq 0 \quad (83)$$

Numerical Simulations

Using the analytical expressions for far field radiation of guided wave modes, it is possible to simulate the guided wave mode propagation in the structure. A four element annular array is simulated on an aluminum structure of thickness 3.2 mm. The array dimensions are given in Table 5. The array is actuated with a tone burst at a frequency of 500 KHz.

Table 5. Numerically calculated amplitude and time delays at 500 KHz for unimodal guided wave generation in an aluminum plate

Element	A0 Mode		S0 mode	
	Amplitude	Time delay (us)	Amplitude	Time delay (us)
1	0.6341	1	0.2238	1
2	0.7292	0	0.3332	0
3	0.1972	1	0.1005	1
4	0.1651	0	0.9104	0

The waveform in the structure with these excitation coefficients can be calculated analytically. With no amplitude and time delay on the array elements the out-plane displacement at a distance 600 mm from the center can be seen in Figure 47 showing both the A0 and S0 modes. With amplitude and time delay control at each element, Figure 48 shows the waveforms with one showing selective A0 mode excitation and the other showing selective S0 mode excitation.

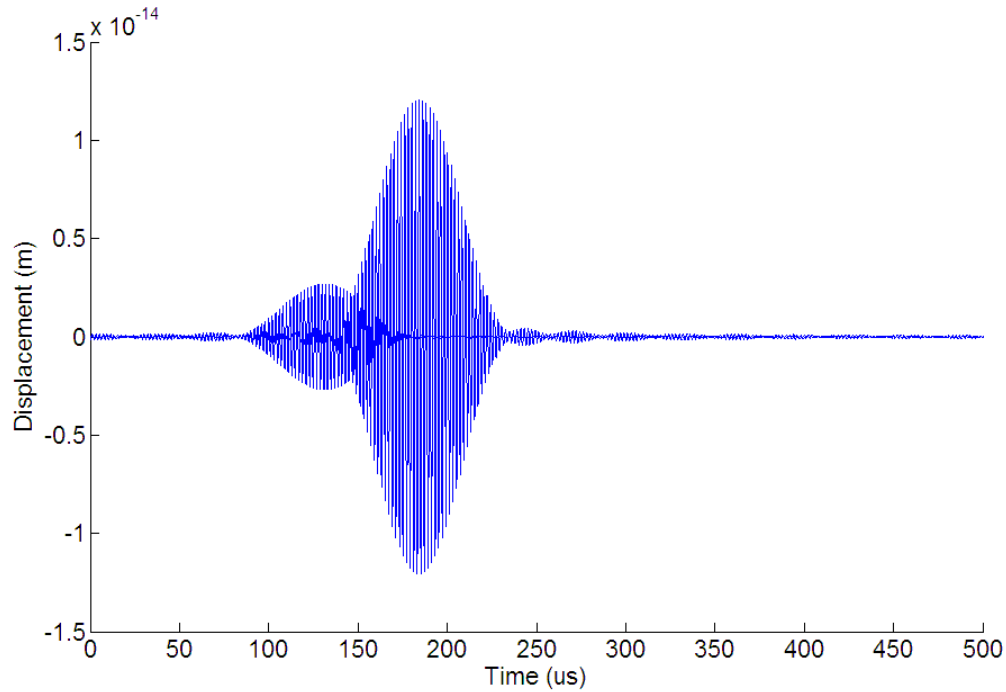


Figure 47: Out-plane displacement in an aluminum plate at a distance of 600 mm due to the annular array with no amplitude and mode control

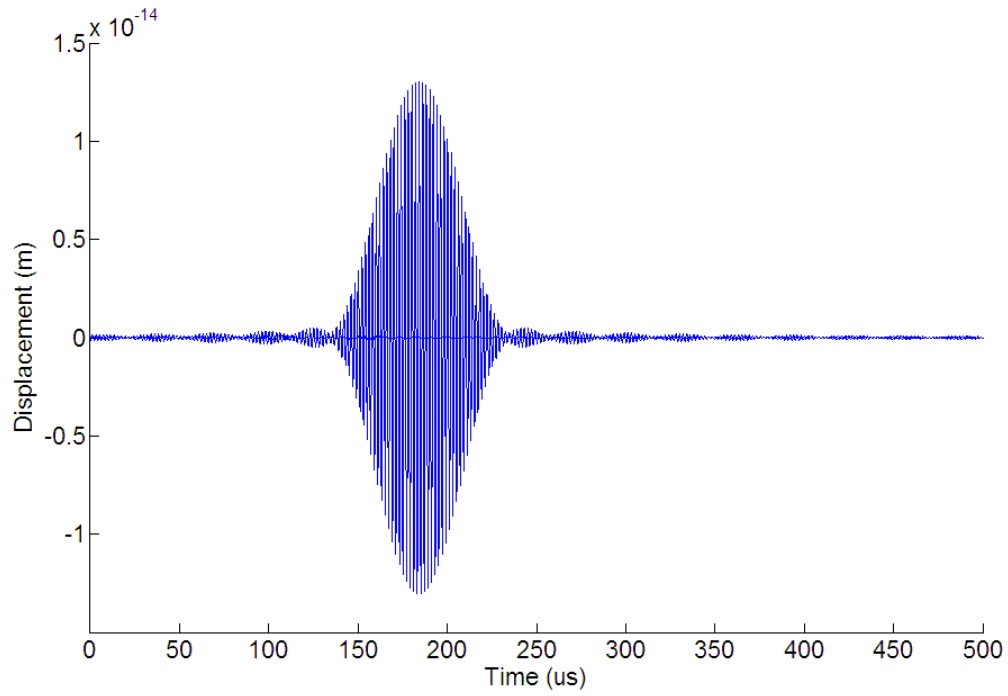


Figure **48**: A 50 cycle tone burst excitation with amplitude and time delay parameters to maximize the A0 mode and suppress S0 mode

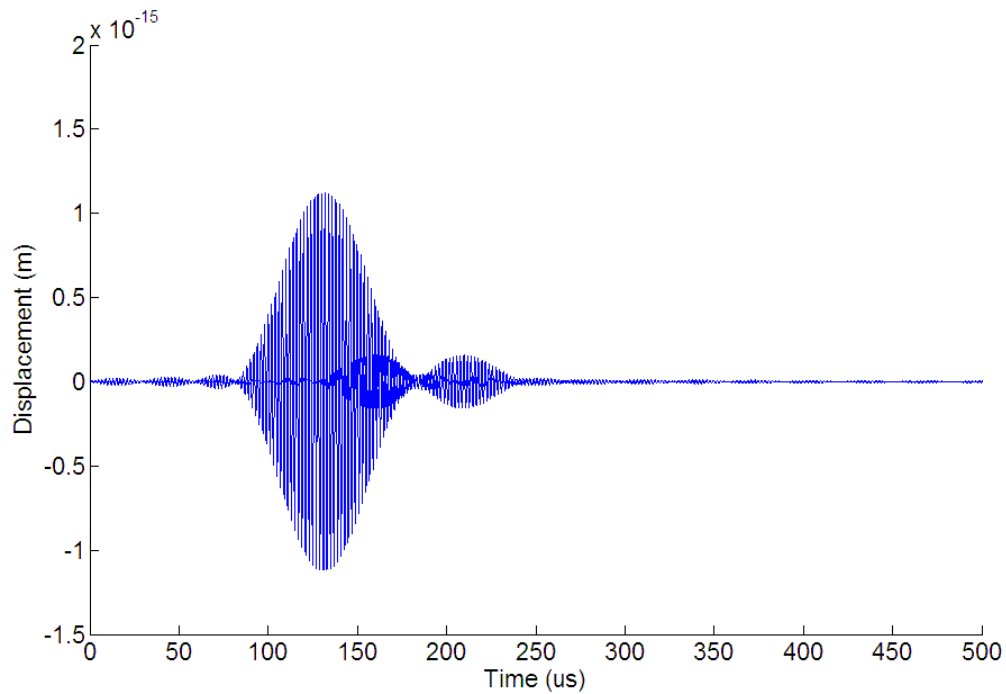


Figure **49**: A 50 cycle tone burst excitation with amplitude and time delay parameters to maximize S0 mode and suppress A0 mode

Piezocomposite based Phased annular array transducers

A typical piezoelectric transducer has a piezocomposite or piezoceramic material, with a matching front layer and a lossy backing. These designs are commonly used in the manufacture of transducers for medical technology and NDT. Figure 50 shows the schematic of a transducer. The piezocomposite disk is sandwiched between a lossy backing and a matching front layer, two electrodes at the top and the bottom are used to apply a sinusoidal voltage.

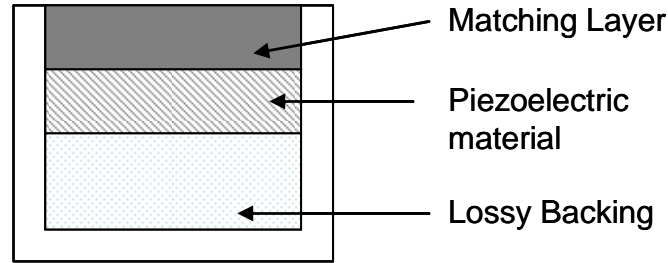


Figure 50: Schematic of a transducer

1-3 Piezocomposite transducers have significantly lower impedance than ceramic material, the typical acoustic impedance of a 1-3 piezocomposite is around 15 MRayl. The impedance of water is around 1.5 MRayl and necessitates a matching layer for efficient transducer operation. For materials like aluminum and fiber reinforced composite with acoustic impedances of around 17 MRayl and 10 MRayl respectively, the matching layer can be optional. The bandwidth of the transducer can be improved by using a lossy backing with approximately the same impedance as the active material. Tungsten filled epoxy is the commonly used backing material which takes advantage of the lossy wave propagation in epoxy and the high acoustic impedance of tungsten, by mixing them in an appropriate ratio backing material of high impedance can be made (Grewe, Gururaja et al. 1990). The desired acoustic impedance of the front matching layer can be found from Equation (84) [Desilets, Fraser et al. 1978].

$$Z_{front} = \sqrt{Z_c Z_L} \quad (84)$$

Where, Z_c –Acoustic impedance of piezomaterial , Z_L - Acoustic impedance of the Load

For array transducers similar fabrication methodology can be employed, for annular array transducer fabrication we can take advantage of the low lateral coupling in the 1-3 piezocomposites and just pattern the electrodes into a desired shape. The desired electrodes can be patterned using lithography techniques. Figure 51 shows a 1-3 PZT-5A fiber composite with center frequency at 500 KHz and the electrodes etched to have four elements numbered from inside to outside. Table 6 shows the dimensions of the array transducer.



Figure 51: A 500 KHz 1-3 Piezofiber composite annular array

Table 6: The dimensions of annular array elements in the transducer

Element Number	Inner Radius (r_i) (mm)	Outer radius (r_o) (mm)
1	0.5	1.5
2	2.5	3.5
3	4.5	5.5
4	6.5	7.5

The transducer is fabricated keeping the width of the annular ring constant which results in increasing area for the outer rings. An apodization factor can be used to keep the impedance uniform across the array elements. The cross talk between the array elements in the transducer can be experimentally determined using phase-gain analysis. An impedance analyzer is used to measure the cross-talk between the adjacent elements in the piezofiber composite. From Figure 52 and 53 it can be seen that at the thickness resonant frequency of the composites the maximum cross-talk occurs which is sufficiently low at -25 dB between elements 1 and 2, -30 dB between elements 1 and 3.

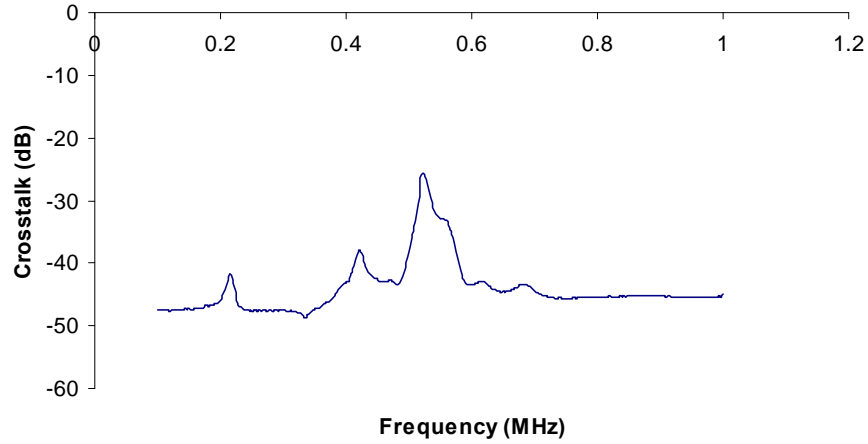


Figure 52: Crosstalk measurement between array elements 1 and 2

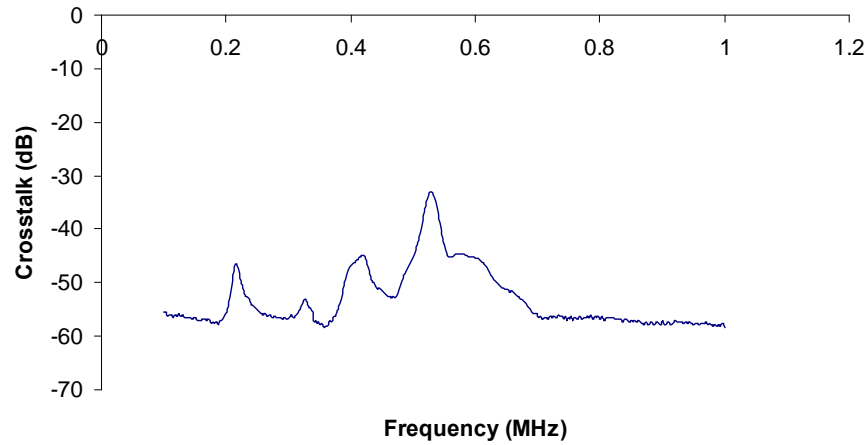


Figure 53: Crosstalk measurement between array elements 1 and 3

The impedance of each array element can be measured using an impedance analyzer, the impedance plots for all the four annular rings can be seen in Figure 54 (a)-(d). It can be noticed that the resonant frequency which is the thickness resonance is uniform across four elements. However, some spurious lateral resonances for fourth ring do fall close to the thickness resonance.

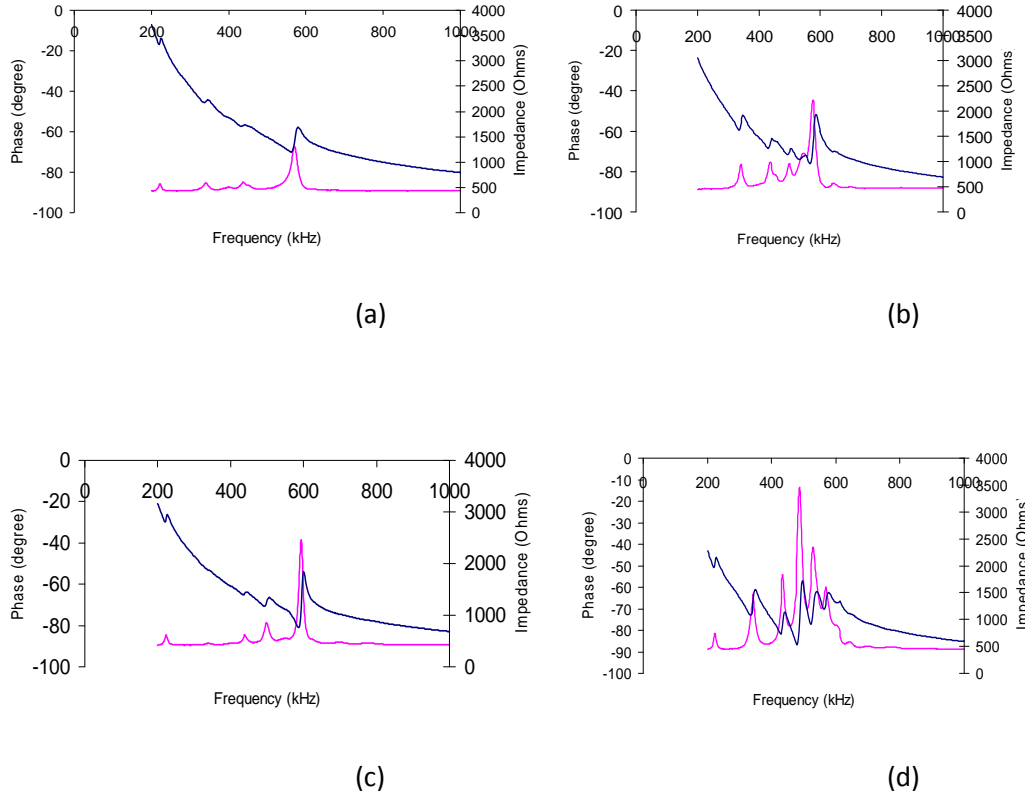


Figure 54: Impedance plots of the different annular rings in the array transducer

The array transducer is made of PZT-5A fibers of thickness 250 μm , the fibers are placed randomly in an epoxy matrix with a fiber volume fraction of 65%. The transducer material is manufactured by Smart Materials Corporation. The transducer is electroded with 1 μm thick copper and a thin tin layer used as a passivation layer to prevent corrosion. For array transducers it is imperative to reduce the cross-talk between elements, hence when using a matching layer it is optimal to dice the matching layer into the array pattern. However, complex array shapes may not always permit this and hence the use of a monolithic matching layer needs to be used which does reduce the isolation between the elements.

Experimental observations of a 1-3 piezocomposite phased annular transducer

A Phased annular array transducer is fabricated with the dimensions as in Table 5. The array element width is 1mm with spacing between successive elements of 1mm. The piezocomposite element is housing in a brass casing, a tungsten filled epoxy backing is used to damp the active element. The acoustic impedance of the piezocomposite (17 Mrayl) is very close to the aluminum structure (17 Mrayl) on which it is being mounted, hence no matching layer is used. The experimental arrangement can be seen in Figure 55. The transducer is permanently bonded on a 3.2 mm thick aluminum plate. It is operated at a frequency of 500 kHz, at which point there are two modes that can exist in the structure namely A0 and S0 modes. To identify the guided

wave modes excited in the structure, the transducer is operated as a sender with desired voltage and time delays while a normal beam transducer is used to receive the modes propagating in the structure. Tuning the amplitude and phase of the transducer elements to generate A0 mode we can see that the S0 mode gets suppressed in the structure as in Figure 56. Similarly, for the S0 mode parameters the A0 mode gets suppressed which can be seen in Figure 57. The small dimensions of the plate means there are several reflections from the edges which can be seen along with the main arrival in the time domain signals.

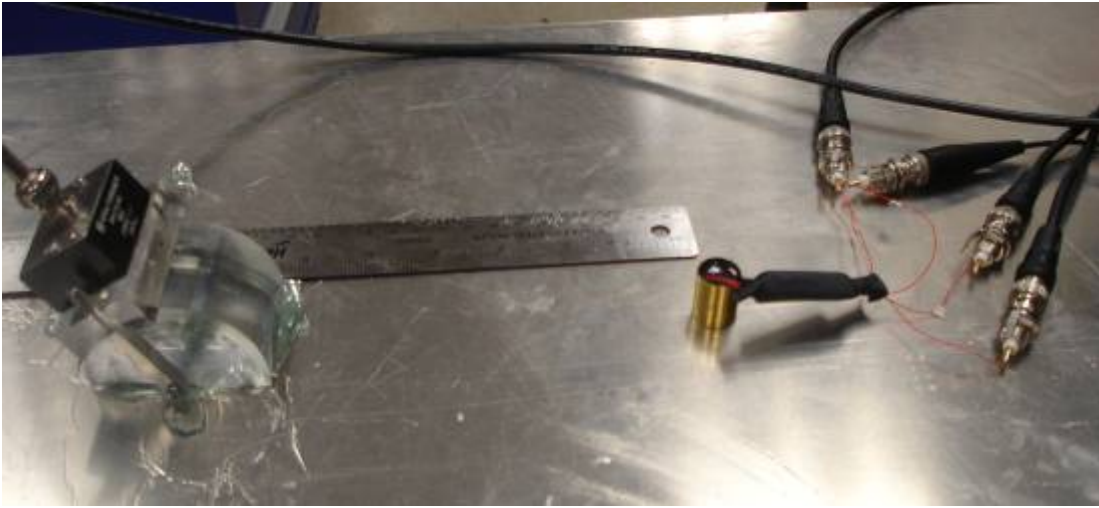


Figure 55: 1-3 Piezocomposite Phased annular transducer and an angle beam receiver mounted on a 3.2 mm thick aluminum plate

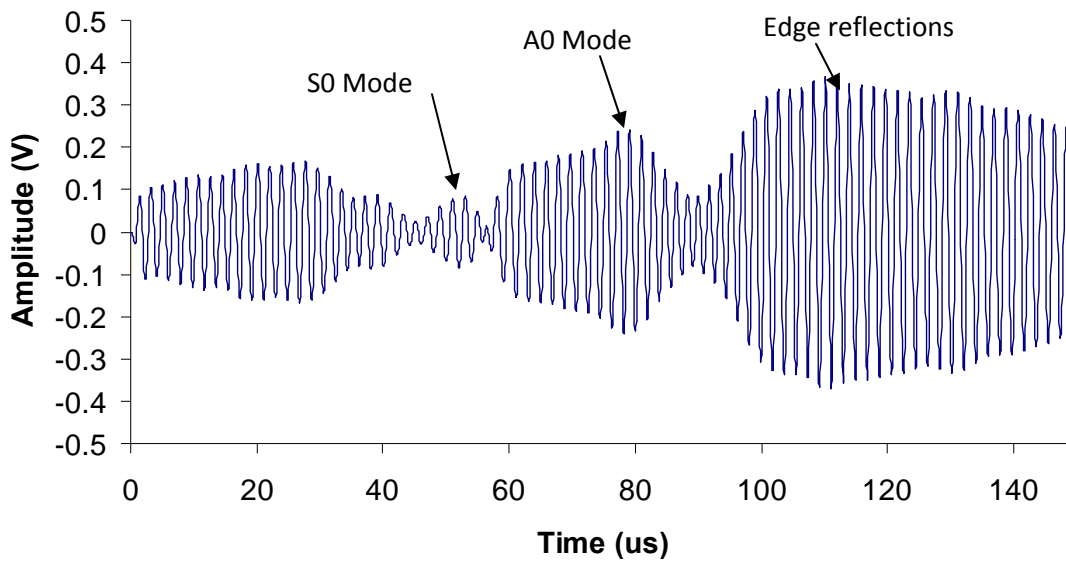


Figure 56: A0 mode generation in the plate with amplitude and time delay to maximize A0 mode and suppress S0 mode

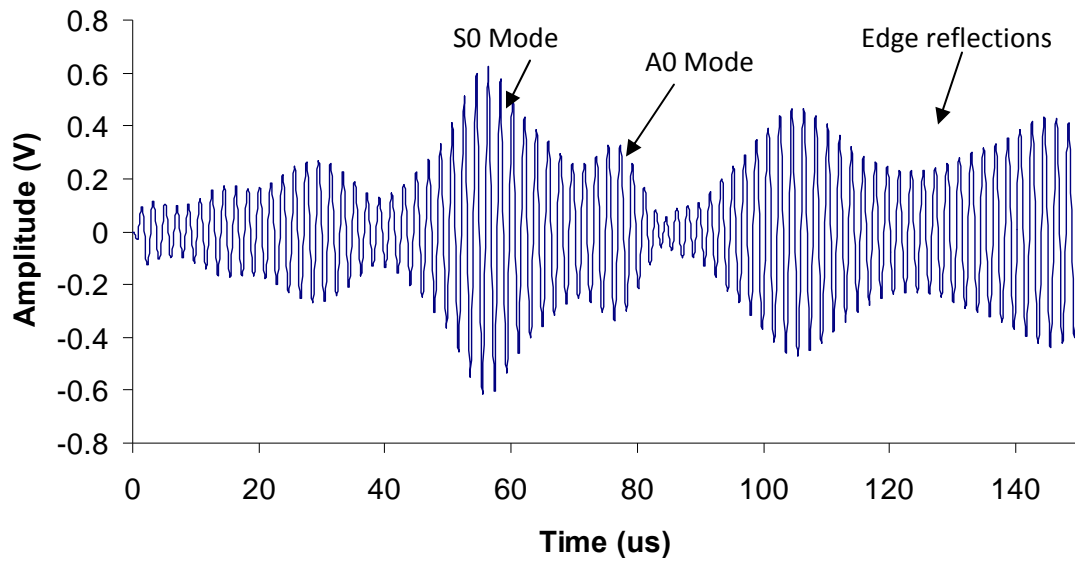


Figure 57: S0 mode generation with the phased annular array with amplitude and time delay to maximize S0 mode and suppress A0 mode

An angle beam transducer can be used to directionally receive the generated guided waves; the difference in the S0 mode amplitudes for the two different driving parameters can be seen in Figure 58. The A0 mode velocity being lower than Plexiglas it is not possible to record it using the angle beam transducer. It can be clearly noticed that the maximum S0 mode in the structure is generated for the parameters to maximize it. Similarly, it gets suppressed for the parameters to minimize it.

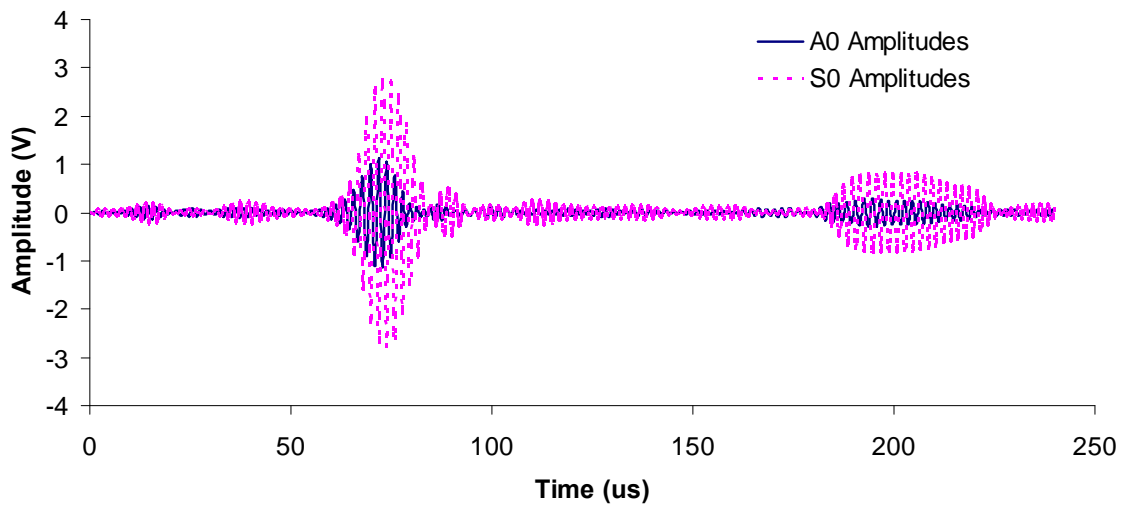


Figure 58: The received S0 mode with an angle beam transducer for transducer amplitude inputs to maximize A0 and S0 respectively

Phased array beam steering in anisotropic composite plates

The ultrasonic guided wave phased array technique offers an efficient means to interrogate damages in plate-like structures. When applying this technique to multilayer composite plates, however, the anisotropic behavior of the composite materials leads to significant influences on the beam steering performances of the phased arrays. In this project, we investigated the beam steering performances of guided wave phased arrays for multilayer composite plates in terms of phased array directivity profiles under influences of anisotropy. Angular dependences of guided wave amplitudes and phase variations in composite plates obtained through a Green's function based method were implemented into directivity profile calculations to account for the influences of anisotropy in a quantitative way. Guided wave phased array experiments were carried out to validate the directivity profile calculations.

Introduction of guided wave beam steering in composite plates

Due to the capability of interrogating a very long distance from a single inspection point and the overall excellent sensitivities to different types of defects, ultrasonic guided waves have been considered as a very promising tool in nondestructive evaluation (NDE) and structural health monitoring (SHM) communities. Compared to single element transducers, guided wave phased arrays have the advantages of providing higher penetration power and damage imaging capability as well as requiring less accessible inspection points, and thus have received more and more research attention.

Similar as in bulk wave phased array applications, a good control on directivity profiles is of paramount importance to the successful implementations of the guided wave phased array technique. Directivity profiles with narrow main lobes and low side lobe amplitudes are desired for high lateral resolutions and less image artifacts in phased array scanning images. On the basis of Huygens' Principle, mathematical formulations have been developed for calculating phased array directivity profiles for isotropic media. When material anisotropy is presented, however, the wave skew effects caused by the material anisotropy have to be taken into account in the directivity profile calculations. An analysis on field profiles of a single transducer in an anisotropic medium showed that the beam patterns experienced beam skewing, beam splitting and bending, as well as beam convergence due to the material anisotropy. Apparently, when applying guided wave phased arrays to anisotropic plates, for instance, multilayer fiber-reinforced composite plates that have been extensively used in the aircraft industry, the phased array directivity profiles determined by the beam patterns of single array elements together with the phase delays will be affected by the material anisotropy.

To quantitatively study guided wave phased array directivity profiles for multilayer composite plates, it is critical to first obtain the guided wave fields generated by a single element of the phased array. As mentioned in the previous report, the Green's function based method is one of the available techniques to predict circular-crested guided wave excitations in composite plates [Velichko 2007], [Yan 2008]. By calculating the convolutions of the Green's function for guided wave excitations with the loading function of the array element, the guided wave excitation of a transducer can be predicted. The method for evaluating the 3D Green's function was described in the first annual report of this project. The Green's function was used to calculate the circular-crested guided wave excitations in multilayer composite plates. The angular dependency on guided wave amplitudes and phase variations resulting from the Green's function calculations were then further implemented into the phased array directivity profile calculations. Experimental validations on the directivity profiles are carried out on a 32 layer carbon/epoxy composite plate.

Angular dependences of guided waves in composite plates

As given in the previous report, the 3D Green's function for far-field guided wave excitations in anisotropic multilayer composite plates can be approximately evaluated using the following equation:

$$\mathbf{g}^{(3)}(r, \varphi, z) = \sqrt{\frac{i}{2\pi r}} \sum_{\nu} e^{ir\Phi_{\nu}(\gamma_{\nu}, \varphi)} \mathbf{G}_{\nu}^{(3)}(\gamma_{\nu}, z) k_{\nu}(\gamma_{\nu}) \left[\frac{\partial^2 \Phi_{\nu}(\gamma_{\nu}, \varphi)}{\partial \gamma^2} \right]^{-1/2}, \quad (85)$$

where r , φ , and z are cylindrical coordinates, ν denotes the ν th guided wave mode, γ is the wave vector direction of the corresponding 2D straight-crested plane wave, $\mathbf{G}^{(3)}$ represents the wave number domain 3D Green's function, k represents the wave number, and Φ represents the phase variations. The guided wave modes included in the summation in equation (85) are determined from:

$$\frac{\partial [k_{\nu}(\gamma) \cos(\gamma - \varphi)]}{\partial \gamma} = 0. \quad (86)$$

Only the wave modes that satisfy equation (86) are included in equation (85). The wave number domain 3D Green's function of each mode can be calculated as:

$$\mathbf{G}_{\nu}^{(3)}(\gamma, z) = \mathbf{A}^{-1} [\bar{\mathbf{u}}_{\nu}(z)]^T \frac{\tilde{\bar{\mathbf{v}}}_{\nu}(d/2)}{4P_{\nu\nu}} \mathbf{A}, \quad (87)$$

where $\bar{\mathbf{u}}_{\nu}$ and $\bar{\mathbf{v}}_{\nu}$ are respectively the particle displacement and particle velocity distributions across the plate thickness that are obtained from the 2D straight-crested plane wave solutions for the ν th mode, the tilde represents complex conjugation, and the matrix \mathbf{A} is of format:

$$\mathbf{A} = \begin{bmatrix} \cos \gamma & \sin \gamma & 0 \\ -\sin \gamma & \cos \gamma & 0 \\ 0 & 0 & 1 \end{bmatrix}. \quad (88)$$

The phase variation function Φ in equation (85) is calculated for each mode using the following equation:

$$\Phi_v(\gamma, \phi) = k_v(\gamma) \cos(\gamma - \phi). \quad (89)$$

As shown in equation (85), the amplitudes of the guided wave fields generated even by axisymmetric loadings may distribute non-axisymmetrically. The phase variations of the wave fields in different directions may be different as well. The Green's function is capable of predicting the amplitudes and also the phase variations of the guided wave fields excited by any surface loadings in general composite plates. When considering point sources, the wave fields are given by the 3D Green's function itself. Since the phased array elements are generally smaller than the wavelength of the guided waves, besides, we are usually interested with the far field responses of the arrays, it is reasonable to consider the array elements as point sources. Therefore, the 3D Green's function given by equation (85) is suitable for guided wave phased array study on composite plates.

Using a surface loaded out-of-plane point source as an example, the angular dependence of the out-of-plane displacement excited by the source can be written as:

$$\alpha_g(\phi) = \left| \sqrt{2\pi} g_z^{(3)}(r, \phi, d/2) \right|, \quad (90)$$

where $\alpha_g(\phi)$ represents the amplitudes of the out-of-plane displacements that are normalized with respect to the distance to the point source, $g_z^{(3)}$ is the out-of-plane component of the 3D Green's function. The corresponding phase variations of the displacements are described by the phase term $\Phi_v(\gamma_v, \phi)$ as below:

$$\Phi_g(\phi) = \Phi_v(\gamma_v, \phi). \quad (91)$$

Equations (92) and (93) are evaluated for the third mode of an 8 layer quasi-isotropic composite plate at frequency 600 kHz. The layup sequence of the plate is $[0/45/90/-45]_2$. The elastic properties of a unidirectional layer are given in Table 7. The density and thickness of each layer are 1608 kg/m^3 and 0.2 mm , respectively. The third mode is the mode that is comparable to the S0 mode in isotropic plates.

Table 7: Elastic properties of the unidirectional lamina in the 8 layer quasi-isotropic composite plate

E_1	172 GPa
$E_2=E_3$	9.8 GPa
G_{23}	3.2 GPa
$G_{12}=G_{13}$	6.1 GPa
ν_{23}	0.55
$\nu_{12}=\nu_{13}$	0.37

The results are presented using polar coordinates in Figs. 85 and 86, respectively. Although the out-of-plane point source can be considered as an axisymmetric loading, the profiles of $\alpha_g(\phi)$ and $\Phi_g(\phi)$ are both non-axisymmetric. The displacement amplitude variation with respect to the angular direction behaviors is quite strong for the specific mode and frequency used here. The maximum amplitudes observed at the 18° and 198° directions are 12.8dB higher than the

minimum amplitudes at the 113° and 293° directions. The phase term $\Phi_g(\phi)$ also varies with directions. Obviously, if such a mode and frequency is selected for phased array beam steering, the angular variations of the displacement amplitudes and phases must be taken into account.

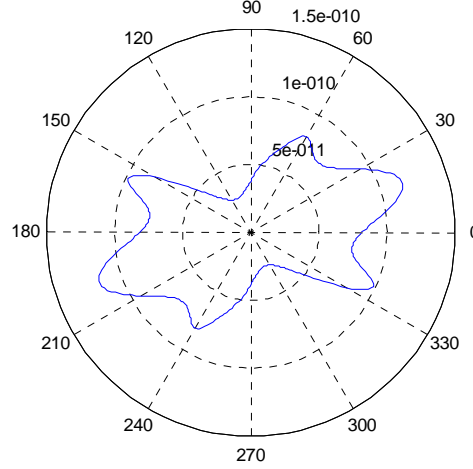


Fig.59: Angular dependence of the out-of-plane displacement of mode 3 at frequency 600 kHz excited by a unit out-of-plane point source.

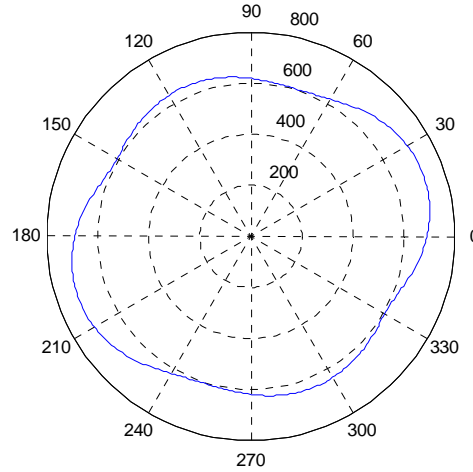


Fig.60: Angular dependence of the phase variation for the out-of-plane displacement of mode 3 at frequency 600 kHz excited by a unit out-of-plane point source.

Guided wave Phased array Directivity profiles

It has been shown elsewhere that the directivity profiles of a guided wave phased array for isotropic plates can be calculated as:

$$P_{isotropic}(\phi) = \sum_n \exp\left\{-ik(\vec{\phi} \cdot \vec{s}_n - \vec{\phi}_0 \cdot \vec{s}_n)\right\}, \quad (92)$$

where $\vec{\phi}_0$ is the unit vector pointing to the beam steering direction and \vec{s}_n denotes the position vector of the n th array element. To calculate the directivity profiles of phased arrays in composite plates, one needs to replace the wave number k in equation (8) with the phase term $\Phi_g(\phi)$ and also include the angular dependent amplitude factor $\alpha_g(\phi)$. The modified directivity profile calculation formula is given by:

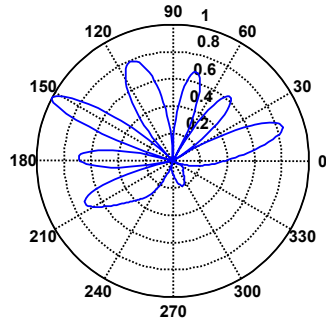
$$p(\phi) = \sum_n \alpha_g(\phi) \exp\{-i(\Phi_g(\phi)\vec{\phi} \cdot \vec{s}_n - \Phi_g(\phi_0)\vec{\phi}_0 \cdot \vec{s}_n)\}. \quad (93)$$

If a circular array is used, equation (93) can be rewritten as:

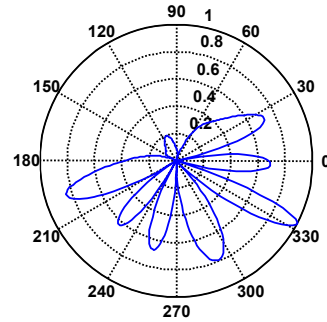
$$p(\phi) = \sum_n \alpha_g(\phi) \exp\{-iR[\Phi_g(\phi)\cos(\psi_n - \phi) - \Phi_g(\phi_0)\cos(\psi_n - \phi_0)]\}, \quad (94)$$

with R representing the radius of the circular array.

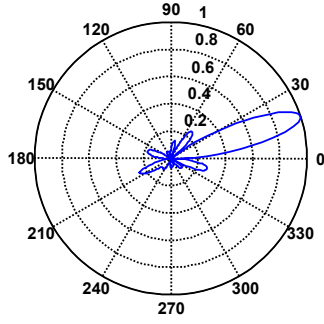
Directivity profiles of a 16 element circular array are calculated using equation (94) for the mode 3 at frequency 600 kHz. The radius of the array is 10 mm. Based on the observations made on the angular dependence of the amplitude, we know that the out-of-plane displacement amplitude is very small at the directions of 113° and 293° as compared to the amplitudes at the 18° and 198° directions. As a result, when phasing the guided wave signals for a constructive interference in the 113° or 293° direction, the amplitude of the guided wave displacement in the beam steering direction is still small compared to the other directions, especially the directions of 18° and 198° . The normalized directivity profiles for the beam steering angles 113° and 293° are respectively given in Fig. 61 (a) and (b). As can be seen, although there are indications of constructive interferences in the beam steering directions, the strong lobes appearing in other directions make the guided wave beam steering fail. By contrast, as can be seen from the normalized directivity profiles shown in Fig. 61 (c) and (d), the beam steering results for the 18° and 198° directions have relatively strong main beam and small side lobes.



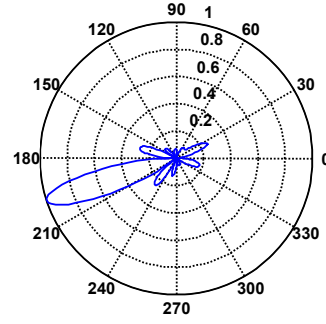
(a) 113°



(b) 293°



(c) 18°

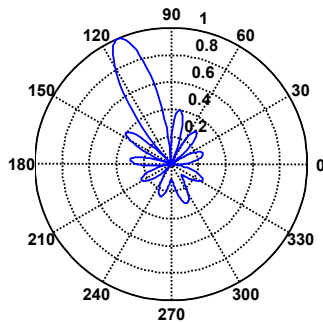


(d) 198°

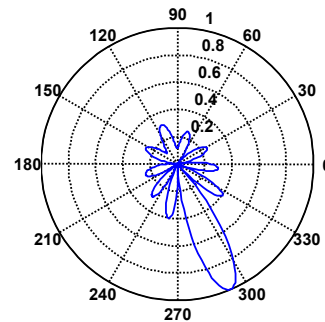
Fig. 61: Directivity profiles of a 16 element circular array for the guided wave mode 3 at frequency 600 kHz in the 8 layer quasi-isotropic plate. The beam steering angles are: (a) 113° , (b) 293° , (c) 18° , and (d) 198° .

The directivity profiles calculated for the same array and beam steering directions using the formula for isotropic plates are shown in Fig. 62. In the calculations, the amplitude factor $\alpha_g(\phi)$ is set to 1 for all directions, whereas for the phase term $\Phi_g(\phi)$, the value of $\Phi_g(0)$ is used for all directions. Comparing Fig. 62 (c) and (d) to Fig. 61 (c) and (d), one can see that the influence of anisotropy actually improves the array directivity profiles for the 18° and 198° beam steering directions. This is due to the fact that such directions are the directions in which the guided wave energy naturally focused together. Despite the good directivity profiles obtained for the 18° and 198° directions, the influence of anisotropy is considered undesired for the phased array beam steering in this case because the beam steering for other directions, say, for example, the 113° and 293° directions, are of extreme side lobes.

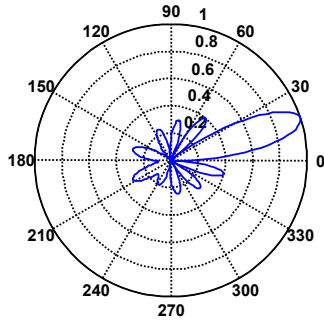
Since the function $\alpha_g(\phi)$ and the phase terms $\Phi_g(\phi)$ vary from one point to another in the dispersion curves of composite plates, it is possible to select guided wave modes and frequencies with quasi-isotropic behavior for the purpose of suppressing the influence of anisotropy in guided wave phased array applications. The mode 1 that is comparable to the A0 mode in isotropic plates is identified with quasi-isotropic behavior at low frequency range. The mode 1 at 160 kHz is selected as an example to demonstrate the feasibility of suppressing the influence of anisotropy for the phased array applications in the 8 layer quasi-isotropic plate. The angular dependence of $\alpha_g(\phi)$ and $\Phi_g(\phi)$ are respectively shown in Fig. 63 (a) and (b) for the selected mode and frequency.



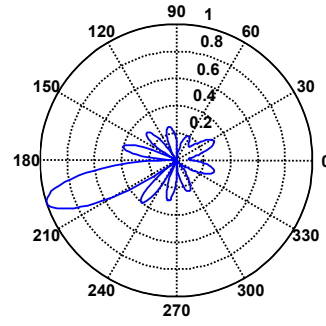
(a) 113°



(b) 293°

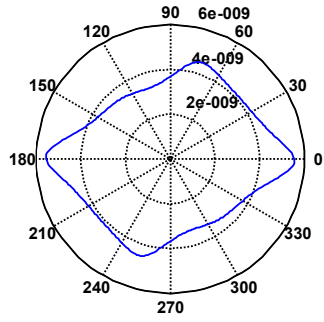


(c) 18°

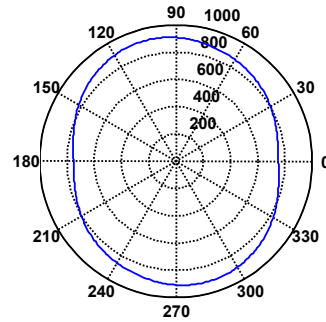


(d) 198°

Fig. 62: Directivity profiles of the 16 element circular array calculated using the formula for isotropic plates. The beam steering angles are: (a) 113° , (b) 293° , (c) 18° , and (d) 198° .



(a) $\alpha_g(\phi)$

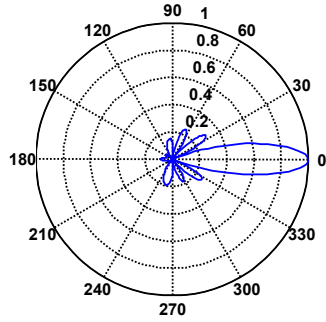


(b) $\Phi_g(\phi)$

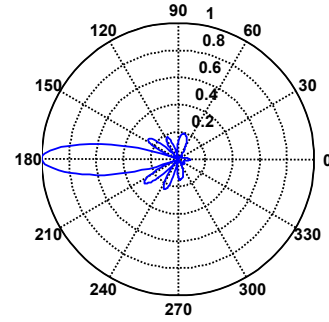
Fig. 63: Angular dependences of the out-of-plane displacement amplitudes and the phase terms for the mode 1 of the 8 layer quasi-isotropic plate at frequency 160 kHz.

The directivity profiles of a 16 element circular array calculated for the mode 1 at 160 kHz after considering the influences of anisotropy are shown in Fig. 64 for the beam steering angles 0° , 180° , 42° , 222° , 110° , and 290° . The radius of the array is 8 mm. At the angles 0° and 180° , the function $\alpha_g(\phi)$ has its maximum value. The minimum value of the function $\alpha_g(\phi)$ appears at the angles 110° and 290° . The angles 42° and 222° give another local minimum value.

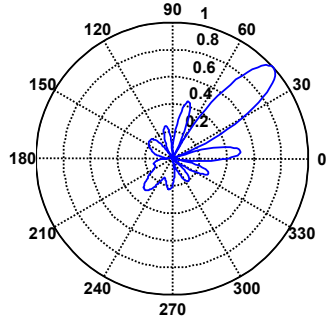
It can be shown by comparing Fig. 64 with the corresponding isotropic case that the directivity profiles for the beam steering directions 0° and 180° are improved by the influence of anisotropy. The directivity profiles for the 42° , 222° , 110° , and 290° directions, by contrast, become worse in terms of having stronger side lobes. However, since the fluctuations of the amplitude and phase angular dependences are not as severe as the ones of the mode 3 at frequency 600 kHz, instead of having failures on beam steering as shown in Fig. 61 (a) and (b) for the mode 3 case, the directivity profiles for the mode 1 at frequency 160 kHz are still applicable. Increased side lobe levels are the price to pay for the influence of anisotropy.



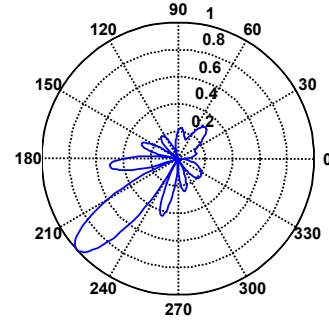
(a) 0°



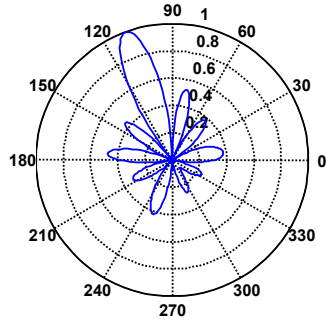
(b) 180°



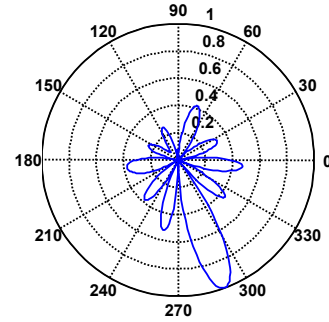
(c) 42°



(d) 222°



(e) 110°



(f) 290°

Fig. 64: Directivity profiles of a 16 element circular array for the mode 1 at frequency 160 kHz. The radius of the array is 8 mm. The beam steering angles are: (a) 0° , (b) 180° , (c) 42° , (d) 222° , (e) 110° , and (f) 290° .

Experiments and results

Guided wave beam steering experiments were carried out on a composite plate. The plate is a 32 layer carbon/epoxy fiber-reinforced composite plate fabricated by ATK, Inc. The fabrication data of the plate is given in Table 8. The finished plate thickness was measured at 6mm. The

elastic properties of the unidirectional Hexcel AS4/8522 tape used in guided wave calculations are given in Table 9. For the woven fabric Hexcel AS4/8522S, averaged elastic properties of a 0 degree tape and a 90 tape were applied. Equal ply thicknesses were assumed.

Table 8: Detailed plate fabrication sheet for the composite plate used in the experiments

Technician Name		Surface Ply Material		Panel Identification ID:		
Dan Goodrick		FEP surface		Chris Deemer NDI 11-29-07 S108 2000		
Date/Time Kit from Freezer: Tape: 1700/12/3/07 Fabric: 1000/11/27/07		Temperature (°F) 69° RH: 15%		Fabric: Hexcel AS4/8552S Pre-Preg Fabric AGP193P(NT)8552S; 38%, 193AW; 50",Lot: S4477SQ		
Date/Time Lay-up Started:		Date/Time Lay-up Ended:		Tape: Hexcel AS4/8552 Tape AS4 12k/8552; 35%; 190AW; 48" Lot P6939-4SQ		
Ply No.	Material	Orientation	Flag size	Debulk Check √ or N/A		Notes
1	Fabric	0/90°	48" x 48"	Optional		
2	Fabric	0/90°	48" x 48"	Optional		
3	Tape	+45°	48" x 48"	Optional		
4	Fabric	0/90°	48" x 48"	Mandatory	x	
5	Tape	-45°	48" x 48"	Optional		
6	Fabric	0/90°	48" x 48"	Optional		
7	Tape	+45°	48" x 48"	Optional		
8	Tape	90°	48" x 48"	Mandatory	x	
9	Tape	90°	48" x 48"	Optional		
10	Tape	-45°	48" x 48"	Optional		
11	Tape	0°	48" x 48"	Optional		
12	Tape	+45°	48" x 48"	Mandatory	x	
13	Tape	90°	48" x 48"	Optional		
14	Tape	-45°	48" x 48"	Optional		
15	Tape	0°	48" x 48"	Optional		
16	Tape	+45°	48" x 48"	Mandatory	x	
17	Tape	+45°	48" x 48"	Optional		
18	Tape	0°	48" x 48"	Optional		
19	Tape	-45°	48" x 48"	Optional		
20	Tape	90°	48" x 48"	Mandatory	x	
21	Tape	+45°	48" x 48"	Optional		
22	Tape	0°	48" x 48"	Optional		
23	Tape	-45°	48" x 48"	Optional		
24	Tape	90°	48" x 48"	Mandatory	x	
25	Tape	90°	48" x 48"	Optional		
26	Tape	+45°	48" x 48"	Optional		
27	Fabric	0/90°	48" x 48"	Optional		
28	Tape	-45°	48" x 48"	Mandatory		
29	Fabric	0/90°	48" x 48"	Optional		
30	Tape	+45°	48" x 48"	Optional	x	
31	Fabric	0/90°	48" x 48"	Optional		
32	Fabric	0/90°	48" x 48"	Mandatory	x	

Table 9: Detailed plate fabrication sheet for the composite plate used in the experiments

E_1	135 GPa
$E_2=E_3$	9.5 GPa
G_{23}	3.65 GPa
$G_{12}=G_{13}$	4.9 GPa
ν_{23}	0.3
$\nu_{12}=\nu_{13}$	0.3

An 8 element circular phased array was attached to the center of the composite plate using instant glue. Each array element is a piezoceramic rod with 5.08 mm diameter and 12.7 mm thickness. The first thickness resonant frequency of the array elements was tested to be around 100 kHz. A layer of Tungsten powder loaded epoxy was applied to the back of each array element to serve as a transducer backing. The radius of the array is 8mm. A picture of the array attached to the composite plate is shown in Fig. 65. In the experiments, the array elements were driven by 5 cycle 100 kHz square wave signals. Because of the thickness resonant frequency of the array elements, the loads applied by the array elements were in the out-of-plane direction. The mode 1 was hence selected due to its high out-of-plane excitability. The out-of-plane excitability values for the modes 2 and 3 at 100 kHz were neglectable when comparing to the corresponding value of the mode 1.

To measure the directivity profiles of the array for different beam steering directions, an 8 channel time delay control system developed by FBS, Inc. was used to apply phase delays. Another piezoceramic element was employed to receive the phased array outputs in different circumferential directions but with the same distances from the center of the array under the through-transmission mode. Obviously, if the phased delays for beam steering were effective, the maximum wave amplitude should be observed when the receiving element locates in the beam steering direction. The plots of the wave amplitudes versus the corresponding circumferential directions of the receiving element can be further compared to the phased array directivity profiles.

The experimental results are shown in Fig. 66 (a)-(f), in terms of normalized wave amplitude plots for beam steering angles starting from 0° to 300° with a 60° increment. The corresponding theoretically calculated array directivity profiles are also shown for comparison. As can be seen, the maximum amplitudes were always received at the corresponding beam steering directions. The beam steering of the phase array was thus proven successful. The experimental results also matched with the calculated directivity profiles quite well. The good matches between the experimental results and the calculated ones proved that the design of array elements controlled the influence of anisotropy quite well so that the guided wave energy generated by the circular array can be steered to any direction in the plate. The minor discrepancies could be mainly introduced by the inconsistent contact conditions between the receiving piezocomposite element and the plate surface at different measurement locations. The inaccuracies on array element placements also contributed to the discrepancies.

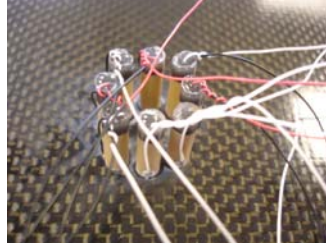
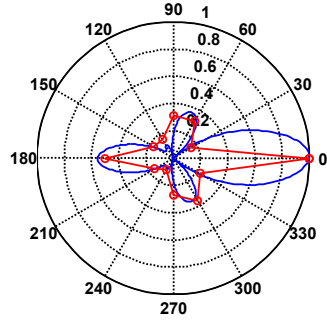
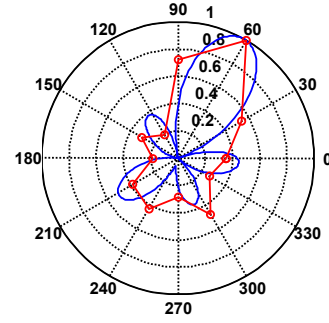


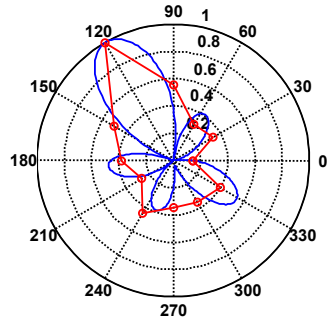
Fig. 65: A close view of the 8 element circular array attached to the center surface of the composite plate



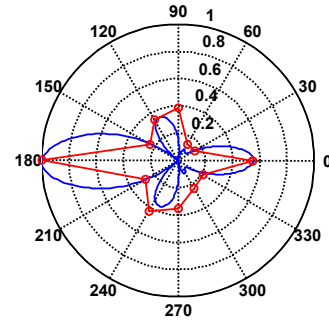
(a) 0° direction beam steering



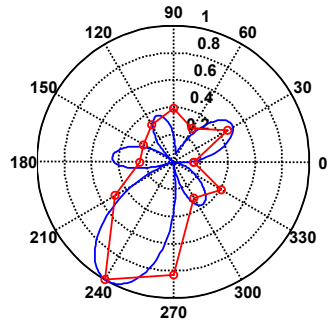
(b) 60° direction beam steering



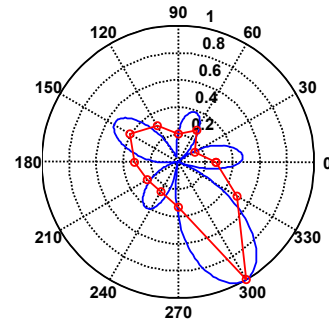
(c) 120° direction beam steering



(d) 180° direction beam steering



(e) 240° direction beam steering



(f) 300° direction beam steering

Fig. 66: Comparisons between experimental results with calculated array directivity profiles for the beam steering angles of (a) 0° , (b) 60° , (c) 120° , (d) 180° , (e) 240° , and (f) 300° . Very good agreements were obtained.

Defect detection in a composite plate using a phased array

The defect detection capability of the phased array was examined using the pulse-echo mode of the time delay control system. A baseline dataset was first taken by applying the time delays to scan the whole plate with a 1° angular increment. A notch was cut and introduced to the plate as the simulated defect. The notch was located at the 150 degree circumferential angle. The distance from the notch to the center of the array was 140mm. The length of the notch was about 25mm. The depth of the cutting was close to 1.3mm. A new dataset was collected with the same settings and angular increment as was used for the baseline data set after the cutting notch was introduced. For each beam steering angle, the 8 signals received by the 8 elements of the array were synthesized using the back-propagation method to yield the defect inspection result in a spatial distribution format for the beam steering angle. The inspection image was generated by subtracting the baseline results from the results obtained using the new dataset and then plotting the envelopes of the residuals with respect to the beam steering angles.

The inspection image for the notch is shown in Fig. 67 in dB scale. The vicinity of the phased array in the image that corresponds to the cross-talk signals (signals for the waves that traveled directly in between array elements) was taken out from the image to enhance the appearance of the defect indication. The dB range for the part of the inspection image shown in Fig. 67 is 8dB. As can be seen, the notch was detected in the beam steering inspection image really well. The circumferential and radial locations of the notch in the image were 149° and 134mm, respectively.

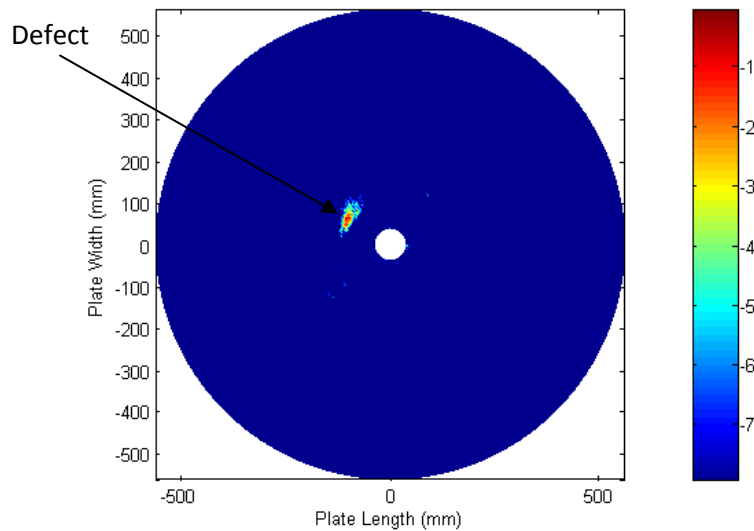


Fig. 67: Defect inspection image obtained using the phased array beam steering technique for the notch in the 32 layer composite plate.

Phased Beamformer Transducer Design

The phased beamformer transducer employs the phased annular array guided wave mode control in conjunction with real time phasing for guided wave beamsteering. The result is a transducer in which all the elements can be individually controlled for real-time mode control and directionality. 1-3 piezo-fiber composites are used in the design of the transducer, the cross-talk between the transducer elements in a piezocomposite is lower than -30 dB the highest cross-talk occurring at the thickness resonance. Taking advantage of the low cross-talk between elements in a piezocomposite a single wafer patterned with the desired electrode pattern is used. For very fine dimensions soldering wires to electrodes becomes a very challenging task, in such cases using a flexible printed circuit board as the transducer electrode will be helpful as it can be readily possible to connect solderable pads to the electrodes. However, care should be taken while bonding the flexible printed circuit board to minimize the bondline, the low dielectric constant of the bondline can reduce the strength of the electric field lines significantly and affect the performance of the transducer.

The number of elements in each transducer array presents a significant challenge in the transducer design. The beamforming process imposes several restrictions on the element size and their spacing. For a uniform circular array the spacing between the circular elements should not exceed $\lambda/2$. Hence, three annular array elements per transducer are used as a compromise between mode selection and beamformability. The number of elements in the annular array affects the excitation spectrum of the guided waves being excited in the structure. Care should be taken to operate the transducer at frequencies where mode isolation is possible. The full transducer once made should incorporate a matching and a backing layer to enhance the bandwidth of operation of the transducer. For the transducer fabricated in Figure 68, no matching and backing layers were used, the impedance of the transducer closely matches the aluminum plate.

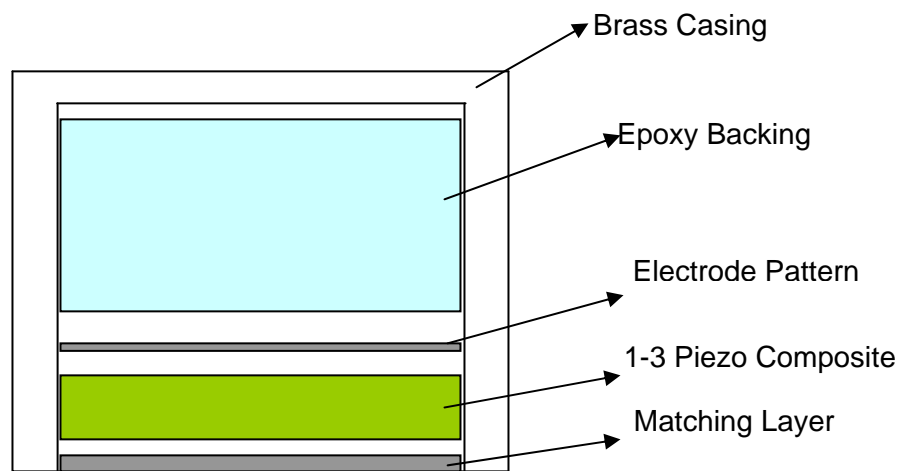


Figure 68: Schematic of Beamformer transducer

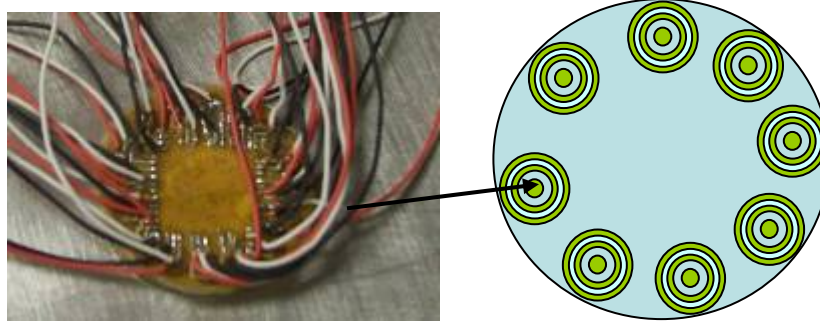


Figure 69: Beamforming transducer with 16 phased annular arrays in a circular array

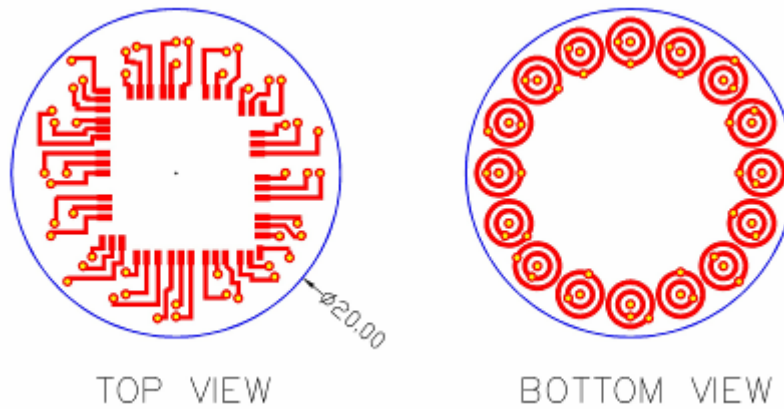
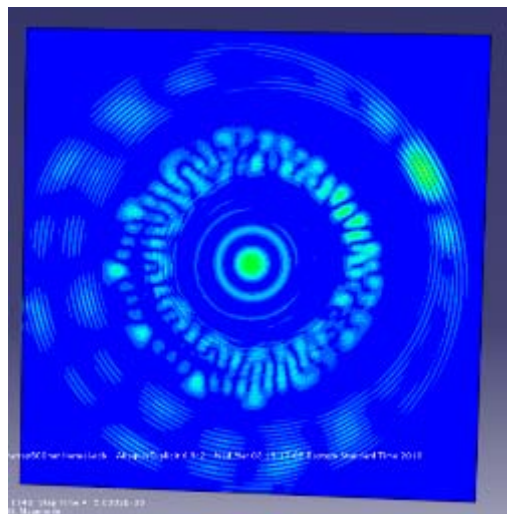
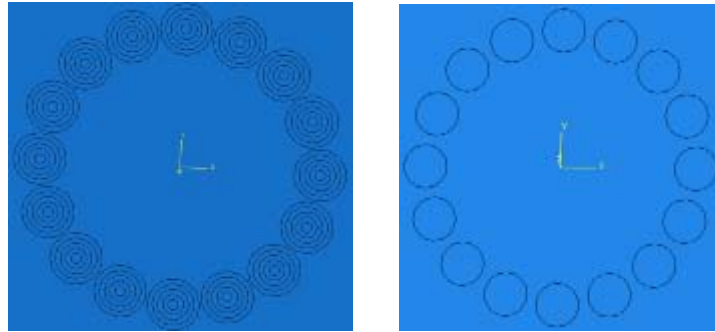


Figure 70: Top and Bottom view of the flexible printed circuit board used as the electrode

Finite element modeling of guided wave beam forming

Finite element modeling is employed to study the guided wave beamforming in structures. ABAQUS software is used to model the wave propagation, 3D linear stress elements are used to study wave propagation. Figure 71 shows the two configurations studied namely the loading due to a normal beam transducer and the other is loading due to a phased annular array transducer. The phased annular array transducer is loaded with amplitude and time delays corresponding to the A0 mode generation at 300 kHz in a 4.8 mm thick plate. As mentioned above with no mode control the unwanted guided wave interferes with the beamforming process as can be seen in Figure 72 with S0 beamformed along the 30^0 direction while for the same time delays the A0 mode aliases which can be noticed. With guided wave mode control the A0 mode beamforming can be seen in Figure 73 with clean A0 mode generated and propagating in the structure.



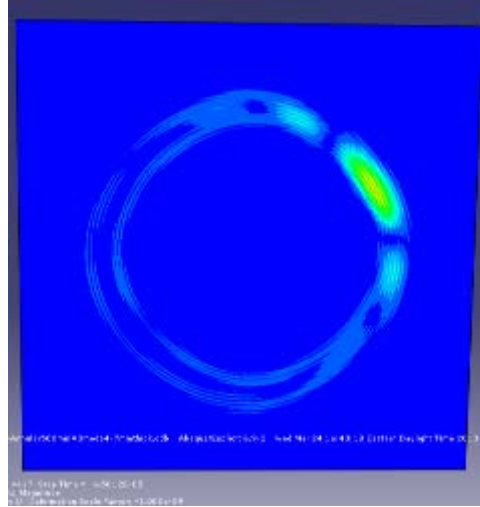


Figure 73: Magnitude of displacement for A0 mode beamforming in a 500 x 500 x 4.7 mm³ aluminum plate with phased annular array loading at 300 kHz

Experiments on an isotropic plate

The phased array experiments are carried using a data acquisition machine built with multi-channel phased array cards. The system has 8 channels and each channel can have independent time delays. However, the minimum number of transducer elements needed to carry out a real time experiment is 16 and for phased annular array beamforming it multiplies to 48 independent channels. Hence, it was decided to carry out synthetic beamforming in which case the constraint on the number of channels can be overcome. Experiments are carried out on aluminum plates with different defects on the plates.

PWAS (piezoelectric wafer active sensors) transducers are disk type transducers predominantly operated in the d31 mode. The shear type of actuation of the d31 mode results in a predominant S0 mode. The transducer diameter of 6.35 mm results in a radial resonance of 350 kHz. To reduce the ringing and increase the bandwidth of the transducer an attenuative epoxy backing is used. The backing considerably improves the performance of the transducer by reducing the ringing. A circular array with radius 18 mm is chosen and transducers are bonded on a 1 mm thick aluminum plate. The S0 mode is used to image the plate for defects, there are several defects that are introduced into the structure Table 10 gives the location and size of the defects. The Corrosion defect is introduced using accelerated electrolysis technique were in salt water and a battery are used corrode the plate, a saw cut defect and several through holes are made manually. The images obtained after beamforming can be seen in Figure 75 and after applying deconvolution in Figure 76. Thresholding the image to -11 dB the image with defects can be seen in Figure 77.

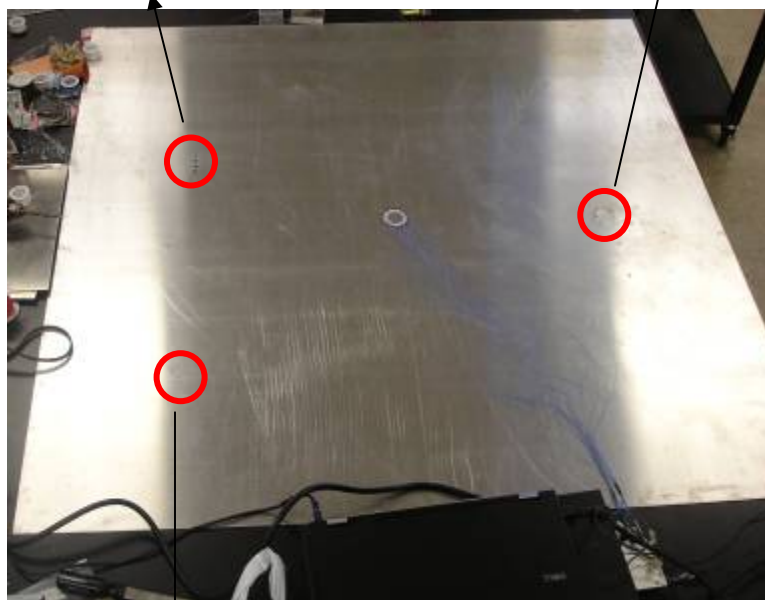
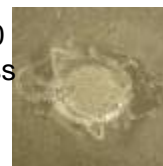
Table 10: Defects introduced into the aluminum plate

Defect	Location from center (mm)	Size (mm)
Corossion	400	25.4 dia
Crack	520	50.8 mm
Holes	400	6.1 mm dia

¼ " dia



1" dia corrosion, 50 % through thickness



2" wide crack, 50 % through thickness

Figure 74: Aluminum plate with several defects

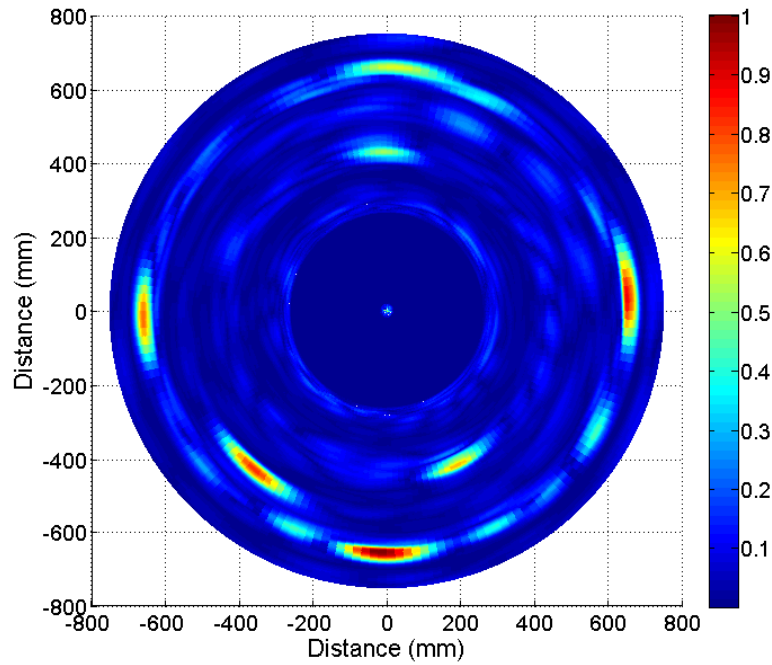


Figure 75: Phased array image of the aluminum plate with defects

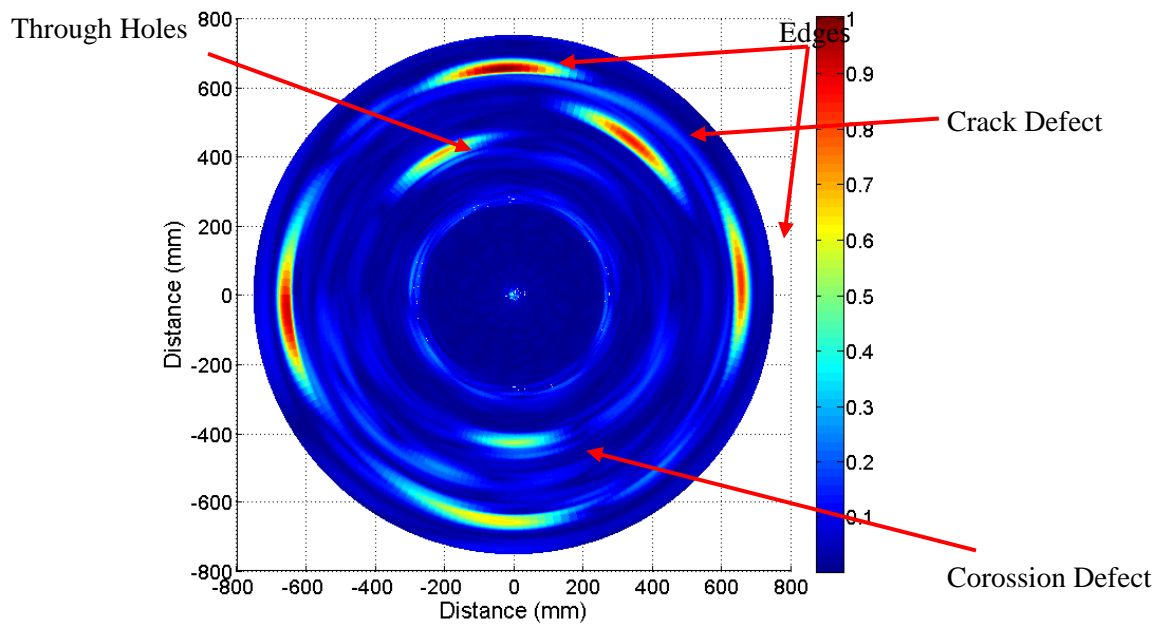


Figure 76: Phased Array Image of an aluminum plate with defects after deconvolution

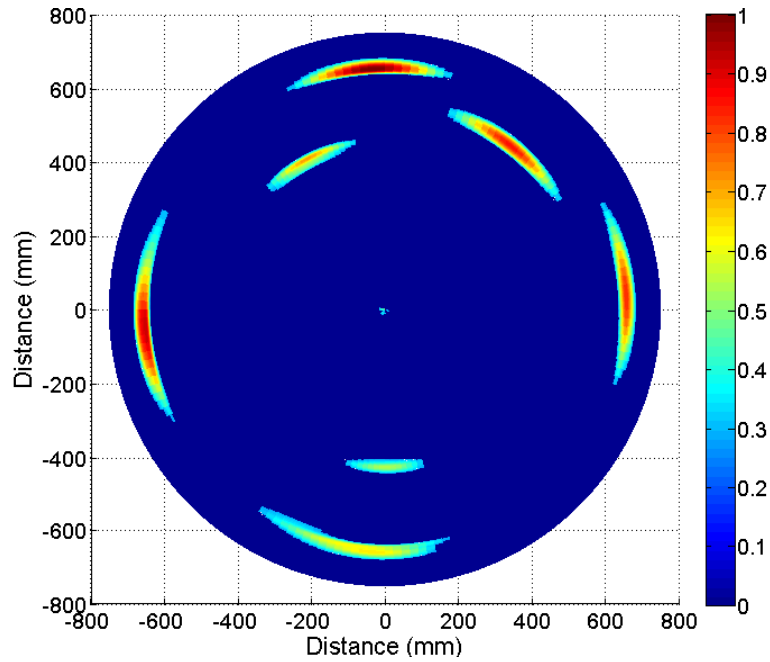


Figure 77: Phased array image after thresholding

A beamformer transducer with 16 array elements is designed using a 1-3 piezofiber composite. Each array element has three annular rings for controlling the guided wave mode generated in the structure. With a phased annular array transducer size mentioned in Table 10, the 16 element beamformer transducer has a diameter of 16 mm giving an overall transducer dimension of 19 mm. The transducer is mounted on a 4.8 mm thick aluminum plate, the transducer is operated at 700 kHz. A saw cut defect of length 2" and 50 % through thickness is made and the defect is imaged with the transducer. The defect image with simple phased addition can be seen in Figure 79 and the image after deconvolution and thresholding can be seen in Figure 80.

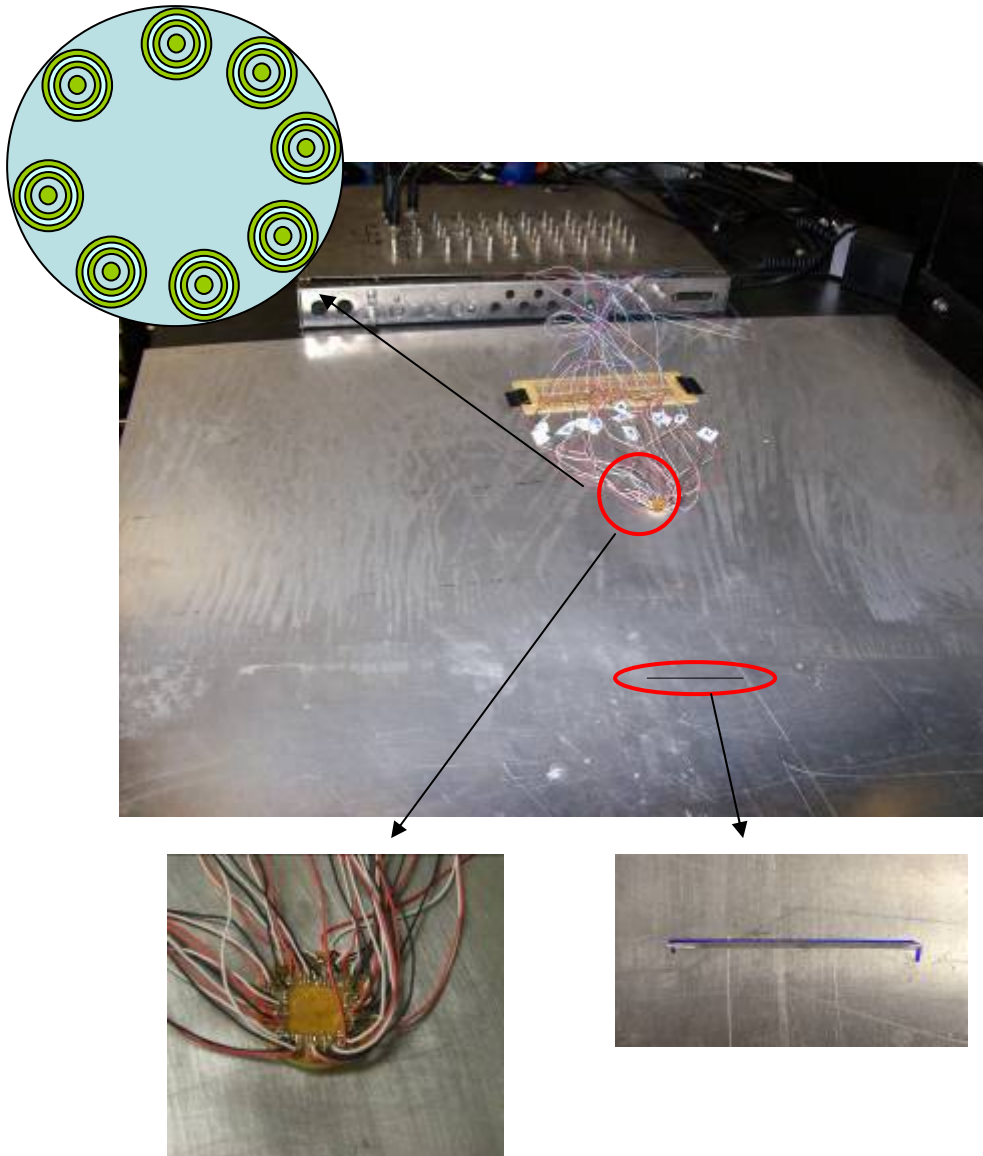


Figure 78: Phased Annular beamforming experiment setup

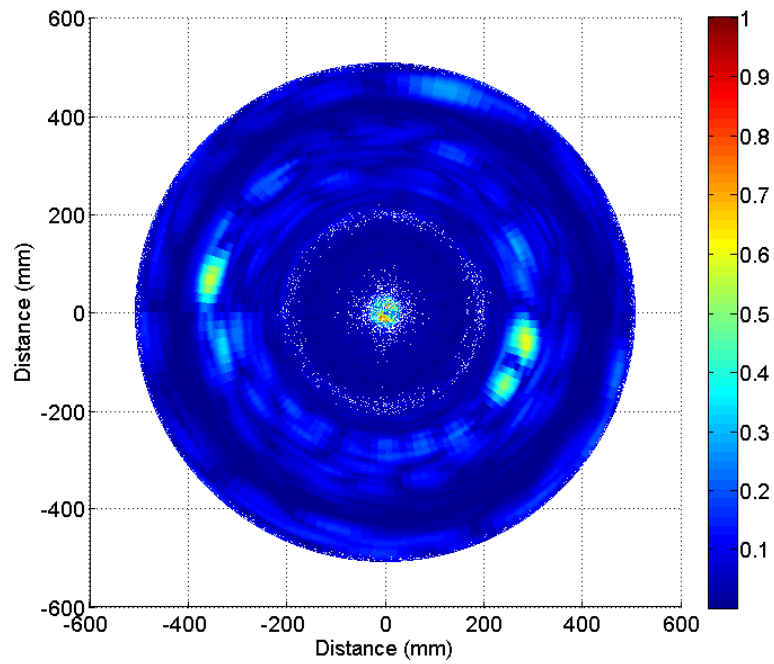


Figure 79: Phased Annular array defect Image showing a crack defect

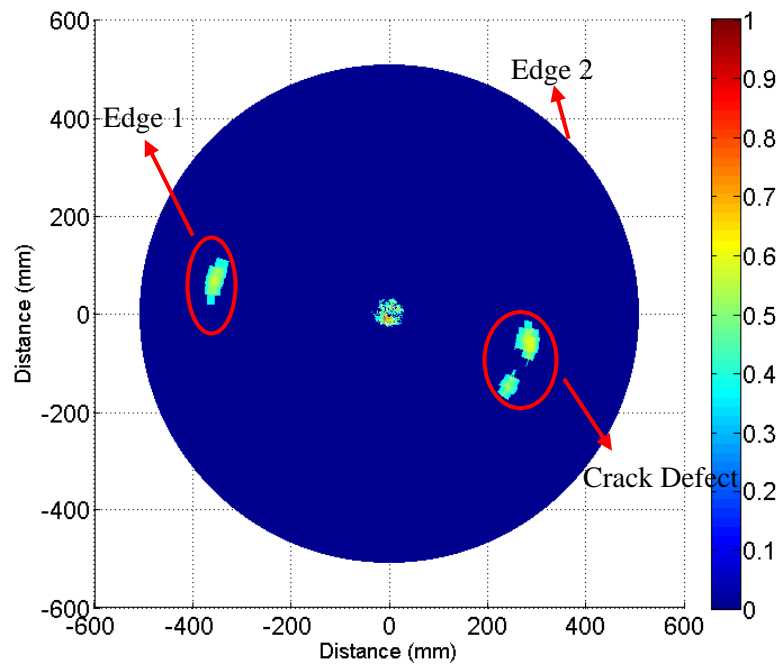


Figure 80: Phased Annular array defect image after thresholding

Guided wave mode control with Phased Annular Array transducers

Phased annular array transducers can be used for guided wave mode control in composites. By controlling the amplitude and phase of the elements in a transducer it is possible to control the guided wave modes by minimizing the energy of the unwanted mode. The optimization problem to determine the optimum excitation parameters namely the amplitude and phase of elements was discussed in earlier sections. The same mathematical concepts are valid for composite structures except that the greens function is dependant on the direction. The energy associated with a guided wave mode due to surface excitation need to take into account the angular dependence of the wave number which can be written as in Equation (95).

$$EN_0^h = \omega \text{Im} \int_0^{2\pi} \int_0^\infty (G(k, \gamma, 0) \sum_{m=1}^M V_m Q(k), \sum_{m=1}^M V_m Q(k)) k dk d\gamma \quad (95)$$

$$EN_0^h = \omega \text{Im} \int_0^{2\pi} (\text{res}(G(k, \gamma, 0)) \Big|_{k=k_v} \sum_{m=1}^M V_m Q(k), \sum_{m=1}^M V_m Q(k)) k_v d\gamma \quad (96)$$

The integral in Equation (96) can be numerically integrated for contributions from all the angles which can be expressed in terms of the excitation parameters as in Equation (97).

$$EN_v^h = \sum_{i=1}^M \sum_{j=1}^M a_{ij}^v V_i V_j^* = (A \hat{V}, \hat{V}) \quad (96)$$

$$a_{ij}^v = \frac{\omega}{4} \left(\sum_{\gamma} (\text{Re } s(G(k, \gamma, 0)) \Big|_{k=k_v}) Q_j(k_v) Q_i(k_v) k_v \right) \delta\gamma \quad (97)$$

The optimum excitation parameters can now be calculated using the same procedure outlined for isotropic plates earlier. At low frequencies where only two fundamental guided wave modes exist and the skew angle being very low they can be treated as having quasi-isotropic behavior and calculated similar to that for isotropic plates can be carried out knowing the greens function for the structure. Table 11 shows the array element dimensions and the calculated excitation parameters for S0 mode maximization at 400 kHz. Figure 81 shows the guided wave signal received in the composite with a normal beam transducer with no mode control. Applying the amplitude and time delays for maximizing mode 3 the corresponding waveform in the composite plate can be seen in Figure 82. An angle beam receiver can be used to confirm the existence of mode 3 in the structure which can be seen in Figure 83. This mode control can be employed for beamforming to improve defect imaging.

Table 11: Phased annular array parameters for guided wave mode generation in composites

Element	Inner Radius (mm)	Outer Radius (mm)	Mode 3	
			Amplitude	Time delay (us)
1	0	0.8	0.7508	0

2	1.6	2.4	0.2490	1.65
3	3.2	4.0	0.6118	0

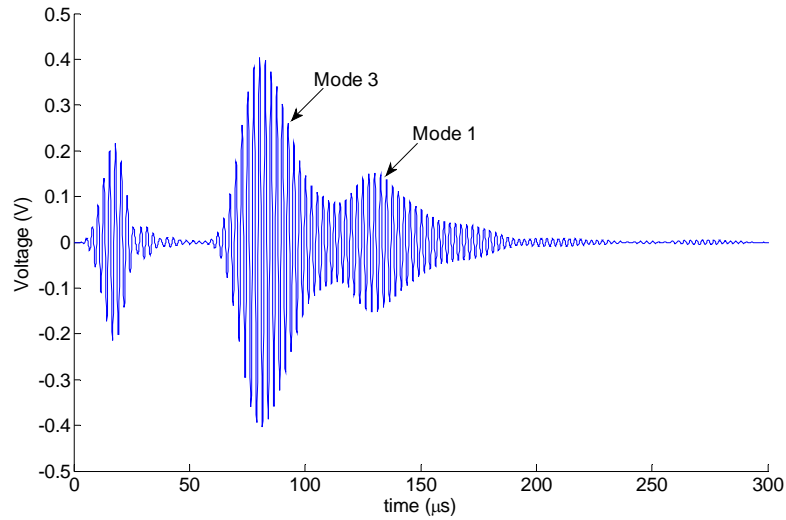


Figure 81: Received signals with a normal beam receiver at a distance 10.5 inches from the transmitter with constant amplitude and no time delays

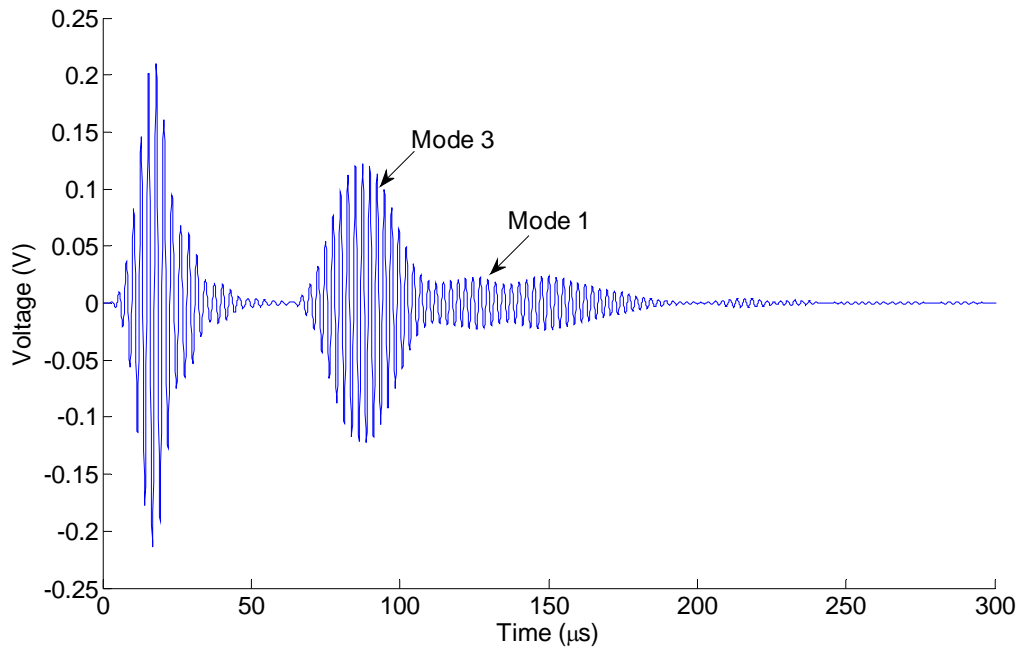


Figure 82: Normal beam receiver at a distance 10.5 inches from the annular array transmitter with amplitude and time delays to maximize mode 3

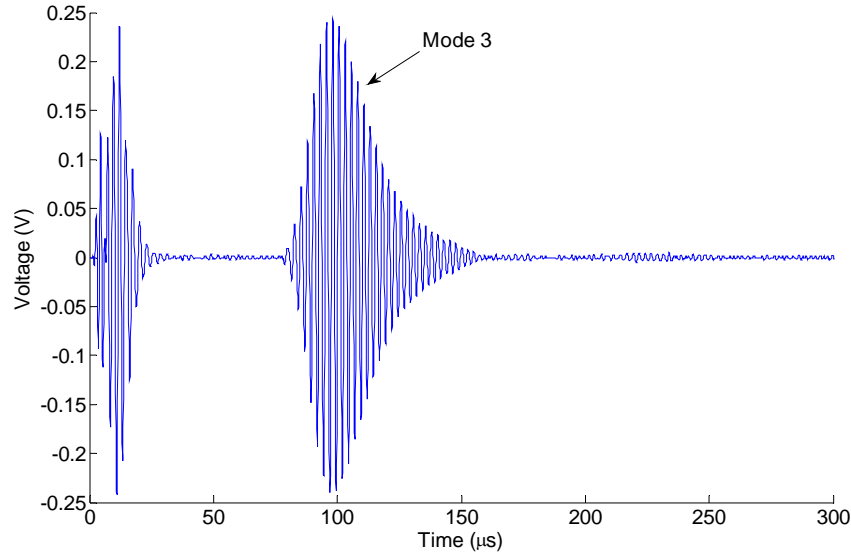


Figure 83: Signal Received by an angle beam transducer with amplitude and time delay to maximize mode 3

Beamforming with a Phased Annular Beamformer Transducer

In the previous section PWAS sensors are used to beamform and image defects in the structure. The group velocities of the fundamental modes being very different the modes were temporally separated and used for imaging. However, at other frequencies the temporal separation between guided wave modes becomes very difficult. Using the phased annular array transducers for mode control gives the advantage of mode control and hence better imaging. A phased beamformer transducer is fabricated with 10 annular array transducers with 3 elements each. The transducer is fabricated using a 1-3 Piezocomposite material made from randomly placed 65% piezo-fiber composite (supplied by Smart Material Corporation). The transducer elements are patterned using lithography. Figure 84 shows the final mounted transducer on a composite plate. No matching is layer is used for the transducer while a light epoxy backing is used to damp the transducer. The element dimensions in the annular array are given in Table 11, the annular array transducers are arranged in a circular pattern for beam steering. A 16 layer AS4/8552 quasi-isotropic composite is manufactured; the delamination is simulated by introducing a Teflon patch 2"x2" at the mid-plane, i.e. between layers 8 and 9. The defect is placed 10" from the center of the plate, the C-scan of the plate can be seen in Figure 85. Synthetic beamforming is carried out using the phased annular beamformer transducer mounted on the plate.

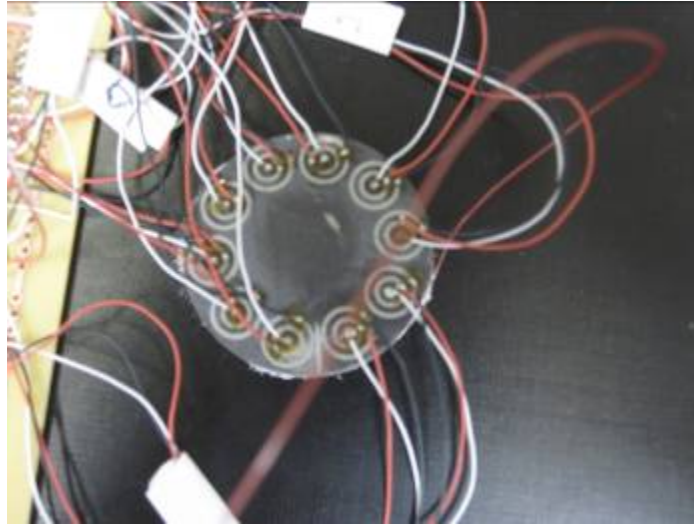


Figure 84: 10 element circular array with 3 annular rings per element

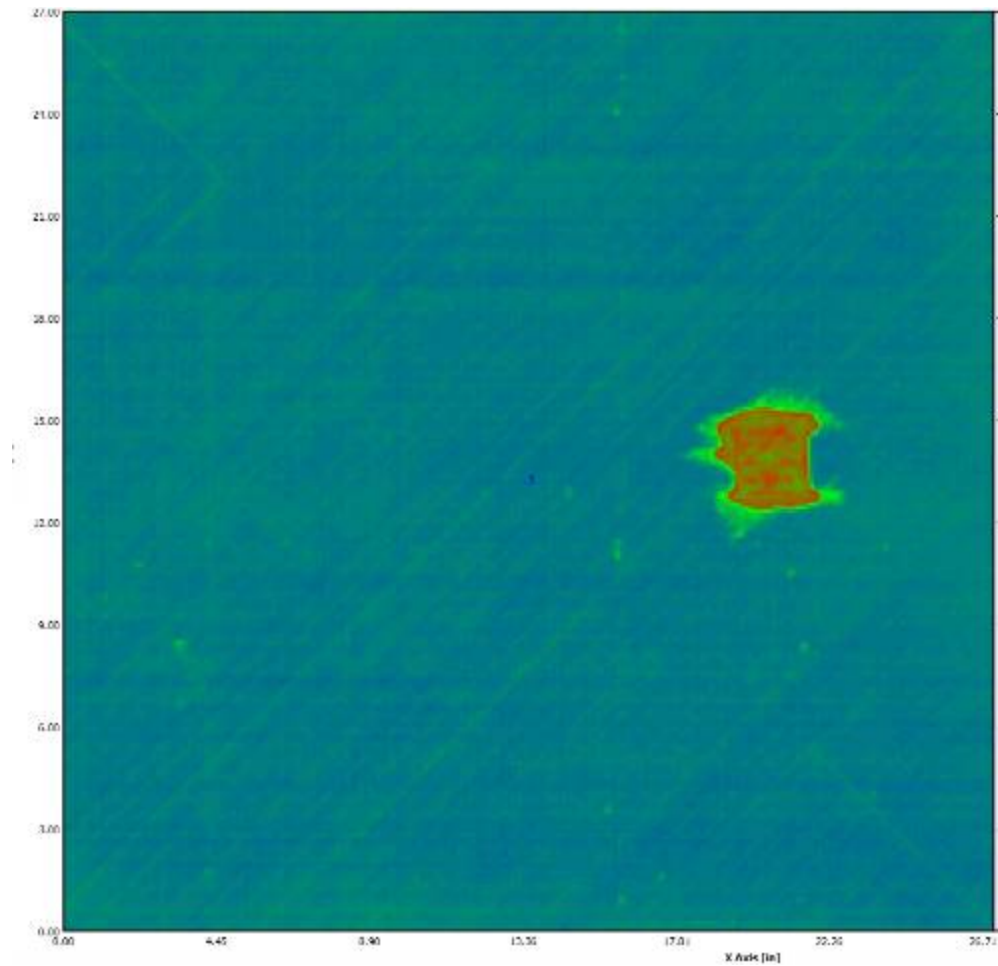


Figure 85: C-Scan image of the composite panel with delamination at 10" from the center of the panel

The beamformer transducer is operated at a frequency of 400 kHz with 10 cycle tone burst input. Transducer 1 is used as a transmitter and Transducer 2 is used as a receiver, the amplitude and phase to excite individual annular elements are taken from Table 11 to maximize mode 3. From Figure 86 the reflection from the delamination can be seen clearly. Using all the 10 transducers synthetic beamforming is carried out to locate the defects in the structure.

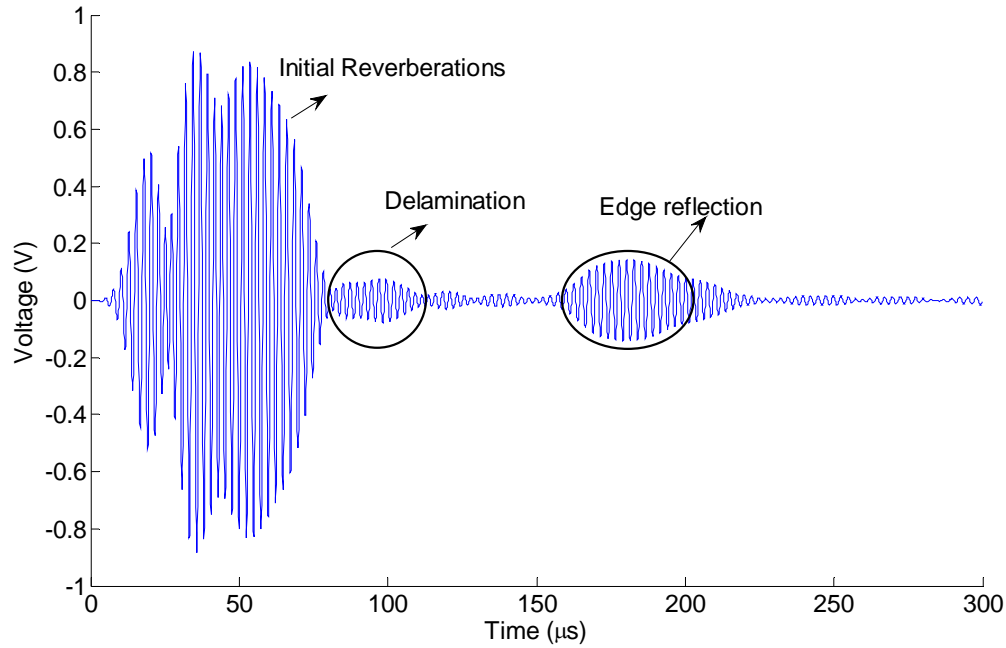


Figure 86: Signal obtained with '1' as sender and '2' as receiver with annular array time delays for mode 3 at 400 kHz

The synthetic phased array imaging of the composite plate with delamination is carried out at 400 kHz, the amplitude and time delays for the phased annular array to maximize mode 3 given in Table 11 are used. The synthetic beamforming image of the composite plate can be seen in Figure 87. After thresholding the image can be seen in Figure 88, artifacts in the image can be noticed which arise mainly because of the high ringing in the transducer which results in the reflected signal becoming overlapped with the initial part of the signal. With time delays to minimize mode 3 and maximize mode 1 the defect image can be seen in Figure 89 showing reduced signal to noise ratio resulting in no recognizable defect.

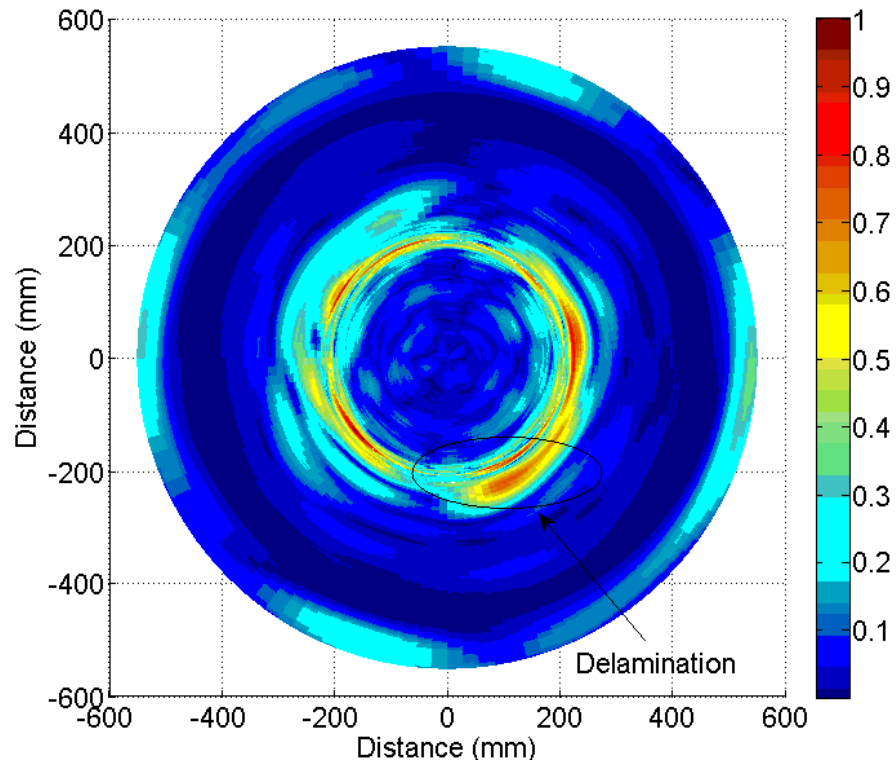


Figure 87: Phased array Image with Mode 3 time delays for the annular array showing the delamination defect and a crack type reflector

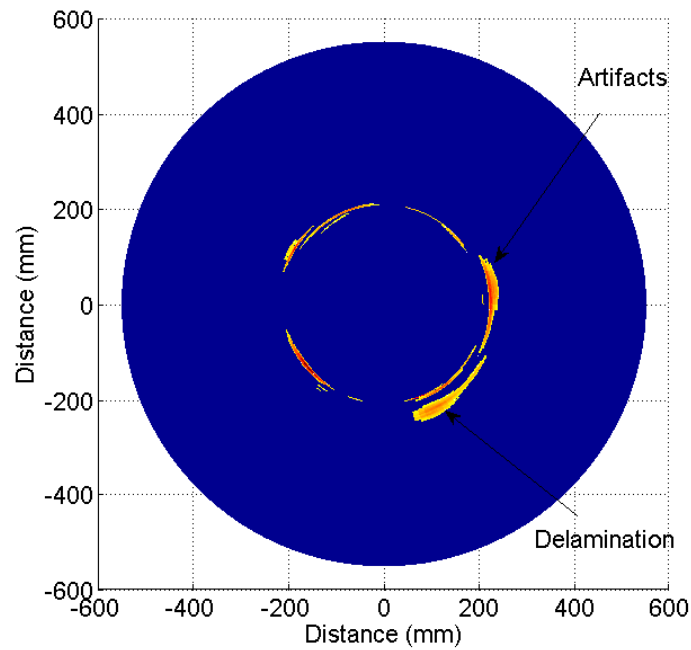


Figure 88: Phased array image of the composite plate showing the delamination after thresholding at a distance of approximately 250 mm from the center

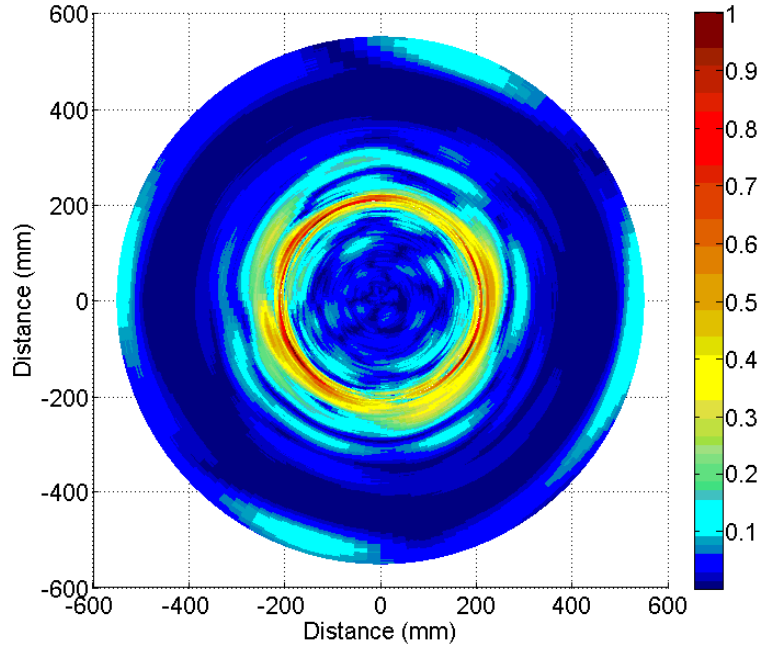


Figure 89: Phased array image with annular array time delays for maximizing mode 1 showing no recognizable defect

Phased Array System with Nonlinear Phase Delays

A phased array transducer arranged on a polar coordinate grid and nonlinear phase delay distribution was developed to ensure single mode selection under all conditions. Finite element simulations were conducted to verify that the nonlinear phased array transducer performed as predicted. Networks were assembled on a printed circuit board to generate the phase delays and bonded plate specimens were fabricated.

Theory

It can be shown that the interaction between the phased array system and an elastic medium can be represented as follows in the Fourier domain [Senesi et al, 2010]:

$$\hat{\mathbf{U}}(\mathbf{k}, \omega) = \hat{\mathbf{D}}(\mathbf{k}, \omega) \hat{\mathbf{F}}(\mathbf{k}, \omega) \quad (98)$$

where $\hat{\mathbf{U}}$, $\hat{\mathbf{D}}$, $\hat{\mathbf{F}}$ are response of the medium, the excitability matrix of the medium and the forcing function presented by the phased array system; respectively. The excitability matrix represents the dispersion properties of the elastic medium. Thus, the design of the phased array involves matching the Fourier spectrum of the elastic medium and the resulting forcing function. The Fourier spectrum of the elastic medium is non-zero only along the dispersion curves. Therefore any spatio-temporal arrangement of the forcing function must result in a peak at a desired point in the dispersion curve.

Note that if the vector $\mathbf{k} = [k_1, k_2]^T$, then $\theta = \tan^{-1}(\frac{k_2}{k_1})$ is the angle at which the wave is steered in an isotropic elastic plate. The magnitude k , is the wave-number selected. For

an anisotropic medium however, the wave will skew away from the intended direction.

In the following subsections we present and compare two kinds of phased array transducers. One is the traditional form of phased array transducer which is arranged on a rectangular grid as shown in Fig 90. The phase delay across the rectangular array varies linearly. The other is a phased array transducer which was developed by us and is arranged on a cylindrical-polar grid as shown in Fig 91. Furthermore, the phase delay along the angular direction is non-linear. Each radial ray is however a linear phased array.

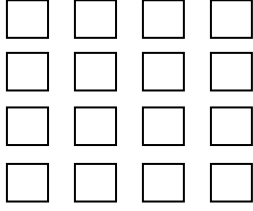


Fig 90. Phased array on rectangular grid

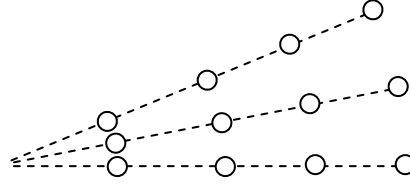


Fig 91. Phased array on a cylindrical polar grid

Phased array on a rectangular grid

Figure 90 shows a rectangular grid of transducers. The forcing function due to this kind of phase array can be written as follows.

$$\mathbf{F}(\mathbf{x}, t) = \sum_{m=-M}^M \sum_{n=-N}^N W(x - mp_x, y - np_y) f(t - m\delta t_x - n\delta t_y) \quad (99)$$

where $W(x, y)$, $f(t)$, $p_x, p_y, \delta t_x, \delta t_y$ represent the shape of each transducer element, the temporal variation of the force, the pitch of the elements in the x-direction, the pitch of the elements in the y-direction, the time delay in the x-direction and the time delay in y-direction; respectively.

The Fourier transform of the forcing function is given by:

$$\hat{\mathbf{F}} = \hat{W} \hat{f} \sum_{m=-M}^M \sum_{n=-N}^N e^{i\{m(k_x p_x + \tau_x) + n(k_y p_y + \tau_y)\}} \quad (100)$$

The product $\hat{W} \hat{f}$ is constant for a given configuration. Thus the wavenumbers and directions selected by this kind of phased array transducer occur wherever the summation in the right hand side of Eqn (100) is maximum. It can be shown that the summation has maxima corresponding to

$$k_i = \frac{2q_i\pi - \tau_i}{p_i}$$

where $i = x, y$, $q_i = 0, \pm 1, \pm 2, \pm 3 \dots$. However, for the purpose of calculation of τ_i we need to consider only $q_i = 0$. The remaining sets of k_i can be selected by varying the frequency of the signal $f(t)$. As will be demonstrated later this may cause unintended multiple modes to be generated in more than one direction.

Proposed phased array configuration

Consider a one-dimensional phased array transducer inclined at an angle ϕ_n . The peak(s) of the frequency spectrum of this kind of phased array transducer is given by

$$k_n p_n \cos(\phi_n) = 2q_n - \tau_n$$

The physical interpretation of the above equation is that the wavenumbers selected by the above phased array transducer are also rotated by an angle ϕ_n about the point $\mathbf{k}_n = (2q_n - \tau_n)\mathbf{o}_n$, where \mathbf{o}_n is the unit vector along the 1-D array. Now we can introduce a series of 1-D phased arrays inclined about different angles ϕ_n and for simplicity assume $p_n = p$. We can then choose τ_n such that all lines corresponding $k_n p$ coincide at a desired point $(k_d p, \theta)$ in the 2-D wave-number domain. The resulting configuration is shown in Fig 91. As will be demonstrated later this results in an almost unique wavenumber and direction to be selected. Factoring out other factors affecting mode selection this configuration and phasing system leads to the selection of a unique mode and unique direction of wave propagation.

Finite element simulation

Finite element simulations of guided wave propagation in a plate were performed. We attempted to select the same mode using both the configurations discussed above (rectangular and polar). For both the cases 8x8 elements were used. The total angle included for the latter type of phased array was kept at 90°. Figs 92 and 93 below show the comparison of wave propagation between phased array systems on rectangular and polar grids; respectively. It may be observed that two modes were generated in case of the rectangular grid type of phased array and primarily single mode is generated in case of the polar grid type of phased array. There are however low magnitude side lobes in the latter case, which may be remedied by using larger number of cycles and/or more number of array elements.

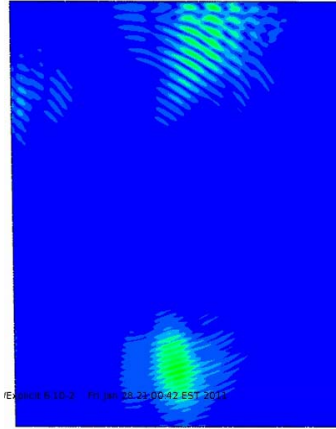


Fig 92. Multiple mode generation by phased array on rectangular grid

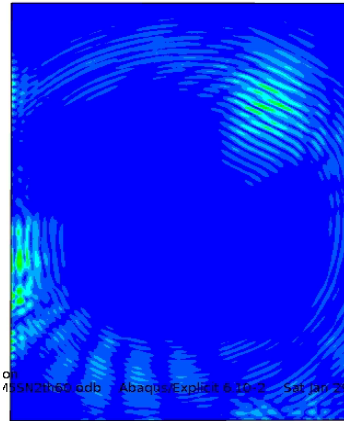


Fig 93. Primarily single mode generation using nonlinear phase and cylindrical polar coordinate grid, although noise or side lobes are present

Multichannel phase delay system

As part of the development of a multichannel phase delay system two configurations were considered. One was to use a phase shifter network to produce signals that are 90° and 180° out of phase. Intermediate phases are obtained by using potentiometers across the phase shifter outputs. The disadvantage of this approach is that the signal suffers 30dB loss at 45° , 135° , 225° and 314° . Thus intermediate amplifiers must be used to amplify the output to the original value.

The alternate approach is to use an allpass filter. An allpass filter is an active filter whose only function is to produce a phase shift. Fig 94 shows the schematic of the allpass filter together with the amplifier. The signal is injected at the left end of the above schematic. The phase delayed signal is output at the switch S1 which is subsequently amplified to 25 V peak voltage signal using the INA103 amplifier. Note that the part left of the switch S1 is the allpass filter and the phase delay is obtained by varying the resistance at R3. Furthermore the peak to peak amplitude of the input signal must be adjusted such that the output of the instrumentation amplifier is 50 V.

The performance of the allpass filter was verified using LM740 operational amplifiers on a printed circuit board with through holes. The performance of the INA103 amplifier was also similarly verified. These amplifiers however are not suitable for ultrasonic frequencies. For ultrasonic frequencies custom made printed circuit boards must be used. This is because we were unable to find high speed operational amplifiers which can be soldered onto a printed circuit board with through-holes. The development of the printed circuit board with surface mount pads (required for the high speed amplifiers) has been an iterative process. It will take at least two more iterations of alteration to the printer circuit board design and testing to arrive at a successful multichannel phase delay system. Power supply is another concern. Currently, only

one voltage regulator was used for all the INA103 amplifiers on the circuit board. This caused overheating of the voltage regulator. Hence more voltage regulators need to be procured, the exact number of which is under evaluation.

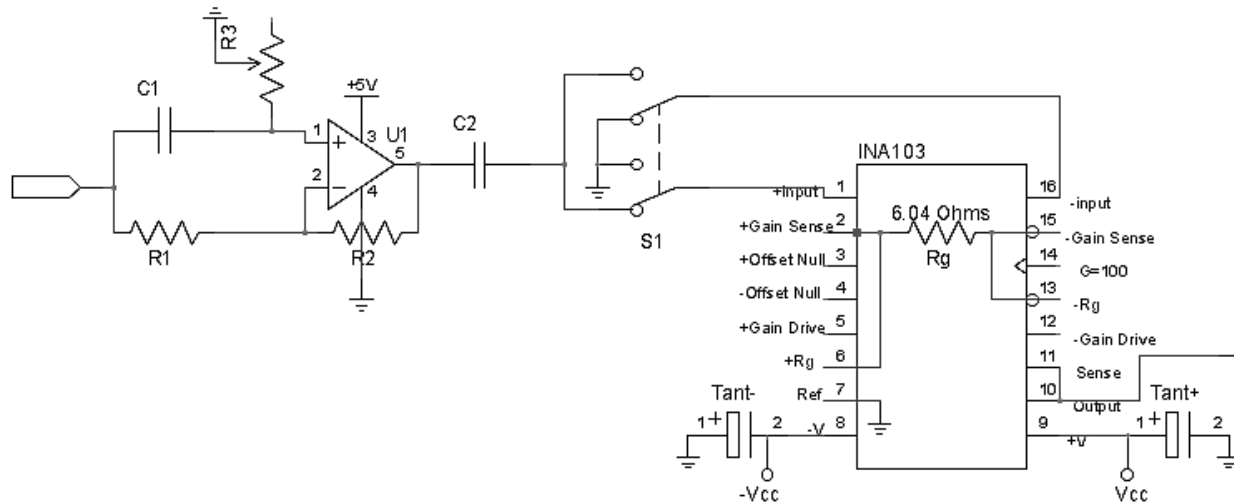


Fig 94. Schematic for a single channel phase delay system

Concluding remarks

Great potential of using ultrasonic guided wave phased arrays for SHM of composite structures has been demonstrated. On the basis of solid understanding of guided wave mechanics, guided wave mode and frequency control has been successfully implemented in guided wave tomography and phased array SHM applications. Moving forward from piezoelectric disk or rod elements that are limited on guided wave mode tuning, we have designed and fabricated annular array transducers for better guided wave mode and frequency control. We have also successfully designed transducers for better sensitivity and penetration power using different materials. We studied the feasibility of miniaturizing the annular array transducers for phased array beam forming using the time delay annular array concept. Novel guided wave beamformers have been developed and applied to both isotropic and multilayer composite structures for SHM applications. Nonlinear phased delays for better mode control and beam forming results have also been investigated. Phase delay circuits that are particularly suitable for guided wave phased array applications have also been studied.

Personnel supported

Penn State University Graduate Students who were fully or partially supported by this project: Fei Yan, Jaya Prakash Koduru, Yue Liang, Siddharth Advani, Jia Hua, Haraprasad Kannajosyula, Cody Borigo, and Owen Malinowski.

Publications

Publications that are drawn from the work done under this project include:

1. F. Yan (2008), *Ultrasonic guided wave phased array for isotropic and anisotropic plates*, Ph.D. thesis, The Pennsylvania State University.
2. Fei Yan and Joseph L. Rose, Composite Plate Inspection Using a Novel Guided Wave Skew Effect Method, *REVIEW OF PROGRESS IN QUANTITATIVE NONDESTRUCTIVE EVALUATION*, AIP Conference Proceedings, Volume 1096, pp. 1049-1056 (2009).
3. F. Yan and J. L. Rose, "Time delay comb transducers for aircraft inspection", *The Aeronautical Journal*, 2009. 113(1144): p. 417-427.
4. Fei Yan, Cliff J. Lissenden, and Joseph L. Rose, "Directivity profiles of ultrasonic guided wave phased arrays for multilayer composite plates", *Proc. SPIE* Vol. 7295, 2009.
5. Jaya Prakash Koduru and Joseph L. Rose, "Guided wave annular array sensor design for improved tomographic imaging", *REVIEW OF PROGRESS IN QUANTITATIVE NONDESTRUCTIVE EVALUATION*, AIP Conference Proceedings, Volume 1096, pp. 658-665, (2009).
6. H. Gao and J.L. Rose, "Goodness Dispersion Curves for Ultrasonic Guided Wave Based SHM: A Sample Problem in Corrosion Monitoring," *The Aeronautical Journal*, 2010. 114 (1151): p. 49-56.
7. F. Yan, R. Royer, and J. L. Rose, (2009), "Ultrasonic guided wave imaging techniques in structural health monitoring," *Journal of Intelligent Materials Systems and Structures*, Vol. 21 (3) pp. 377-384.
8. J.L. Rose (2010), "Successes and challenges in ultrasonic guided waves for NDT and SHM," *Materials Evaluation*, Volume 68 (5), pp. 495-500.
9. Jaya Prakash Koduru and Joseph L. Rose, "Modified Lead Titanate/Polymer 1-3 composite transducers for structural health monitoring", *Proc. Review of Progress in QNDE*, AIP Conf. Proc. 1211, pp. 1799-1806, 2010
10. Jaya Prakash Koduru and Joseph L. Rose, "Defect detection in composite plates using guided wave phased arrays", *U.S National Congress on Theoretical and Applied Mechanics*, 2010
11. Jaya Prakash Koduru, Guided wave phased arrays for defect detection in plate like structures, Ph.D. thesis, The Pennsylvania State University, 2010
12. Fei Yan, Cody Borigo, Yue Liang, Jaya P. Koduru and Joseph L. Rose, "Phased annular array transducers for ultrasonic guided wave applications", *Proc. SPIE* 7984, 79840S (2011)

13. J.L. Rose, "The Upcoming Revolution in Ultrasonic Guided Waves," *Proc. SPIE* 7983, 798302.
14. Jaya Prakash Koduru and Joseph L. Rose, "Guided wave phased arrays for defect detection in composite plates", in press, *Review of Progress in Quantitative Nondestructive Evaluation*, Vol. 30 (2011)

References

- Achenbach, J.D. and Xu, Y. (1999), "Wave motion in an isotropic elastic layer generated by a time-harmonic point load of arbitrary direction," *J. Acoust. Soc. Am.* **106**(1), 83-90.
- Auld, B.A. and Kino, G. S. (1971a), "Normal Mode Theory for Acoustic Waves and Their Application to the Interdigital Transducer," *IEEE Trans.* Vol. **ED-18**, 898-908.
- Auld, B.A. and Kino, G. S. (1971b), "Normal Mode Theory for Acoustic Waves and Their Application to the Interdigital Transducer," *IEEE Trans.* Vol. **ED-18**, 898-908.
- Bartoli, I., Marzani, A., Lanza di Scalea, F., and Viola, E. (2006), "Modeling wave propagation in damped waveguides of arbitrary cross-section," *J. Sound. Vibr.*, **295**, 685-707.
- Cawley, P., Alleyne, D.N., and Chan, C.W., 2000, *Inspection of Pipes*, United States Patent No. 6,148,672.
- Ditri, J.J. and Rose, J.L. (1994a), "Excitation of Guided Waves in Generally Anisotropic Layers using Finite Source," *ASME J. Appl. Mech.* **61**, 330-338.
- Ditri, J.J., Pilarski, A., Pavlakovic, B., and Rose, J.L. (1994b), "Generation of guided waves in a plate by axisymmetric normal surface loading," *Review of Quantitative Nondestructive Evaluation*, Vol. **13**, Edited by D. O. Thompson and D. E. Chimenti, 133-140.
- Gao, H. (2007), *Ultrasonic guided wave mechanics for composite material structural health monitoring*, Ph.D. thesis, The Pennsylvania State University.
- Giurgiutiu, V. (2005), "Tuned Lamb Wave Excitation and Detection with Piezoelectric Wafer Active Sensors for Structural Health Monitoring," *J. Intel. Mat. Sys. Struct.* **16**, 291-305.
- Hay, T.R., *Ph.D. Thesis*, Pennsylvania State University, University Park, PA (2004).
- Hayashi, T., Song, W.J., and Rose, L.J., 2003, "Guided wave dispersion curves for a bar with an arbitrary cross-section, a rod and rail example," *Ultrasonics*, **41**(3), pp. 175-183.
- Kino, G.S. (1987), *Acoustic Waves: Devices, Imaging and Digital Signal Processing*, Prentice-Hall, Englewood Cliffs, NJ.

Knopoff, L., 1964, "A Matrix Method for Elastic Wave Problems," *Bull. Seism. Soc. Am.* **54**, pp. 431-438.

Li, J. and Rose, J.L., 2001a, "Implementing guided wave mode control by use of a phased transducer array," *IEEE Trans. Ultrasonics Ferroelectron. Frequency Contr.*, **48**, pp. 761-768.

Quarry, M.J. and Rose, J.L., 1997, "Multimode guided wave inspection of piping using comb transducers," *Materials Evaluation*, **45**, pp. 504-508.

Raghavan, A. and Cesnik, C.E.S. (2004), "Modeling of piezoelectric-based Lamb wave generation and sensing for structural health monitoring," *Proc. of SPIE* Vol. **5391**, 419-430.

Rose, J.L., *Ultrasonic Waves in Solid Media*, Cambridge University Press, New York, NY (1999).

Schoeppner, G.A., et al., *Proceedings of AIAA/ASME/ASCE/AHS/ASC Structures, Structural Dynamics, and Materials Conference and Exhibit*, 42nd, Seattle, WA, Apr. 16-19, 2001, AIAA-2001-1216 (2001).

Thomson, W.T., 1950, "Transmission of elastic waves through a stratified solid medium," *Journal of Applied Physics*, **21**, pp. 89-93.

Velichko, A. and Wilcox P.D. (2007), "Modeling the excitation of guided waves in generally anisotropic multilayered media," *J. Acoust. Soc. Am.*, **121(2)**, 60-69.

Wilcox, P.D. (2004), "Modeling the excitation of Lamb and SH waves by point and line sources," *Review of Quantitative Nondestructive Evaluation*, Vol. **23**, Edited by D. O. Thompson and D. E. Chimenti, 206-213.

Wilcox, P.D., Lowe, M.J.S. and Cawley, P. (2005), "The excitation and detection of Lamb waves with planar coil electromagnetic acoustic transducers," *IEEE Trans. Ultrason., Ferroelect., Freq.* **52(12)**, 2370-2383.

Yan, F. (2008), *Ultrasonic guided wave phased array for isotropic and anisotropic plates*, Ph.D. thesis, The Pennsylvania State University.

Yan, F. and Rose, J.L., 2007, "Guided wave phased array beam steering in composite plates," *Proc. SPIE* Vol. **6532**, pp. 65320G.